FEDERAL UNIVERSITY OF SANTA CATARINA
DEPARTMENT OF AUTOMATION AND SYSTEMS

Eduardo Schmidt

A state estimation strategy for monitoring, control, and optimization of airborne wind energy systems

Florianópolis
2017

FEDERAL UNIVERSITY OF SANTA CATARINA
DEPARTMENT OF AUTOMATION AND SYSTEMS

Eduardo Schmidt

A state estimation strategy for monitoring, control, and optimization of airborne wind energy systems

Thesis submitted to the Postgraduate Program in Automation and Systems Engineering of the Federal University of Santa Catarina for the degree of Master of Science in Automation and Systems Engineering.

Advisor:
Prof. Dr. Alexandre Trofino Neto

Florianópolis
2017

Ficha de identificação da obra elaborada pelo autor,
através do Programa de Geração Automática da Biblioteca Universitária da UFSC.

Schmidt, Eduardo
A state estimation strategy for monitoring, control, and optimization of airborne wind energy systems / Eduardo Schmidt ; orientador, Alexandre Trofino Neto, 2017.
135 p.

Dissertação (mestrado) - Universidade Federal de Santa Catarina, Centro Tecnológico, Programa de Pós Graduação em Engenharia de Automação e Sistemas, Florianópolis, 2017.

Inclui referências.

1. Engenharia de Automação e Sistemas. 2. Energias renováveis. 3. Aerogeradores cabeados. 4. Estimação de estado. 5. Filtro de Kalman. I. Trofino Neto, Alexandre. II. Universidade Federal de Santa Catarina. Programa de Pós-Graduação em Engenharia de Automação e Sistemas. III. Título.

Eduardo Schmidt

A state estimation strategy for monitoring, control, and optimization of airborne wind energy systems

This thesis was deemed adequate for the degree of "Master (Ms.) in Automation and Systems Engineering", and approved in its final form by the Postgraduate Program in Automation and Systems Engineering.

Prof. Dr. Daniel Ferreira Coutinho
Coordinator of the postgraduate program

Examining comittee:

Prof. Dr. Hector Bessa Silveira
Federal University of Santa Catarina

Prof. Dr. Marcelo De Lellis Costa Oliveira
Western Paraná State University

Prof. Dr. Fabio Baldissera
Federal University of Santa Catarina

ACKNOWLEDGEMENTS

There are no words to express how thankful I am to my parents, Luiz and Iara, for the education, the unconditional love and support, and for always encouraging me to pursue my dreams. None of my achievements would have been possible without them. I would also like to express my gratitude to my brother, André, for always being there for me, for caring, and for teaching me valuable lessons when I least expected but needed the most. Additionally, I would like to thank my advisor, Prof. Alexandre Trofino, for trusting and giving me the opportunity to work in such an interesting project, and for his support and advisement during the development of this thesis. Finally, I would like to recognize my colleagues and friends Matheus Winter, Lucas Coelho, Romano Weirich, Rafael Duarte, Jean Damke, Henrique Hartwig, Helmut Araujo, Marcelo De Lellis, Ramiro Saraiva, Rodrigo Travessini, Gabriel Manoel, Renan Heinzen, Rafael Bidese, Giulia Ciprandi and many others for sharing their knowledge, time, thoughts, or simply for making this journey more enjoyable.

RESUMO EXPANDIDO

Introdução

O crescimento da demanda por eletricidade, associado às preocupações com o meio ambiente têm motivado uma série de importantes transformações na indústria de energia. Essas transformações são a principal causa da recente expansão das energias renováveis, que, além de diminuirem o impacto ambiental, representam também uma grande oportunidade de negócios. Estudos indicam que, até 2040, tecnologias renováveis serão responsáveis por até 60% de toda a potência elétrica gerada no planeta. Nesse cenário de transição, os sistemas de geração eólica e solar são os que apresentam maior potencial. Para a conversão de energia eólica em elétrica, atualmente utilizam-se estruturas compostas por um conjunto de pás acopladas a um gerador que sustentado por uma torre. Apesar de já bastante desenvolvida e estabelecida comercialmente, essa tecnologia apresenta algumas limitações. Quanto maior o gerador utilizado, maior a potência da turbina. Na prática, entretanto, a utilização de um gerador maior implica também no aumento do restante da estrutura, e consequentemente dos custos associados. Além disso, a potência gerada por uma turbina eólica é função das condições de vento no local onde a mesma está instalada. Mais especificamente, a potência é proporcional à disponibilidade, e à velocidade do vento, duas grandezas que aumentam com a altitude, e variam com a geografia. Sendo assim, é natural que sejam construídas estruturas cada vez maiores, capazes de explorar ventos de melhor qualidade em altitudes elevadas, e que as plantas eólicas concentrem-se em regiões com condições favoráveis de vento. Essa tendência de aumento do tamanho das turbinas vem sendo observada há muitas décadas, sendo a principal maneira de se escalar a tecnologia. Devido à não linearidade da relação entre potência e custos, acredita-se que a partir de uma determinada potência, que corresponde a uma altitude entre 150 m e 200 m, estruturas convencionais de aproveitamento eólico possam deixar de ser economicamente atrativas. Com o intuito de superar essas limitações, uma nova classe de conversores eólicos, denominada aerogeradores cabeados, vem sendo estudada. Tais sistemas

utilizam aeronaves conectadas ao solo por meio de cabos para explorar ventos em altitudes até então inacessíveis aos aerogeradores convencionais. Além de permitir a operação em altitudes elevadas, onde os ventos são mais velozes e constantes, aerogeradores cabeados tem o potencial de reduzir drasticamente custos associados às plantas eólicas, e viabilizar a instalação das mesmas em um maior número de localidades.

Apesar de extremamente promissores, sistemas de aerogeradores cabeados encontram-se atualmente em um estágio intermediário de desenvolvimento, e diversos obstáculos ainda precisam ser superados antes que eles sejam comercialmente viáveis. Entre os principais desafios estão o controle automático de vôo, o monitoramento e a detecção de anomalias no sistema, e a otimização da potência gerada. Soluções propostas para estes problemas dependem do conhecimento de variáveis tais como a posição e a velocidade da aeronave, suas características aerodinâmicas, e as condições de vento na altitude de vôo. Na maioria dos casos, informações sobre essas variáveis são pouco confiáveis, ou então inexistentes.

Objetivos

O objetivo principal deste trabalho é o desenvolvimento de uma estratégia de filtragem para aerogeradores cabeados dependente de um conjunto mínimo de medições, e que possibilite a estimação das variáveis cinemáticas do sistema, dos seus parâmetros aerodinâmicos, e das condições de vento na altitude de voo. Além dos desenvolvimentos teóricos e da realização de simulações em laboratório, os objetivos incluem ainda a implementação de uma primeira versão da solução proposta, capaz de ser integrada a um protótipo de aerogerador cabeado e validada em condições reais de operação.

Metodologia

A partir das necessidades identificadas na etapa de revisão bibliográfica, uma topologia modular de estimação foi proposta com o intuito de simplificar as etapas de projeto, implementação, e teste, e proporcionar uma maior flexibilidade na implantação em protótipos de aerogeradores cabeados. Essa estrutura é composta por dois módulos principais: o

módulo de estimação cinemática, responsavel por estimar, utilizando um conjunto de medições, a posicão e a velocidade da aeronave, e um módulo de estimação aerodinâmica, responsável por estimar as forças aerodinâmicas atuando no sistema, bem como as condições do vento na altitude de voo. Além destes dois blocos principais, foi proposta também a utilização de um bloco estático para a computação, a partir dos estados estimados, de variáveis adicionais como a eficiência equivalente do sistema e o ângulo de ataque dinâmico da aeronave. Para obtenção de um modelo dinâmico do sistema, o mesmo foi representado como um único ponto de massa. Nessa representação, assume-se que os cabos e a aeronave possam ser modeladas como uma única massa equivalente, sujeita às forças aerodinâmicas de sustentação, arrasto, e à ação da gravidade, tendo seu movimento restrito pelo cabo a uma superfície esférica centrada na unidade de solo. Ao contrário do que ocorre na maioria dos modelos ponto de massa estudados, optou-se pela utilização de coordenadas cartesianas. Utilizando o *framework* lagrangiano, foram obtidas as equações dinâmicas do sistema, que mais tarde foram utilizadas na implementação de dois filtros de Kalman estendidos, um para cada módulo proposto. Os vetores de observacão dos filtros foram construídos utilizando variáveis disponíveis em praticamente todos os protótipos de aerogeradores cabeados estudados. No módulo de estimação cinemática, foram incluídas medições de distância entre a aeronave e um conjunto de pontos de referência no solo, obtidas por módulos de rádio-frequência com o intuito de aumentar a qualidade da estimação na presença de fenômenos devidos à não rigidez do cabo. A utilização de dispositivos de radio-frequência para a estimação da posição e velocidade da aeronave no contexto de aerogeradores cabeados foi proposta recentemente e, até o presente momento, ainda não havia sido validada na prática. No filtro de Kalman do módulo de estimação aerodinâmica foi aplicada ainda a técnica da medição perfeita para a imposição de uma restrição de ortogonalidade entre o vetor da força de sustentação e o vento aparente, o que melhorou as características de convergência do estimador. A estrutura de estimação proposta foi implementada em *software* utilizando uma plataforma embarcada desenvolvida pelo grupo de pesquisa em que este trabalho foi realizado, e que contou com a colaboração do autor. Para a validação em laboratório da solução desenvolvida, foi implementado um ambiente de

simulação na linguagem Python, o que permitiu a realização de experimentos na configuração *hardware-in-the-loop*. Já para a avaliação experimental dos estimadores foi utilizado um protótipo de pequena escala também disponível no laboratório. Para a obtenção das medições de distância utilizadas no módulo de estimação cinemática, módulos de rádio-frequência foram adquiridos e adaptados, resultando em um sistema de fácil instalação em campo. Todos os outros sensores necessários para a implementação dos estimadores já encontravam-se disponíveis no protótipo.

Resultados e discussão

No ambiente de simulação, os estimadores foram capazes de rastrear todas as variáveis do sistema, sendo que as referências, ou valores teóricos destas foram obtidos diretamente do modelo utilizado na simulação. Com base nos estados estimados, foi possível calcular os parâmetros aerodinâmicos da aeronave, bem como o seu ângulo de ataque. Nos ensaios experimentais realizados em campo foi possível estimar, utilizando a solução desenvolvida, a posição em coordenadas esféricas do aerofolio, e compará-la com as leituras obtidas dos *encoders* rotativos instalados junto à base. Comparando os valores referentes ao ângulo polar, é possivel perceber um *offset* considerável entre as estimativas e as leituras do *encoder*, o que provavelmente se deve à não rigidez do cabo, conforme já discutido na literatura. Embora já observada em simulações, esse fenômeno nunca havia sido verificado na prática. É interessante que, mesmo em situações com um comprimento de cabo relativamente curto, o fenômeno já é perfeitamente visível. Em relação ao ângulo de azimute, é possível perceber que a leitura do *encoder* possui uma leve atenuação quando comparada às estimativas obtidas, o que provavelmente se deve à dinâmica inserida pelo cabo no sistema. As demais variáveis estimadas tiveram um comportamento parecido com o obtido nas simulações, indicando um correto funcionamento dos estimadores, e novamente permitiram a computação das características aerodinâmicas da aeronave durante o vôo.

Em resumo, este trabalho realizou um estudo das diferentes abordagens voltadas à estimação no contexto de aerogeradores cabeados, analisando as vantagens e desvantagens de cada uma delas. A par-

tir desse estudo, foi proposta uma topologia de estimação em cascata, com dois estágios baseados no filtro de Kalman estendido. A estrutura proposta foi implementada, integrada a um protótipo de pequena escala, validada em um ambiente de simulação, e avaliada em condições reais de operação. Os resultados obtidos demonstraram a eficácia dos módulos desenvolvidos na estimação da posição e velocidade da aeronave, das suas características aerodinâmicas, e das condições de vento na altitude de voo, e indicam que os mesmos possuem vantagens em relação às abordagens já existentes, principalmente devido à utilização de dispositivos de rádio-frequência e à imposição da restrição de ortogonalidade entre os vetores força de sustentação e vento aparente estimados. Em relação ao potencial de aplicação, acredita-se que a estrutura proposta possa ser utilizada como uma plataforma flexível de estimação sobre a qual blocos de controle, otimização, e detecção de anomalias podem ser desenvolvidos. As variáveis estimadas também podem ser utilizadas para melhorar o processo de projeto e avaliação do desempenho aerodinâmico de aeronaves, e permitem avaliar o potencial eólico de um determinado terreno antes da instalação do aerogerador. Entre as vantagens da solução proposta estão a dependência de um conjunto mínimo de sensores, disponíveis em praticamente todos os protótipos de aerogeradores cabeados estudados; a possibilidade de aplicação em diferentes tipos de sistema, independente da configuração dos mesmos; e a flexibilidade na instalação devido à estrutura modular, o que também favorece a redução dos atrasos de comunicação entre a aeronave e a unidade de solo.

RESUMO

Aerogeradores cabeados são sistemas de aproveitamento eólico que se utilizam das forças aerodinâmicas atuando sobre estruturas suspensas conectadas ao solo por meio de cabos para a produção de energia elétrica. Além de permitir a operação em altitudes elevadas, onde os ventos são mais velozes e constantes, esses sistemas tem o potencial de reduzir drasticamente custos associados às plantas eólicas, e viabilizar a instalação das mesmas em um maior número de localidades, o que vem atraindo o interesse tanto da indústria quanto da academia. Apesar de promissores, tais sistemas encontram-se atualmente em um estágio intermediário de desenvolvimento, e diversos obstáculos ainda precisam ser superados antes que eles sejam comercialmente viáveis. Ao longo da última década, controle de vôo foi o assunto que despertou maior interesse da comunidade de aerogeradores cabeados. Entretanto, mais recentemente, a otimização da potência gerada por esses sistemas passou também a ocupar um lugar de destaque nas pesquisas. Uma vez que as soluções propostas para estes problemas dependem do conhecimento de variáveis tais como a posição e a velocidade da aeronave, suas características aerodinâmicas, e as condições de vento na altitude de vôo, é fundamental para o avanço da tecnologia obter mecanismos eficazes para a estimação dessas variáveis. Neste contexto, o presente trabalho apresenta uma estratégia de estimação para aerogeradores cabeados composta por uma estrutura composta por dois filtros de Kalman estendidos associados em cascata, e capaz de obter, em tempo-real, utilizando uma quantidade mínima de sensores, estimativas da posição e a velocidade da aeronave, das condições de vento na altitude de voo, e das forças atuando sobre o sistema, que por sua vez podem ser utilizadas na determinação das características aerodinâmicas do mesmo. A solução proposta é validada em um ambiente de simulação e mais tarde testada em condições reais de operação em experimentos envolvendo um protótipo de pequena escala, e resultados obtidos indicam que ela é capaz de fornecer informações confiáveis para fins de monitoramento, controle, e otimização de aerogeradores cabeados. Finalmente, os estimadores projetados podem ser facilmente adaptados à outras configurações, e são capazes de acomodar medições adicionais, o que é altamente desejável considerando o nível de maturidade da tec-

nologia e a variedade de conceitos em uso pela comunidade. Além da estratégia de estimação, podem também ser considerados contribuições deste trabalho o desenvolvimento de um ambiente de simulação, de uma plataforma de software embarcado, e uma interface gráfica de usuário voltados especificamente para a aplicação.

Palavras-chave: Energias renováveis, Aerogeradores cabeados, Estimação e estado e parâmetros, Filtro de Kalman estendido.

ABSTRACT

Airborne Wind Energy (AWE) systems harvest wind power by exploiting the aerodynamic forces acting on lightweight suspended structures anchored to the ground by means of one or more tethers. Among other advantages, this technology is able to reach higher altitudes than conventional wind turbines, where the winds are generally stronger and more consistent, while dramatically reducing the construction and installation costs of the power plant. These characteristics allow AWE devices to be deployed virtually anywhere, and have been attracting a lot of interest from both academia and industry. However, despite the promising outlook in terms of economical feasibility, the technology is currently at an intermediate development stage, and there are still several challenges to be overcome before it can reach the market. In the last decade, the problem of control design for AWE generators has been extensively studied, and more recently the optimization of their power yield has also become a concern. Since effective solutions to these problems rely on knowledge of both system parameters and state, reliably estimating these quantities is fundamental for pushing the technology forward. In this context, the present thesis introduces an estimation strategy for AWE comprising two cascaded Extended Kalman Filters (EKFs) capable of obtaining in real time and from a minimum amount of data the position and velocity of the aircraft, the wind conditions at flight level, and the forces acting upon the system, which can in turn be used to determine its aerodynamic characteristics. The proposed solution is validated in a simulation environment and later tested under actual operating conditions in experiments involving a small scale prototype, with results indicating that it can indeed provide AWE systems with reliable information for the purposes of monitoring, control and optimization. Finally, the designed estimators are shown to be easily extensible to support other configurations and to accommodate additional measurements, which is highly desirable given the level of maturity of the technology and the variety of experimental setups in use by the community. Besides the estimation strategy, a simulation environment, an embedded software platform, and a graphical user interface were also developed, and can be seen as secondary contributions of this work.

Keywords: Renewable energy systems. Airborne wind energy. State and parameter estimation. Extended Kalman filters.

Contents

List of Figures

List of Tables

Acronyms

AOA	Angle-of-arrival.
API	Application Programming Interface.
AWE	Airborne Wind Energy.
CRLB	Cramer-Rao Lower Bound.
CSMA	Carrier sense multiple access with collision avoidance.
CSS	Chirp Spread Spectrum.
EKF	Extended Kalman Filter.
FDOA	Frequency-difference-of-arrival.
FOS	Fast Orthogonal Search.
GPS	Global Positioning System.
GSL	GNU Scientific Library.
HIL	Hardware-in-the-loop.
IEA	International Energy Agency.
IMU	Inertial Measurement Unit.
KF	Kalman Filter.
LCOE	Levelized Cost of Electricity.

LEI	Leading Edge Inflatable.
LiPo	Lithium Polymer.
LLS	Linear Least Squares.
MHE	Moving Horizon Estimator.
NLS	Nonlinear Least Squares.
NMPC	Nonlinear Model Predictive Control.
NSBEE	Nanotron Swarm Bee.
OS	Operating System.
PDF	Probability Density Function.
POA	Phase-of-arrival.
RF	Radio Frequency.
RSS	Receiver signal strength.
SDS-TWR	Symmetrical Double-Sided Two-Way Ranging.
SI	International System of Units.
TDOA	Time-difference-of-arrival.
TOA	Time-of-arrival.
TOF	Time-of-flight.
UKF	Unscented Kalman Filter.
UWB	Ultra-wideband.

CHAPTER 1

Introduction

The increasing demand for electricity associated with recent environmental concerns are propelling an important transformation in the energy industry. These changes are the root cause behind the recent expansion of renewable energy sources, which have also unveiled a great business opportunity. Together, hydropower, wind, and solar are expected to become responsible for up to 60% of the power generated in the planet by 2040. In this context, one of the most promising technologies is Airborne Wind Energy (AWE), which aims at harvesting high altitude wind power at a fraction of the cost of conventional wind turbines. Although exciting, AWE is currently at an intermediate development stage, and several challenges still need to be overcome before it can reach the market. This thesis represents a contribution to one of these challenges, which is the estimation of important variables for monitoring, control, and optimization of AWE devices, especially with respect to their power output.

This chapter provides a brief historical overview of energy technologies, followed by an analysis of the transformations the sector is currently going through, and by an introduction to the concept of AWE and to its challenges. Once the reader is familiar with the subject, the

aim of the thesis is formally described and justified based on excerpts extracted from the literature. Finally, the last two sections provide an overview of the document structure and of the conventions adopted within the text.

1.1 Historical overview

Before the industrial revolution, the world's energy needs were modest. With the adoption of the modern coal powered steam engine as the primary source of mechanical work, however, this paradigm started to change. Due to economical advantages, steam engines were soon powering locomotives, factories, and farm implements. At the time, coal was also used as the main energy source for heating buildings and smelting iron into steel.

Not much later, the world saw its first hydroelectric plant, and rivers that once turned wheels to grind corn were now grinding out electricity instead. By the late 1800s, a new form of fuel was catching on: petroleum. It quickly became a valuable commodity for lighting and, by the turn of the century, its derivatives were firing internal combustion engines, which had many advantages over their predecessor, the steam engine.

With the low-cost automobile and the spread of electricity, society's energy use changed for good. Power plants became larger, until there were massive coal plants, hydroelectric dams, and even nuclear stations. Power lines extended hundreds of kilometers between cities, bringing electricity to rural areas. Energy use grew quickly, doubling every 10 years. The cost of energy production was declining steadily, and its efficient use, as well as the associated environmental impacts, were simply not a concern [2]. After 1970, however, this blooming scenario suffered a major setback, as the overconsumption together with a series of political and military events in the middle-east caused the petroleum prices to rocket overnight, leading to shortages of this commodity in many of the world's most industrialized countries, and ultimately to a recession period.

The recession made clear how dependent the global economy was on fossil fuels, and forced governments into an in-depth oil and gas risk assessment. In the years that followed, efforts were put into establish-

ing strategic petroleum reserves, exploring and developing alternative energy sources, making changes in policies, and increasing energy efficiency. Society had a glimpse of what would happen if it ran out of fossil fuels, and it became obvious that in order to keep up the pace of economical and technological growth, it would be necessary to find a long-term solution to the energy problem. Furthermore, it was in the years that followed the 1970's recession that the environmental movement started to gain significant traction, as people realized the energy crisis was partially caused by their consumption habits, and started questioning whether these very same habits could not be the root cause of other devastating natural phenomena.

1.2 Global outlook

Even though the response to the 1970's oil shocks gave the planet a life-saving head start in the struggle to avoid catastrophic climate change, fossil fuels, the most likely villains behind global warming, still remain important, and are responsible for a share of approximately 86% of the total primary energy produced in the planet. According to a recent study published in [3] by the International Energy Agency (IEA), the global energy demand will experience an increase of 30% until 2040, as depicted in Figure 1.1, while the demand for electricity is expected to double by 2060, mostly due to the technology-enabled lifestyle of the urban centers. Meeting this demand will require a substantial effort from human civilization, and while efficiency gains resulting from new technologies might favor more industrialized economies, the IEA predicts that hundreds of millions of people might still be left without basic energy services in 2040.

Besides meeting the energy demand, in order to achieve the objectives of the increasingly stringent climate policies, such as the recently signed Paris Agreement – which pledges to limit the rise in global average temperature to well below 2^oC above pre-industrial levels, the governmental entities are expected to gradually change their subsidy policies to support low-carbon energy sources such as wind and solar. This trend, associated with cost declines in key technologies, will cause the renewable energy industry to experience a fast expansion, becoming responsible for up to 60% of the electric power generated by the end of

the prediction horizon. The transition phenomena has already started, and an increasing slice of the roughly $ 1.8 trillion investment in the energy sector has been attracted to clean energy every year. A major portion of these resources is being channeled to fund wind and solar, which currently are our most promising technologies, and, according to the IEA, will be responsible for almost half of the energy generated from renewable sources by 2060.

Investment in upstream oil and gas, on the other hand, has started to fall sharply, and subsidies to this industry dropped in 2015 to $325 billion from $500 billion the previous year, reflecting not only lower fossil-fuel prices but also the subsidy reform process that has gathered momentum in several countries.

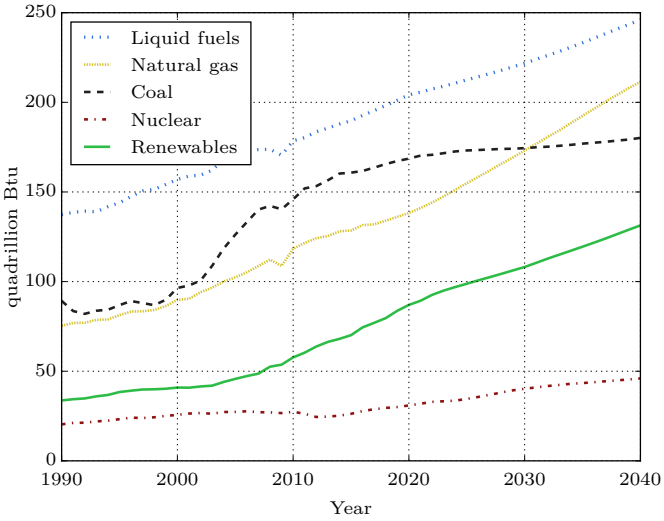

Figure 1.1: Total world energy consumption by energy source
Source: Adapted from [4]

Wind power has the potential to meet the world's energy demand and, differently from fossil sources, it is largely available almost everywhere [5]. It has been around for a long time, and while at first its use was limited to sailing, grinding grains, and pumping-water, the development of electric power opened up a number of new applications for the technology. Eventually, small wind stations suitable for farms

or residences were developed, as well as larger utility-scale generators that could be connected to the electric power grid. Nowadays, wind powered generators operate in every size range between tiny stations for battery charging up to near-gigawatt sized offshore wind farms that provide electric power to national electrical networks.

However, the current wind power technology, based on wind towers, has several limitations that need to be overcome to make such energy source competitive against fossil sources. In particular, wind towers require heavy foundations and huge blades, with massive investments leading to higher energy production costs with respect to thermal plants. Moreover, the average power density per square kilometer obtained by the present wind farms is 200–300 times lower than that of big thermal plants of the same rated power, leading to significant land occupation and impact on the environment [5].

The ultimate goal of the conventional wind harvesting technology is to further scale up the turbines towards higher power levels. This trend can be seen in Figure 1.2, which shows the evolution of wind turbines in both size and power since 1980. The growth in size, however, comes at the expense of higher materials, transportation, installation, and maintenance costs, especially in offshore scenarios. As a result, it turns out that many investments in wind farms are only economically attractive due to governmental subsidies and other incentives such as carbon credit sales.

We may eventually come to a point where further decreases in the system weight, as well as advances in materials and turbine design will simply stop making economical sense. Furthermore, tower-based turbines harvest most of their power at the tip of the blades due to their higher tangential speed. Studies such as [7] show that 30% of the outer area is responsible for more than 50% of the power output of a wind turbine, while the inner portion serves basically to transfer the mechanical power to the generator inside the nacelle. In order to withstand the weight of the nacelle and the blades, not to mention the strong bending moment due to the rotor operation, the tower requires a bulky, expensive structure, which does not directly favor the energy generation nor the economical viability. Together, tower and blades comprise almost half of the total cost of a wind turbine.

Finally, due to the aforementioned reasons, wind towers are eco-

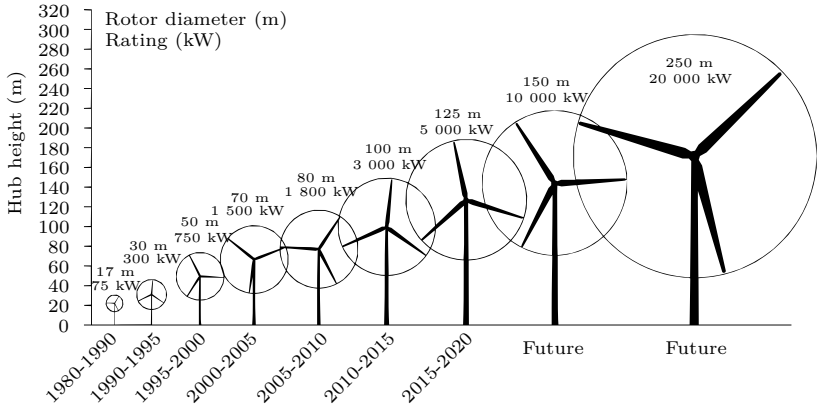

Figure 1.2: Evolution of the conventional wind turbines
Source: Adapted from [6]

nomically attractive only up to a maximum height of about 150 m, and can therefore be used with profit only in locations with "good" wind speed at 50–150 m of height from the ground [5].

1.3 Airborne wind energy

Among the novel technologies for producing electricity from renewable resources, a new class of wind energy converters has been conceived under the name of AWE systems. This new generation of systems employs flying wings or aircraft in order to reach winds blowing at atmosphere layers that are inaccessible to traditional wind turbines [8]. AWE technology is able to reach higher altitudes than conventional wind turbines, where the wind is generally stronger and more consistent, as depicted in Figure 1.3, while allowing for a reduction in the construction and installation costs of the power plant. Moreover, since most locations offer a good wind potential at higher altitudes, deployment sites for AWE systems are much easier to find, which makes the technology even more appealing. This becomes evident from the inspection of Figure 1.4, which compares the Levelized Cost of Electricity (LCOE) [1] of

[1]The LCOE is a measure which attempts to compare different methods of electricity generation on a consistent basis. It is an economic assessment of the average total cost to build and operate a power-generating asset over its lifetime divided

a 100 kW conventional wind turbine and an AWE system of equal rated power developed by the german company EnerKite.

Airborne wind energy systems usually consist of two major components, namely a ground station and an aircraft, which are mechanically or sometimes even electrically connected by one or more tethers. Among the different concepts, we can distinguish ground-generation systems, in which the conversion of mechanical energy into electrical energy takes place at the ground, and airborne-generation systems, in which the conversion occurs at the aircraft and the electricity is transferred to the ground through the tether. Within these two groups there are many other possible subdivisions, depending e.g. on the type of aircraft, steering concept, and the presence or absence of movement of the ground station.

1.4 Motivation

In the last decade, developments in the AWE sector have experienced an extremely rapid acceleration. Several companies have entered the business of high-altitude wind energy, registering hundreds of patents and developing a number of prototypes and demonstrators. Research teams all over the world are currently working on different aspects of the technology, including control, electronics and mechanical design [8].

Despite the promising outlook in terms of economical feasibility, as pointed out in [11, 12], AWE technology is currently at an intermediate development stage, with several challenges yet to be overcome before it can reach the market. Tether technology, aerodynamics and wing design, sensors, control and energy conversion are all fields where AWE-oriented research is required either to solve technical bottlenecks or to improve off-the-shelf solutions that are being already used [13].

According to [14], the challenge of an AWE system is that it requires reliable and fully autonomous flight of a tethered wing – an unstable system with non-linear dynamics. In this context, reliable and accurate state estimates are necessary [15].

In the last few years, the problem of control design for airborne wind energy generators has been studied by several research groups

by the total energy output of the asset over that lifetime. The LCOE can also be regarded as the minimum cost at which energy must be sold in order to break-even over the lifetime of the project.

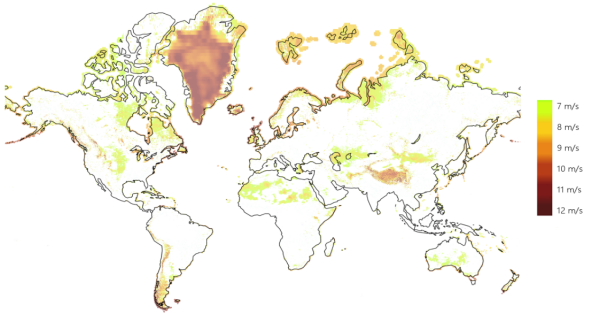

50 m height

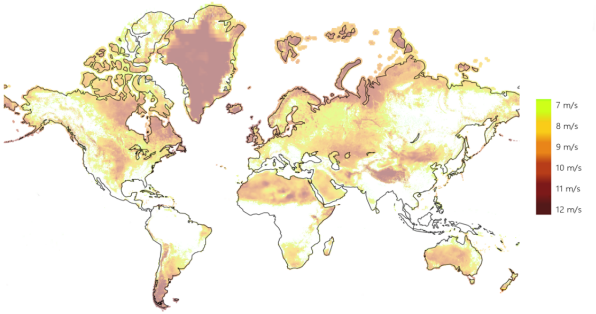

200 m height

Figure 1.3: Global wind availability and average speed
Source: [9]

and companies, leading to a quite significant series of theoretical and numerical results. All of the recently developed control approaches rely on the availability of a series of variables to be used for feedback, most notably the wing's 3-D position and velocity. The problem of estimating these quantities with sufficiently good accuracy and limited lag is therefore of paramount importance in the field. However, in the literature, there are only few works on this topic, highlighting the specific issues that need to be addressed and providing either numerical or experimental results [16].

Besides the airfoil position and velocity, knowledge of the wind conditions at flight level could also be extremely useful for controlling the system, as pointed out in [17].

More recently, attention has been paid not only to the control prob-

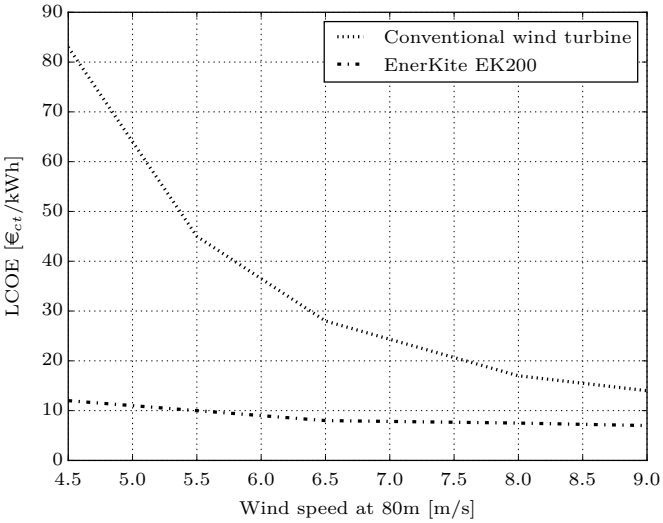

Figure 1.4: LCOE of a conventional wind turbine and of an AWE system of equivalent rated power

Source: Adapted from [10]

lem, but also to strategies aiming at maximizing the generated power of the AWE system. Approaches, as the one presented in [18], rely on the knowledge of the aerodynamic characteristics of the airfoil. These parameters, besides depending on the constructive characteristics of the wing, are also substantially time-variant. Another work concerned with this same aspect is [19], which employs numerical optimization techniques to optimally choose the design and operational parameters of AWE systems operating in a configuration known as pumping-kite. More specifically, the author presents optimal values for the reeling out/in speeds, elevation, and azimuth angles of the flight path during both the active and the passive phases, which turn out to be functions of the nominal wind at flight level. As these optimization based approaches become more popular, addressing the problem of estimating aerodynamic parameters, the wind characteristics, and other variables not strictly needed for control purposes becomes necessary.

1.5 Objectives

The aim of this thesis is, therefore, to develop a filtering setup for Airborne Wind Energy systems capable of estimating the airfoil kinematic variables, its aerodynamic parameters, and the wind characteristics at flight level, relying on the least possible set of measurements, and allowing for the implementation of more advanced power optimization strategies and fault detection schemes in the future. Besides the theoretical work and the simulation results, this thesis also aims at yielding a version of the proposed solution suitable for integration into an actual AWE prototype, and to validate it under operating conditions during field experiments.

More specifically, the purposes of the thesis are:

- To study measurement techniques and estimation approaches presented in the literature and already in use by the AWE community;
- To identify, based on the aforementioned study, needs of the AWE community related to the estimation of variables, and to specify a solution capable of meeting these needs;
- To propose a solution meeting the specifications resulting from the previous item;
- To implement the proposed solution, including all hardware and software modules required for its correct functioning;
- To evaluate the performance of the developed solution, and determine its advantages and drawbacks with respect to other solutions in the literature.

1.6 Document structure

The thesis is organized as follows:

- Chapter 2 provides a brief theoretical introduction to topics fundamental to the comprehension of the document, including an overview of basic aerodynamics, modeling of dynamical systems, estimation, and wireless positioning techniques;

- Chapter 3 presents the AWE technology, discusses its advantages and classifies the constructive concepts used to harness wind power at high altitudes;

- Chapter 4 reviews the recent AWE literature, describing the current state-of-the-art in modeling, control, optimization, measurement, and estimation techniques. The chapter is meant to motivate the study, and to provide the reader with enough background to understand the constraints of the problem at hand, the reasons behind the design choices, and the advantages of the resulting solution;

- Chapter 5 derives a simplified dynamical model of a generic tethered aircraft, and describes in detail the estimation strategy proposed for AWE systems and which is at the core of this thesis;

- Chapter 6 gives a general idea of the experimental setup used in the validation of the proposed solution, and describes both the radio-frequency based positioning infrastructure and the software modules responsible for executing the estimators;

- Chapter 7 presents the results obtained with the proposed estimation solution both in the lab, using a simulation environment, and during field tests, with a small-scale AWE prototype;

- Chapter 8 finally summarizes the accomplishments of this work, discusses its importance and limitations, and presents a series of subjects for future investigations.

1.7 Notation and units

Within this document vectors are denoted by bold characters, their Euclidean norm by $\|.\|$, and scalar values by non-bold characters. In situations involving more than one reference frame, the frame in which a vector is expressed is indicated by a superscript. The symbol x_k indicates the k–th sample of a discrete signal x, and when the quantity represented by x is originally continuous, x_k refers to its discretized version. When charting vectorial signals, the x, y, and z components are represented in different colors, as indicated in the legend. Scalars

are always charted in blue. Otherwise explicitly noted, all quantities are described in the International System of Units (SI).

CHAPTER 2

Theoretical background

The work presented in this thesis requires, for its comprehension, knowledge from very distinct, sometimes even unrelated areas. In order to avoid jeopardizing the reading and interrupting the flow of thought by including in other chapters content that is not directly related to AWE, this chapter centralizes all topics necessary for the understanding of the remaining of the document. Therefore, a brief theoretical introduction is provided to subjects such as basic aerodynamics, modeling of dynamical systems, estimation, and wireless positioning techniques, including, whenever possible, suggestions of references for further study.

2.1 Basic aerodynamics

A wing, or airfoil, can be defined as a characteristically shaped structure which, when subject to such an air flow, gives rise to an aerodynamic force. The ultimate goal of an airfoil is to obtain the lift necessary to keep it in suspension. Although a flat plat could be used, Sir George Cayley and Otto Libenthal, in the beginning of the 19^{th} century, demonstrated that curved surfaces are more efficient for this purpose. Early tests showed that, in addition to a curved surface, it

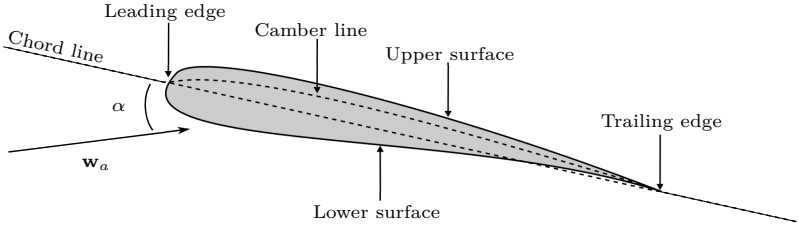

Figure 2.1: Profile view of an airfoil with its main elements
Source: Original

was desirable to have airfoils with a rounded leading edge and a sharp trailing edge [20], resulting in the profile shown in Figure 2.1, which also indicates a few of the main elements of an airfoil shape.

The upper surface, sometimes also referred to as suction surface, is generally associated with higher velocities and lower static pressure, whereas the lower, or pressure surface, is subject to higher static pressure. This difference in pressure between the two surfaces contributes to the appearance of the aerodynamic lift force. The leading edge is the point at the front of the airfoil that has maximum curvature, i.e. minimum radius. The trailing edge is the point of minimum curvature at the rear of the airfoil. The chord line is the straight line connecting leading and trailing edges. The chord length, or simply chord, is the length of the chord line. The mean camber line or mean line is the locus of points midway between the upper and lower surfaces, and is what determines the curvature of the airfoil. Its shape depends on the thickness distribution, which is variable along the chord. The aerodynamic center of the airfoil is the chord-wise length about which the pitching moment is independent of the lift coefficient and the angle-of-attack; and the center of pressure is the chord-wise location about which the pitching moment is zero [21].

The intensity and direction of the flow through which the airfoil is moving, represented in this work by the apparent, or effective wind vector $\mathbf{w}_a$, is given by the composition of the airfoil velocity vector $\dot{\mathbf{r}}$ and the nominal wind speed with respect to the ground $\mathbf{w}_n$, according to the equation

$$\mathbf{w}_a = \mathbf{w}_n - \dot{\mathbf{r}}. \tag{2.1}$$

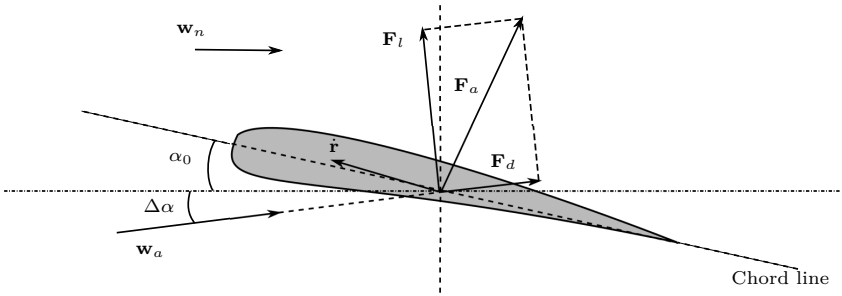

Figure 2.2: Angles and forces acting on a tethered airfoil
Source: Original

The angle α between the relative wind $\mathbf{w}_a$ and the chord line in the airfoil plane of symmetry receives then the name of angle-of-attack. If the airfoil flies tethered to the ground, this angle, which is indicated in Figure 2.1, can be further split into two components, namely the static, and the dynamic angle-of-attack. The static angle-of-attack α_0 depends solely on how the lines are adjusted with respect to the airfoil, and unless a specific control input is used to change it, it can be considered constant. The dynamic angle-of-attack, on the other hand, is a function of the position of the airfoil on the wind window, of its velocity, and of the nominal wind. The aerodynamic force resulting from the interaction of the airfoil with the air flow to which it is subject can be decomposed into two orthogonal components, namely the lift and the drag forces, both illustrated in Figure 2.2. Whereas the drag force F_d has the same orientation of the apparent wind, the lift force is always perpendicular to it. The magnitudes of the lift and drag forces are given by the equations

$$\begin{aligned} ||\mathbf{F_l}|| &= \frac{1}{2}\rho A C_l ||\mathbf{w_a}||^2, \\ ||\mathbf{F_d}|| &= \frac{1}{2}\rho A C_d ||\mathbf{w_a}||^2, \end{aligned} \tag{2.2}$$

where ρ is the air density, A is the airfoil projected area, and C_l and C_d are the lift and drag coefficients, respectively. These parameters vary as function of the angle-of-attack of the airfoil, but how exactly they change with α depends on the constructive characteristics of the airfoil.

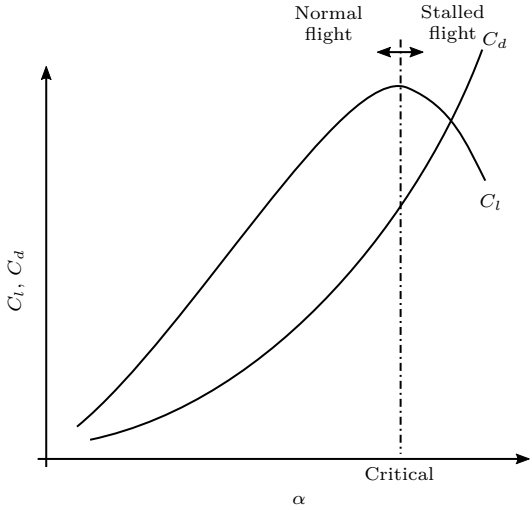

Figure 2.3: Typical lift and drag curves
Source: Original

Both for aviation and energy generation purposes, a high lift-to-drag ratio, defined as C_l/C_d is desired. This ratio is sometimes also referred to as the aerodynamic efficiency E of the airfoil, denomination that will be employed throughout this document.

The curves describing the variation of C_l and C_d with respect to changes in the angle-of-attack can be obtained empirically through complex wind tunnel experiments, and are extremely valuable for design and optimization, since these parameters have direct implication in maneuverability and controllability of the aircraft. As already mentioned, although the exact shape of the aerodynamic curves might differ according to the constructive characteristics of the aircraft, the typical behavior of C_l and C_d as the angle-of-attack changes is presented in Figure 2.3. Note that there is a value of α for which the coefficient of lift is maximum. After this value, known as the critical angle-of-attack, the airfoil will fly in a stall condition, meaning that any increase in α will cause the lift coefficient to drop. The critical angle-of-attack depends on several factors such as the airfoil section or profile of the wing, its projected shape, and aspect ratio.

2.2 Wind modeling

Within the Planetary Boundary Layer (PBL) - the lowest portion of the atmosphere, which extends up to approximately 600 m, the wind is mainly influenced by interactions with the surface of the Earth and by thermodynamic phenomena [22]. Therefore, surface roughness and obstacles can affect the flow, reducing its speed and changing its direction significantly, as can different meteorological conditions. The altitude effect on wind speed is of fundamental importance for modeling and analyzing wind power systems. In this context, two main models are usually employed, namely the logarithmic wind profile and the wind profile power law [23].

2.2.1 Logarithmic wind profile

The logarithmic wind profile is a semi-empirical relationship commonly used to describe the vertical distribution of horizontal mean wind speeds within the lowest portion of the PBL. In this model, the absolute wind speed at a given altitude $\|\mathbf{w}(z)\|$ is related to the wind speed measured at a reference altitude $\|\mathbf{w}(z_r)\|$ according to the equation

$$\|\mathbf{w}(z)\| = \|\mathbf{w}(z_r)\| \frac{\log(z/z_0)}{\log(z_r/z_0)}, \tag{2.3}$$

where z_0 is the surface roughness length, in meters. According to [24], the surface roughness length over land depends on the surface cover and land use and is often difficult to estimate. A subjective way of determining this parameter is by a visual survey of the terrain around the region of interest and by consulting Table 2.1. As a rule-of-thumb, the parameter can be also approximated by one-tenth of the height of the surface roughness elements. For example, short grass of height 0.01m has a roughness length of approximately 0.001m. For heterogeneous surfaces, it is common to average the roughness lengths over all different subregions.

2.2.2 Wind profile power law

The wind profile power law relationship is often used as a substitute for the logarithmic wind profile when surface roughness or stability

Table 2.1: Surface roughness length for different terrain. Source: [1]

Terrain description	z_0 [m]
Water surfaces: seas and lakes	0.0002
Open terrain with smooth surface (concrete, airport runways, mown grass etc)	0.0024
Open agricultural land without fences and hedges	0.03
Agricultural land with a few buildings and hedges 1 km apart	0.055
Agricultural land with a few buildings and hedges 0.5 km apart	0.1
Agricultural land with many trees, bushes and plants	0.2
Towns, villages, agricultural land with many or high hedges, forests and very rough and uneven terrain	0.4
Large towns with high buildings	0.6
Large cities with high buildings and skyscrapers	1.6

information is not available. This model establishes a relationship between the absolute wind speed at any given altitude $\|\mathbf{w}(z)\|$ and the wind speed measured at a reference altitude $\|\mathbf{w}(z_r)\|$, according to the equation

$$\|\mathbf{w}(z)\| = \|\mathbf{w}(z_r)\| \, (\frac{z}{z_r})^{\alpha}, \tag{2.4}$$

where the exponent α is an empirically derived coefficient that varies dependent upon the stability of the atmosphere. For neutral stability conditions, α is approximately 0.143.

The log wind profile is generally considered to be a more reliable estimator of mean wind speed than the Wind profile power law in the lowest 10–20 m of the PBL. Between 20 m and 100 m both methods can produce reasonable predictions of mean wind speed in neutral atmospheric conditions. From 100 m to near the top of the PBL the power law produces more accurate predictions of mean wind speed, assuming neutral atmospheric conditions. In Figure 2.4, the differences in the wind profiles predicted by these two models are evidenced. This figure was generated considering smooth terrain conditions, $\alpha = 0.1$, $z_0 = 0.001$, $z_r = 2\ m$, and $w_r = 5\ m/s$.

2.3 Lagrangian mechanics

Although Newton's second law can be used to correctly describe the motion of a particle, or system of particles, it is not hard to find problems in which the particles are constrained to move in some complicated

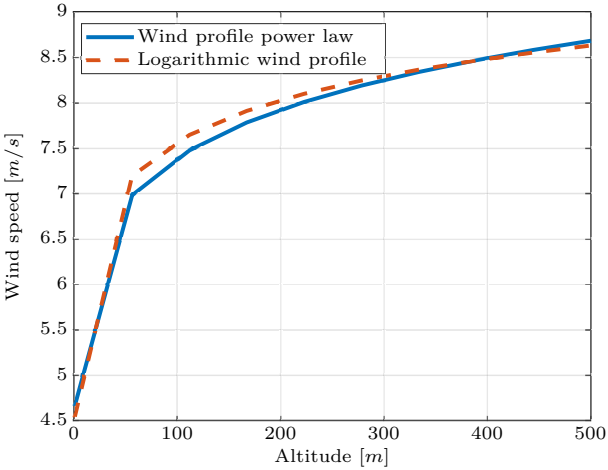

Figure 2.4: Logarithmic wind profile and the wind profile power law
Source: Original

manner, e.g. following the contours of a given surface. It might be the case that the forces keeping the particles on this surface are not easily expressible in Cartesian coordinates, or even impossible to model. Since the modeling procedure based on the Newtonian framework requires knowledge of all forces acting on the system, it can be completely unsuitable in such situations, or lead to equations that are too complex and difficult to manipulate.

This section presents an alternative approach for modeling systems that are hard to formulate using the Newtonian formalism. This new method is based on the so-called Hamilton's Principle, and can be applied to a much wider range of physical phenomena than Newton's theory. Through the application of Hamilton's Principle of Least Action, the derivation of the equations of motion, known in this framework as the Lagrange's equations, is straightforward. If the procedure is correctly followed, it yields a result equivalent to that obtained using Newton's laws, as expected.

Minimal principles in physics have a long and interesting story. The search for such principles is predicated on the notion that nature always minimizes certain important quantities when a physical process takes place [25].

In Lagrangian mechanics, the configuration of a system is described by an arbitrary, independent set of generalized coordinates $\mathbf{q} \in \mathbf{Q}$, where $\mathbf{Q}$ is the generalized coordinates space, constrained to evolve on a given manifold $\mathbf{c}(\mathbf{q}) = 0$ with $\mathbf{c} : \mathbf{Q} \to \mathbf{C}$, where $\mathbf{C}$ is the constrained coordinate space. The Lagrange function of the system is defined as

$$\mathscr{L}(\mathbf{q}, \dot{\mathbf{q}}, \mathbf{v}) = T(\mathbf{q}, \dot{\mathbf{q}}) - V(\mathbf{q}) - \mathbf{v}^T \mathbf{c}(\mathbf{q}) \tag{2.5}$$

where $T(\mathbf{q}, \dot{\mathbf{q}})$ is the kinetic energy of the system as function of its generalized coordinates and their derivatives, and $V(\mathbf{q})$ represents its potential energy as function of the generalized coordinates. Finally, $\mathbf{v}$ is the set of Lagrange multipliers associated to the constraints $\mathbf{c}$ to which the system is subject.

Hamilton's Principle, first published in a 1834 paper, and on which it is possible to base all of mechanics and most of classical physics, states that the development in time for a mechanical system is such that the integral of the difference between the kinetic and the potential energy is stationary. It can be shown that, based on this principle, the motion, or time trajectory $\mathbf{q}(t)$ of the modeled system can be mathematically obtained by solving the equations

$$\frac{d}{dt}\frac{\partial \mathscr{L}}{\partial \dot{\mathbf{q}}} - \frac{\partial \mathscr{L}}{\partial \mathbf{q}} = \mathbf{F}_q, \quad \mathbf{c}(\mathbf{q}) = 0 \tag{2.6}$$

where $\mathscr{L}$ is shorthand notation for $\mathscr{L}(\mathbf{q}, \dot{\mathbf{q}}, \mathbf{v})$, and $\mathbf{F}_q$ is the vector of generalized forces acting on the system. These forces are defined by the "virtual work" condition, i.e. for any infinitesimal displacement $\delta\mathbf{q}$ of the system configuration, yielding the work δw on the system, the equality $\delta w = \langle \delta\mathbf{q}, \mathbf{F}_q \rangle$ must hold.

The equations presented in this section should be enough for the reader to grasp all the modeling presented within this thesis. However, it is far from covering all the content necessary for understanding the theory behind these equations. If that is the interest of the reader, the material in [25, 26, 27] is recommended.

2.4 The estimation problem

Consider a N-point random data set $x[0], x[1], ..., x[N-1]$ which depends on a set of unknown parameters denoted by the vector θ. Esti-

mation refers then to the task of determining the value of the parameter based on the available data. More formally, it can be written as obtaining the estimator $\hat{\theta}$ given by

$$\hat{\theta} = g(x[0], x[1], ..., x[N-1]), \tag{2.7}$$

where g is some function.

The first step in determining a good estimator is to mathematically model the data. Because the data set is inherently random, it is usually described by its Probability Density Function (PDF), or $p(x[0], x[1], ..., x[N-1]; \theta)$. The PDF is, in turn, parameterized by the unknown parameter θ, and its specific format depends on previous knowledge about the available data.

Estimation based on PDFs in which the parameters of interest are assumed to be unknown, but deterministic is known as *classical* estimation. In some cases, however, there might be also some *a priori* information available about the parameters. For instance, one might know that a given parameter lies in a specific range, or has a known mean. This information can be incorporated into the estimator by assuming that the parameters are no longer deterministic, but random variables with their own PDFs. Such an approach is known as *Bayesian* estimation. The parameter is then viewed as a realization of the random variable θ, and the data is described by the joint PDF

$$p(\mathbf{x}, \theta) = p(\mathbf{x}|\theta)p(\theta), \tag{2.8}$$

where $p(\theta)$ is the prior PDF, summarizing the knowledge available about θ before any data are observed, and $p(\mathbf{x}|\theta)$ is a conditional PDF, summarizing the knowledge provided by the data conditioned on knowing θ. Once the PDF has been specified, the problem becomes one of determining an optimal estimator or function of the data, as in Equation 2.7.

According to [28], an estimator may be thought of as a rule that assigns a value to θ for each realization of $\mathbf{x}$.

2.4.1 Optimal estimation

This section introduces two theorems of optimum estimation theory required for the comprehension of the Kalman filter. For the sake of

simplicity, only scalar random variables are considered. Nonetheless, the generalization to the multivariate case is straightforward.

Suppose we are given an observation

$$y_k = x_k + v_k, \tag{2.9}$$

where x_k is an unknown signal and v_k is an additive noise component. The variable $\hat{x}_k$ denotes the a posteriori estimate of the signal x_k given the observations $y_1, y_2, \ldots y_k$. Let us define a cost, or loss function given by the mean square error between the actual value of x_k and the estimated signal $\hat{x}_k$.

$$J_k = E[(x_k - \hat{x}_k)^2] = E[\tilde{x}_k^2], \tag{2.10}$$

where E is the expectation operator. Note that the cost function is nonnegative, and a nondecreasing function of the estimation error $\tilde{x}_k = x_k - \hat{x}_k$. This specific kind of cost function is known as the mean-square error.

Theorem 1 (***Conditional mean estimator***)**.** *Given the stochastic processes x_k and y_k of Equation 2.9, then the optimum estimate $\hat{x}_k$ that minimizes the mean-square error J_k is the conditional mean estimator:*

$$\hat{x}_k = E[x_k | y_1, y_2, \ldots y_k]$$

Theorem 2 (***Principle of orthogonality***)**.** *Let the stochastic processes x_k and y_k be of zero means; that is,*

$$E[x_k] = E[y_k] = 0 \quad \textit{for all} \quad k$$

Then if the optimal estimate $\hat{x}_k$ is restricted to be a linear function of the observables and the cost function is the mean-square error, then the optimum estimate $\hat{x}_k$, given the observations $y_1, y_2, \ldots, y_k$ is the orthogonal projection of x_k on the space spanned by these observations.

2.4.2 Kalman filter

The celebrated Kalman filter, rooted in the state-space formulation of linear dynamical systems, provides a recursive solution to the linear optimal filtering problem. It applies to stationary as well as to nonstationary environments. The solution is recursive in that each updated

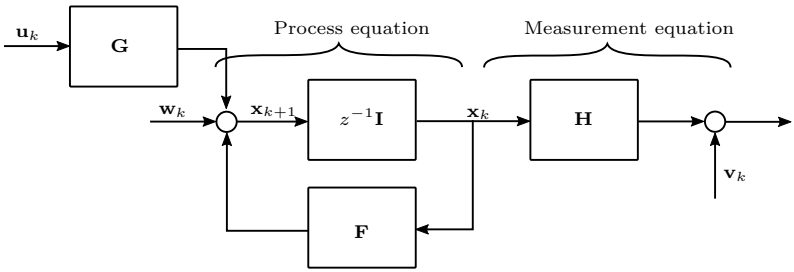

Figure 2.5: Block diagram of a generic linear, discrete-time dynamical system

estimate of the state is computed from the previous estimate and the new input data, so only the previous estimate requires storage. In addition to eliminating the need for storing the entire past observed data, the Kalman filter is computationally more efficient than computing the estimate directly from the entire past observed data at each step of the filtering process [29]. This section provides an overview of the Kalman algorithm, and is heavily based on [29], except for minor changes in notation, which has been adapted to conform to the conventions adopted in this document.

Consider a linear, discrete-time dynamical system, which is described by the block diagram in Figure 2.5. The state vector, or simply state, is denoted by $\mathbf{x}_k$, and is defined as the minimal set of data that is sufficient to uniquely describe the dynamic behavior of the system. It can also be seen as the least amount of data on the past behavior of the system that is needed to predict its future behavior. Typically, the state $\mathbf{x}_k$ is unknown, and in order to estimate its value one has to rely on the information available about the system, also known as the observed data, which is denoted by $\mathbf{y}_k$.

The block diagram of Figure 2.5 can be mathematically described by the following pair of equations:

(i) *Process equation*

$$\mathbf{x}_{k+1} = \mathbf{F}\mathbf{x}_k + \mathbf{G}\mathbf{u}_k + \mathbf{w}_k \tag{2.11}$$

where $\mathbf{F}$ is the transition matrix taking the state $\mathbf{x}_k$ from time k to time $k+1$, and $\mathbf{G}$ is the so-called input matrix, which accounts for the effects of the input vector $\mathbf{u}_k$ in the system. The vector

$\mathbf{w}_k$ corresponds to an additive, white, and Gaussian zero mean process noise, with covariance matrix defined by

$$E[\mathbf{w}_n \mathbf{w}_k^T] = \begin{cases} \mathbf{Q}, & \text{for } n = k \\ \mathbf{0}, & \text{for } n \neq k \end{cases} \tag{2.12}$$

where the dimension of the state space is denoted by M.

(*ii*) *Measurement equation*

$$\mathbf{y}_k = \mathbf{H}\mathbf{x}_k + \mathbf{v}_k \tag{2.13}$$

where $\mathbf{y}_k$ is the observation vector at time k and $\mathbf{H}_k$ is the measurement matrix. The measurement noise $\mathbf{v}_k$ is assumed to be additive, white, and Gaussian, with zero mean and with covariance matrix defined by

$$E[\mathbf{v}_n \mathbf{v}_k^T] = \begin{cases} \mathbf{R}, & \text{for } n = k \\ \mathbf{0}, & \text{for } n \neq k \end{cases} \tag{2.14}$$

Moreover, it is also assumed that the measurement noise $\mathbf{v}_k$ is uncorrelated with the process noise $\mathbf{w}_k$. The dimension of the measurement space is denoted by N.

The Kalman filtering problem can then be stated as follows: *Given a set of observed data* $\mathbf{y}_1, \mathbf{y}_2, \ldots \mathbf{y}_k$*, find for each* $i \geq 1$ *the minimum mean-square error estimate of the state* $\mathbf{x}_i$.

This problem is called filtering if $i = k$, prediction if $i > k$, and smoothing if $1 \leq i \leq k$.

Suppose that a measurement of a linear dynamical system, described by Equations 2.11 and 2.13 has been made at time k. The requirement is to use the information contained in the new measurement $\mathbf{y}_k$ to update the estimate of the unknown state $\mathbf{x}_k$.

The standard Kalman filter achieves this with a two stage algorithm. In the first stage, known as the prediction stage, the filter utilizes the knowledge about the dynamics of the system, which is embedded in the matrix $\mathbf{F}$, to propagate in time the previous estimate $\hat{\mathbf{x}}_{k-1}$, and obtain a prediction of the current state. The state resulting from this

propagation is referred to as the *a priori* estimate $\hat{\mathbf{x}}_k^-$, i.e. the estimate before any measurement has been considered. Besides the state vector, the filter also predicts, based on the previous estimate, on the available dynamics, and on the uncertainty of the model, the covariance matrix associated with the state. As it happens with the predicted state, this covariance is called the *a priori* state covariance, and therefore denoted $\mathbf{P}_k^-$.

In the subsequent filtering, or update stage of the algorithm, the *a priori* state and covariances are refined based on the observations of the system, resulting in the so called *a posteriori* state vector and covariance matrix, $\hat{\mathbf{x}}_k$ and $\mathbf{P}_k$, respectively. How exactly this refinement takes places depends on the uncertainties associated with the process model used in the prediction phase, and on those associated with the measurement data. Basically, measurements having large discrepancies when compared to their expected value, calculated from the *a priori* state through the observation model, or those with large uncertainties, will have less influence on the resulting state estimate. This influence of the different measurements is determined by the algorithm in an optimal way at every time step as the weight matrix $\mathbf{K}_k$, known as the Kalman gain matrix. The algorithm just described can be formalized as

Initialization

For $k = 0$, set

$$\begin{aligned} \hat{\mathbf{x}}_0 &= E[\mathbf{x}_0] \\ \mathbf{P}_0 &= E[(\mathbf{x}_0 - E[\mathbf{x}_0])(\mathbf{x}_0 - E[\mathbf{x}_0])^T] \end{aligned} \tag{2.15}$$

Computation

For $k = 1, 2, ...$, compute:

- State estimate and error covariance propagation:

$$\begin{aligned} \hat{\mathbf{x}}_k^- &= \mathbf{F}\hat{\mathbf{x}}_{k-1} + \mathbf{G}\mathbf{u}_{k-1} \\ \mathbf{P}_k^- &= \mathbf{F}\mathbf{P}_{k-1}\mathbf{F}^T + \mathbf{Q} \end{aligned} \tag{2.16}$$

- Kalman gain matrix computation:

$$\mathbf{K}_k = \mathbf{P}_k^- \mathbf{H}^T (\mathbf{H}\mathbf{P}_k^- \mathbf{H}^T + \mathbf{R})^{-1} \tag{2.17}$$

- State estimate and error covariance update:

$$\begin{aligned} \hat{\mathbf{x}}_k &= \hat{\mathbf{x}}_k^- + \mathbf{K}(\mathbf{y}_k - \mathbf{H}\hat{\mathbf{x}}_k^-) \\ \mathbf{P}_k &= (\mathbf{I} - \mathbf{G}_k\mathbf{H})\mathbf{P}_k^- \end{aligned} \tag{2.18}$$

2.4.3 Extended Kalman filter

The Kalman Filter (KF) is the minimum-variance state estimator for linear dynamic systems with Gaussian noise. Even if the noise is non-Gaussian, the KF is the best linear estimator. For nonlinear systems, in which neither the evolution of the states in time nor the measurements can be expressed by a matrix multiplication, it is not possible, in general, to derive the optimal state estimator in closed form. In such situations, however, various modifications of the KF can be used to estimate the state. These modifications include the EKF, the Unscented Kalman Filter (UKF), and the particle filter [30]. The EKF is one of the most widely adopted variants of the KF. It assumes that the system can be modeled as

$$\begin{aligned} \mathbf{x}_{k+1} &= \mathbf{f}(\mathbf{x}_k, \mathbf{u}_k) \\ \mathbf{y}_k &= \mathbf{h}(\mathbf{x}_k, \mathbf{u}_k) \end{aligned} \tag{2.19}$$

Provided that these functions are differentiable, a first order Taylor expansion is then used to approximate their derivatives at each time step

$$\begin{aligned} \tilde{\mathbf{F}}_{k-1} &= \left.\frac{\partial \mathbf{f}(\mathbf{x}_k, \mathbf{u}_k)}{\partial \mathbf{x}}\right|_{\hat{\mathbf{x}}_{k-1}, \mathbf{u}_{k-1}} \\ \tilde{\mathbf{H}}_k &= \left.\frac{\partial \mathbf{h}(\mathbf{x}_k)}{\partial \mathbf{x}}\right|_{\hat{\mathbf{x}}_k^-} \end{aligned} \tag{2.20}$$

which are finally employed in the standard KF algorithm. Note that if the state transition and observation models are both linear, the EKF

is identical to the original algorithm. One of the main disadvantages of the EKF is that it does not offer any kind of convergence or optimality guarantees. Moreover, depending on the nonlinear characteristics of $\mathbf{f}$ and $\mathbf{h}$, the approximations of derivatives of these functions by a first-order Taylor expansion might be off by a significant amount, which could lead to errors and ultimately to divergence.

2.4.4 Constrained estimation with the Kalman filter

Although the KF and its extended variants are powerful tools for state estimation, they might not be able to directly incorporate all information available about a system. For example, one may know that the states satisfy equality or inequality constraints. In this case the KF can be modified to exploit this additional information and get better filtering performance than the original formulation [30]. If the system is nonlinear, the KF variations are not necessarily minimum variance, so it is not surprising that improvements can be seen by incorporating state constraints in the filter. Even if the system is linear, if there are additional constraints beyond those explicitly given in the model, the complete system description is different than that given by the standard equations, and a modified version of the filter may result in improved performance.

According to the survey presented in [30], linear constraints can be enforced in the linear KF through several different techniques such as model reduction, perfect measurements, estimate projection, gain projection, PDF truncation, and system projection. The same survey also discusses approaches that can be employed in the case of nonlinear constraints, including second-order expansion, the smoothly constrained KF, the Moving Horizon Estimator (MHE), modified versions of the UKF, interior point approaches, and particle filters. Since under certain conditions several of these strategies are equivalent and result in the same estimate, due to its simplicity only the perfect measurement technique is considered in this work. If the reader is interested in studying other alternatives for the enforcement of state constraints in a KF scenario, the survey in [30] is strongly recommended as a starting point.

2.4.4.1 Perfect measurement technique

Provided that information is available about a system in the form of a linear equality constraint involving its states, and that these constraints can be written as

$$\mathbf{D}\mathbf{x} = \mathbf{d}\,, \tag{2.21}$$

where $\mathbf{D}$ is a known matrix and $\mathbf{d}$ is a known vector, then they can be incorporated into the KF as perfect measurements. The idea behind this simple technique is basically to augment the observation vector with the information contained in the constraints, and treat them as measurements with zero, or negligible, measurement noise:

$$\begin{bmatrix}\mathbf{y}_k \\ \mathbf{d}\end{bmatrix} = \begin{bmatrix}\mathbf{H} \\ \mathbf{D}\end{bmatrix}\mathbf{x}_k + \begin{bmatrix}\mathbf{v}_k \\ \mathbf{0}\end{bmatrix}. \tag{2.22}$$

The fact that the components of the measurement equation corresponding to the constraints are noise free will result in a posteriori KF estimate of the state that is consistent with them [30], meaning that the *a posteriori* estimated state $\hat{\mathbf{x}_k}^+$ will satisfy $\mathbf{D}\hat{\mathbf{x}_k}^+ = \mathbf{d}$.

The state constraints can also be nonlinear. In these cases, instead of $\mathbf{D}\mathbf{x}_k = \mathbf{d}$ we have

$$\mathbf{c}(\mathbf{x}_k) = \mathbf{p}, \tag{2.23}$$

where $\mathbf{c}$ is a known function, and $\mathbf{p}$ is a known vector. If the constraint is linearized around $\mathbf{x}_k^-$, and the second-order terms are neglected, one ends up with

$$\mathbf{c}'(\hat{\mathbf{x}}_k^-)\mathbf{x}_k = \mathbf{p} - \mathbf{c}(\hat{\mathbf{x}}_k^-) + \mathbf{c}'(\hat{\mathbf{x}}_k^-)\hat{\mathbf{x}}_k^-. \tag{2.24}$$

This equation is equivalent to the linear constraint $\mathbf{D}\mathbf{x}_k = \mathbf{d}$ if

$$\begin{aligned}\mathbf{D} &= \mathbf{c}'(\hat{\mathbf{x}}_k^-) \\ \mathbf{d} &= \mathbf{p} - \mathbf{c}(\hat{\mathbf{x}}_k^-) + \mathbf{c}'(\hat{\mathbf{x}}_k^-)\hat{\mathbf{x}}_k^-\end{aligned} \tag{2.25}$$

Therefore the same perfect measurement technique applicable to linear constraints can be also employed in situations in which these constraints are nonlinear, after they are linearized.

The perfect measurement approach has the advantage of not changing the state equation, which makes it easy to implement. Moreover, it allows the filter to cope with situations in which the constraints are not always present.

2.5 Wireless positioning systems

Positioning systems aim at determining the location of a target object either relative to a known position or within a coordinate system [31], and can be classified in two major groups, namely global- and local positioning systems. While the former concerns about determining the absolute coordinates of a target in the terrestrial globe, the latter aims at localizing it with respect to an arbitrary known reference. Local positioning systems can be further divided into self- and remote positioning system, according to the ability of the target to find its own position at any given time and location. In remote positioning systems, other nodes are required for determining the relative position of a target located in their coverage area either actively, i.e. with the target cooperating to the localization process, or in a passive fashion, in which the target is noncooperative and possibly even unaware of the existence of other devices.

The basic elements of any positioning systems are: the sensing devices, responsible for obtaining data related to the unknown location or motion of the target; and a positioning algorithm, which uses these data to compute its coordinates. This section is intended to provide the reader with a minimum background on wireless positioning systems necessary for the comprehension of the thesis and of the design choices that will be presented later in the text. More specifically, it focuses on systems based on radio-frequency technologies, even though there are several other solutions in the literature that can too be classified as wireless (e.g. inertial measurement systems, vision systems, etc). The content presented is, therefore, by no means an extensive overview and, for a more comprehensive presentation of the vast universe of positioning systems, one should refer to [31].

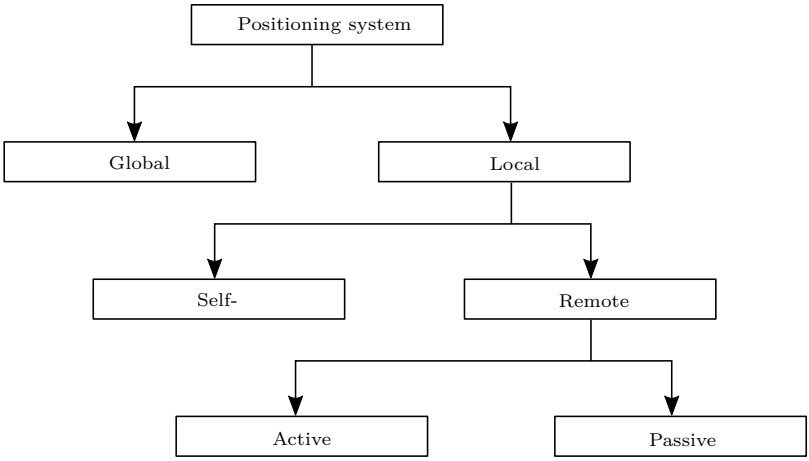

Figure 2.6: Positioning systems classification.
Source: Adapted from [31]

2.5.1 Radio-frequency positioning

A positioning system in which the sensing devices extract their measurements from radio-frequency (RF) signals is known as a RF positioning system. Besides the categories previously described and shown in Figure 2.6, such systems also differ in terms of the specific technique used to sense and measure the position of the target within the environment. According to [32], there are four major techniques employed for this purpose, including nearest cell, lateration, angulation, and pattern recognition, although it is also common to find solutions in which these methods are combined, resulting in a hybrid system.

One of the simplest mechanisms for estimating approximate location of a RF device in situations in which a cellular network infrastructure is available is the concept of nearest-cell, or cell of origin. In its simplest form, this technique makes no explicit attempt to resolve the position of the mobile device beyond indicating the cell within the infrastructure with which it is registered. Although easy to implement, since it does not require any complicated algorithms, this solution has the drawback of having a coarse granularity, and its accuracy depends on a series of factors such as the number of cells in the infrastructure and the size of each cell. Besides, without a distance metric, it cannot guarantee that

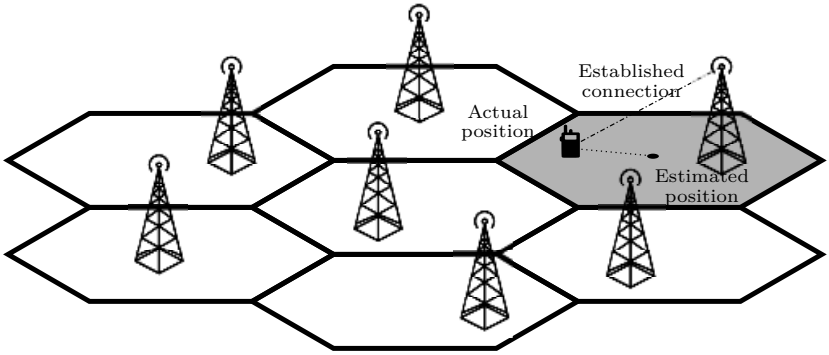

Figure 2.7: Nearest-cell positioning concept

the mobile devices will always be associated with the closest cell, which might result in poor accuracy.

Pattern recognition techniques are based on the recording of radio signal behavior patterns in different locations of specific environments, and later comparing these patterns to those measured by a target in order to determine its position. These two stages are known as calibration and operation phases, respectively. The technique does not rely on any specific hardware, and may be implemented totally in software, provided that the RF signal characteristics are accessible to the programmer, which can significantly reduce complexity and cost compared to angulation and time-based lateration. Solutions based on pattern recognition assume that each location in the environment of interest has a unique RF "signature". Therefore, its performance is strongly associated to the validity of this assumption, and is normally maximum immediately after a calibration. At that time, the information is current and indicative of conditions within the environment. As time progresses and changes occur that affect RF propagation, accuracy can be expected to degrade in accordance with the level of environmental change [32]. Other drawbacks of the technique include the effort necessary for the calibration phase, which depends on the size and complexity of the environment, and also the impossibility to re-use the calibration maps.

As the name suggests, angulation techniques are based on measurements of the angle, or direction at which a radio signal reaches a series

of receiving stations, also known as angle-of-arrival (AOA) or direction-of-arrival (DOA) measurements. These measurements are obtained by moving antennas capable of automatically following the direction of the target based on time delay, phase shift, frequency shift, or amplitude of the received signal, or by complex, and costly antenna arrays, which determine the angle indirectly by measuring these quantities at each individual array element. Assuming the location of the reference stations are known, geometric relationships are used to estimate location from the intersection of lines defined by the measured angles. If there are at least three receiving stations available, the resulting estimate is unique. Note that, although there is no need of accurate time synchronization between receivers, since they are geographically apart, their measurements might need to be sent to a remote processing station, which requires a communication infrastructure. According to [33], angle-of-arrival positioning is commonly used to locate illegal transmitters, both broadcast and those used for eavesdropping, and for tracking wild animals that are tagged with tiny transmitters. It is not restricted by the problems dictating conditions of use of other location methods. It requires no cooperation from the target, and any type of signal can be used. It is also used over wide frequency bands and ranges. Angulation techniques are very dependent on the quality of the direction measurements, hence on the characteristics of the moving antennas or antenna arrays chosen for the implementation.

Finally, lateration, or distance-based techniques rely on range, or distance measurements between a moving target and a series of known reference points, which are usually known as anchors. Once obtained, these measurements are then fed to a positioning algorithm, which is responsible for combining them and yielding an estimate of the target location. According to [33], there are two main lateration modes, namely multilateration and unilateration. In a multilateral system the mobile target works as a transmitter, whose beacons are received by each of the fixed anchors, which can then process these signals and estimate the target's location, whereas in unilateration systems the mobile target works as the receiver.

The Angle-of-arrival (AOA) is the common metric used in direction-based systems, whereas the Receiver signal strength (RSS), Time-of-flight (TOF), carrier signal Phase-of-arrival (POA), Time-of-arrival (TOA),

Time-difference-of-arrival (TDOA), and Frequency-difference-of-arrival (FDOA) of the received signal are a few of the metrics employed in distance-based solutions. Which metrics should be measured depends on the positioning algorithms. For a more extensive survey of the metrics, a reading of [33, 34, 35] is suggested.

Range and angle measurements used for localization are measured in a physical medium that introduces errors. Generally, these measurements are impacted by both time-varying errors and static, environment-dependent errors. Time-varying errors, e.g. due to additive noise and interference, can be reduced by averaging multiple measurements over time. Environment dependent errors are the result of the physical arrangement of objects, e.g. buildings, trees, and furniture, in the particular environment in which the sensor network is operating. Since the environment is unpredictable, these errors are unpredictable and must be modeled as random [36].

CHAPTER 3

Airborne wind energy systems

Airborne Wind Energy (AWE) systems harvest wind power by exploiting the aerodynamic forces acting on lightweight suspended structures anchored to the ground by means of one or more tethers. This technology is able to reach higher altitudes than conventional wind turbines, where the wind is generally stronger and more consistent, while allowing for a reduction in the construction and installation costs of the power plant, among other advantages as discussed in [8, 11, 22, 37, 38, 39].

Research on AWE systems started in the early eighties, with the seminal work in [39], and despite the apparent abandonment during the nineties, the field recovered and experienced an extremely rapid expansion in the last decade. To this date, a large number of systems based on radically different concepts have already been analyzed and tested by several different institutions worldwide, which are also responsible for hundreds of patents and scientific papers directly related to the technology.

Research teams and companies all over the world are currently working on different aspects of the technology including control, electronics and mechanical design [8]. According to a survey conducted by the AWESCO, an european collaboration network aimed at pushing the

Figure 3.1: Institutions involved with Airborne wind energy worldwide as of June 2015

Source: [40]

AWE technology forward, at the beginning of 2015 there were at least 55 academic and industrial institutions around the world actively involved with research and development in the field. These institutions, shown in Figure 3.1, have been attracting a considerable amount of investment from both the public and the private sector. Note that, besides research groups and universities, there are also several companies involved with AWE. For these companies, obtaining safety certifications and operation authorization from the governmental agencies is extremely important in order for them to commercialize their products, and this must be kept in mind when proposing solutions to the technical challenges involved in AWE.

According to [7], there are three major reasons for the interest in AWE for electricity production: first, like solar, wind power is one of the few renewable energy resources that is in principle large enough to satisfy all of humanity's energy needs; second, in contrast to ground-based wind turbines, AWE devices might be able to reach higher altitudes, tapping into a large and so far unused wind power resource; and finally,

AWE systems might need less material investment per unit of usable power than most other renewable energy sources. This saving in material comes at a cost, however: while a conventional wind turbine is a stationary construction on the ground, an AWE system needs to fly to maintain its shape: an intrinsically stable system was exchanged by an intrinsically unstable one [7].

3.1 Constructive concepts

According to [8], on which this chapter is heavily based, AWE systems generally comprise two main components: a ground unit, and at least one aircraft that are mechanically or sometimes even electrically connected by ropes, often referred to as tethers. Among the different concepts, one can distinguish ground-generation systems, in which the conversion of mechanical energy into electrical energy takes place on the ground, and airborne-generation systems, in which the conversion happens at the aircraft and the electricity is transferred to the ground through the tether.

Ground-generation AWE systems can be further split into two separate groups. In the first group, the ground station is fixed, while in the other it is allowed to move. Airborne-generation AWE systems can, in turn, be classified as crosswind or non-crosswind devices. The classification of AWE systems is depicted in Figure 3.2.

In the literature, ground and airborne generation concepts may also be referred to as lift- and drag-modes, respectively. While the former is labeled after the component of the aerodynamic force it relies on to generate electricity, the latter receives its name due to the drag added to the aircraft by the on board turbines (even though their rotation is an effect of the aerodynamic lift of the blades).

3.1.1 Ground-generation

In a ground-generation AWE system, electrical energy is produced on the ground by mechanical work done by traction force resulting from the interaction of the wind and the aerodynamic characteristics of the suspended aircraft. The traction force is transmitted to the ground through one or more tethers, which are attached to the electricity generation mechanism.

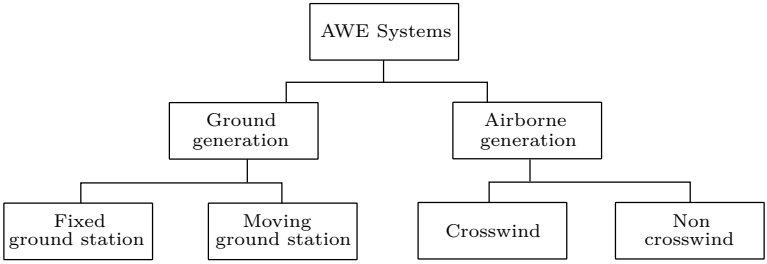

Figure 3.2: Taxonomy of AWE systems
Source: Adapted from [8]

Ground-generation AWE systems with a fixed ground station represent the most common concept within the AWE community. The operation of these devices comprises a two-phase cycle. In the first phase, known as the traction, active, or generation phase, the aircraft is driven in a way to produce a lift force, and consequently a traction force on the tethers, which in turn induce the rotation of electrical generators. In the retraction, passive, or recovery phase, motors rewind the ropes thereby bringing the aircraft back to its original position with respect to the ground. In order to have a positive balance, the net energy produced in the generation phase has to be larger than the energy spent in the recovery phase. This positive balance must be guaranteed by the control systems, which are responsible for adjusting the aircraft's aerodynamic characteristics through the manipulation of control variables aiming at keeping it in flight and also at maximizing the cycle power.

The trajectory followed by the aircraft during the active phase can vary, and has direct implication in the amount of power harvested from the wind, as it influences the magnitude of the lift force. The most adopted mode of flight in this category of AWE systems is the crosswind flight, which consists of flying with a significant component of the prevailing wind perpendicular to the airfoil surface area, in order to maximize the so called apparent wind and therefore the traction force on the tether. In practice, this generally results in a circular or eight-shaped trajectory. Even though it demands more actuation effort, the latter is usually preferred in order to avoid accumulated torsion on the tether and eliminate the need of an additional mechanism. Because of

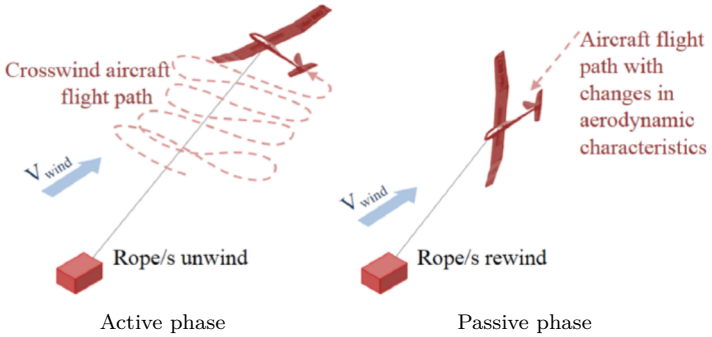

Figure 3.3: Operation phases of a ground-generation AWE system with fixed ground station

Source: [8]

their unique constructive characteristics and behavior when in operation, AWE devices with ground-generation and a fixed ground station also receive the name of pumping-kites.

AWE systems with a moving ground station are built aiming at producing an always positive power, rather than a cyclic power as what happens with pumping-kite systems. While this allows for a simplification of the electronics required for the connection of such systems to the grid, it makes them more complex, and hence more difficult to build and deploy successfully. According to [8], currently there are no working moving ground station AWE systems, and a single prototype is under construction.

As mentioned earlier in the text, ground-generation AWE systems make use of the lift component of the aerodynamic forces acting on the airfoil to pull a load on the ground, moving a generator and producing electrical power. Within the lift operation mode, however, there are a number of possibilities for choosing the type of aircraft to be connected to the ground station, and each option has its own particular set of advantages and drawbacks. In general, the aircraft can be either rigid, and similar in design to an airplane, or flexible, resembling the kites used in kite surfing. As a rule of thumb, rigid wings have a better aerodynamic efficiency, i.e. their lift-to-drag ratio is larger than that of a flexible kite, and their modeling and control are simpler. On the other hand, they can be much more expensive to build, less resistant

to impacts, and cause more severe damage in the case of a collision. As the technology matured towards a more industrial level, and issues such as the fully autonomous operation started to become a concern, many AWE groups have demonstrated a preference for rigid or semi-rigid aircraft, which besides having a more predictable behavior, were also shown to greatly reduce the complexity of the autonomous take-off and landing.

The most common types of aircraft employed in AWE applications include the Leading Edge Inflatable (LEI) kites, which are single layer kites whose stiffness is enhanced by inflatable structures on the leading edge; Foil kites, also known as ram-air kites, which are double-layer kites with cells that inflate during flight and give the kite the necessary stiffness; Delta kites, which are made of a single layer of fabric material reinforced by a rigid frame; Gliders, which are rigid wings with an excellent aerodynamic performance, although heavy and expensive; Swept rigid wings, which are basically gliders without fuselage and tail control; and Semi-rigid wings, a novel aircraft design within AWE, composed of multiple short rigid modules that are hinged to each other, resulting in a structure lighter than that of a straight rigid wing and more aerodynamically efficient and durable than that of fabric kites. With respect to LEI kites, foil wings have a better aerodynamic efficiency, and can be one order of magnitude larger in size. Delta kites have better aerodynamics than the LEI and foil variants, but their rigid frames have to be constructed in such a way that it resists the mechanical bending stresses, which in turn increases the aircraft weight, cost, and minimum take-off wind speed. Another important aspect of aircraft design is durability. While LEI, foil, and delta kites have their performance compromised after around several hundred hours, rigid wings offer a much larger lifespan, usually of several decades.

In ground-generation AWE systems, the aircraft is connected to the ground by at least one power rope that is responsible for transmitting the lift force to the ground station. As the pumping cycle occurs, the flight trajectory must be controlled to ensure a safe flight and to maximize the cycle power. In order to accomplish that, a series of different approaches can be employed to change the aerodynamic characteristics of the aircraft and hence its dynamic behavior. The most common strategies are to move actuators similar to ailerons on the aircraft, or

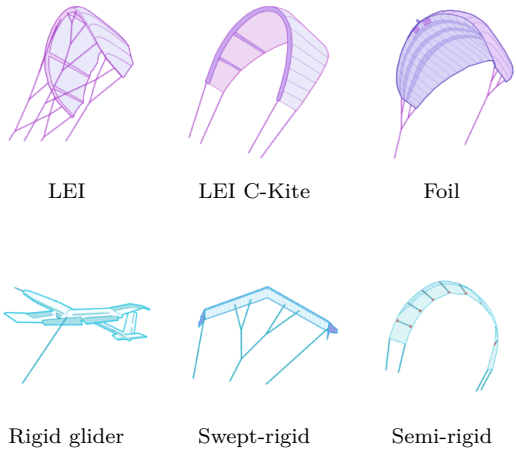

Figure 3.4: Aircraft in ground-generation AWE systems
Source: [8]

to pull lines attached to it changing their relative length and ultimately the wing displacement with respect to the wind for changing its course or angle-of-attack.

In the latter approach, the pulling of the lines can be performed either by actuators mounted on a small structure known as control pod, or control unit, flying right below the aircraft, or placed on the ground station. Although the control pod has the potential of eliminating the command delay introduced by long tethers, it might change the dynamics and the efficiency of the system due to its mass and drag, and require additional infrastructure for communication depending on where the control algorithms responsible for generating the inputs for the actuators are executed. The different actuation strategies commonly seen in AWE systems are presented in Figure 3.5.

Since they are connected to the ground station by a single tether, suspended actuation structures eliminate the increased aerodynamic drag caused by multiple lines, and can potentially increase the velocity of the aircraft. On the other hand, the control unit introduces an extra mass and a new drag surface into the system, affecting its dynamic behavior and efficiency. Moreover, the suspended actuation unit must be powered either by batteries – which must be recharged, possibly by

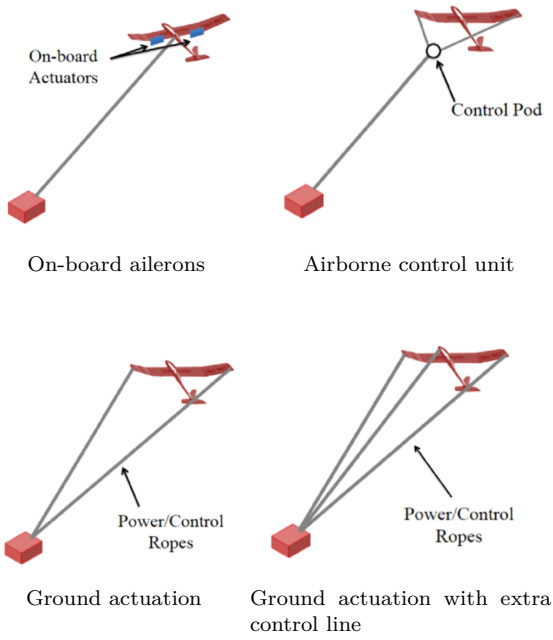

Figure 3.5: Actuation strategies in ground-generation AWE systems
Source: [8]

an on board turbine attached to the control pod or through the main tether, increasing the overall complexity of the system. The choice of an actuation strategy is a trade-off decision that must be taken carefully considering many different aspects.

A simpler solution is to keep the actuators on the ground. Due to the length of the tethers, however, this introduces a transport delay into the system, and might severely impact the performance of the controllers, not to mention the additional drag of the extra tether.

3.1.2 Airborne-generation

In an airborne-generation scenario, electrical energy is produced on the aircraft and it is transmitted to the ground via a special tether which carries electrical cables. In this case, electrical energy conversion is generally achieved using wind turbines. AWE systems based on this

concept continuously produce electric power while in operation, except during take-off and landing maneuvers, during which the on board turbines operate as motors, consuming energy. This configuration greatly simplifies the launching and landing of the aircraft, at the expense of having to transmit electricity to the ground through the main tether.

As presented in Figure 3.6, regarding the aircraft, airborne-generation AWE systems can be further classified into three separate groups according to their flying principle: wings lift, which is achieved with a tethered flight of special gliders or frames with multiple wings; buoyancy and static lift, achieved with aerodynamically shaped aerostats filled with lighter-than-air gas; and rotor thrust, which is achieved with the same turbines used for electrical power generation. Except for the buoyant aerostats, all other wings in an airborne-generation scenario must be rigid, in order to sustain the rotors and the connected electric generators [38].

Buoyant aerostats suspended by aerostatic lift forces are perhaps the AWE concept with greater similarity to conventional wind power technology. The working principle of these devices is the same of the tower-based turbines, except that the electric energy is transmitted to the ground through the tether, which can be reeled out to a very large length, possibly in the order of kilometers.

If the reader is interested in obtaining more details about the constructive concepts chosen by the different companies and research institutions working with AWE for their prototypes, the material in [8], [22], and [37] is recommended.

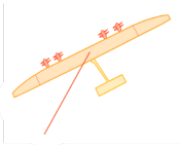

Plane with turbines

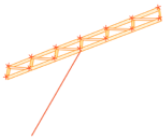

Frame of wings and turbines

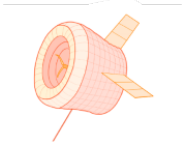

Lifting aerostat with turbine

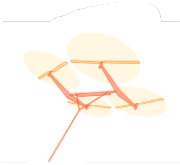

Static suspension quadrotor

Figure 3.6: Aircraft in airborne-generation AWE systems
Source: [8]

CHAPTER 4

Related work

In recent years, research and development of the AWE technology has picked up pace both in academia and industry. This growing interest is mainly motivated by the potential of AWE to, hypothetically, yield a lower levelized cost of energy than the current de-facto technology, which requires a heavy, expensive concrete tower for supporting the turbine. Despite the promising outlook in terms of economical feasibility, AWE technology is currently at an intermediate development stage, with several challenges yet to be overcome before it can reach the market.

This chapter presents a literature review of topics such as modeling, control, optimization, and estimation in AWE systems. More than a source of motivation for this thesis, they inspired and guided the development of the estimation structures that will be described in detail in the upcoming chapters. Hopefully, by finishing the text, the reader will have a better comprehension of the importance of reliably determining the aircraft position, the aerodynamic parameters, and the wind conditions at flight level, and will be able to compare and understand the main advantages of the proposed solution over other existing approaches.

4.1 Modeling

Modeling is a crucial element of AWE for system analysis, simulation, optimization, and control. AWE devices are intricate mechanical systems, where the winch, tethers, and wings interact dynamically to yield complex, fast and nonlinear dynamics [26]. Many models have been proposed in the literature to describe the behavior of a tethered aircraft in several levels of accuracy and for different steering mechanisms. The most complex models are able to describe the aerodynamics and deformations of the wing in detail, yet at a high computational cost. As a consequence, they are strictly oriented to simulation. Models with intermediate levels of complexity still achieve a reasonable level of detail and thus can be used for faster, real-time simulations. The simplest models are more appropriate for analytical tasks such as optimization and control design [37].

4.1.1 Single particle models

The model presented in [5, 19] is built upon a simpler version published in [41], and aims at describing a tethered airfoil in a pumping-kite configuration by a set of six dynamic states, namely the azimuth ϕ and polar θ angles, and the tether length l, together with their first-order time derivatives. The airfoil is represented as a single equivalent point mass m at Cartesian coordinates $\mathbf{r}$, which is subject to aerodynamic, gravitational, apparent, and line traction forces. This point mass is assumed to be anchored to the ground by a rigid segment of variable length $r = \|\mathbf{r}\|$, subject to aerodynamic drag and gravitational forces only. Unlike its predecessor, this model considers variations of the airfoil angle of attack, leading to more accurate results.

The model in [19] initially defines two reference frames: the *inertial* reference frame $(\mathbf{e}_x, \mathbf{e}_y, \mathbf{e}_z)$, which is centered at the system anchorage point on the ground, and whose $\mathbf{e}_x$ and $\mathbf{e}_z$ axes are aligned with the nominal wind vector $\mathbf{w}_n^l = [w_{nx}, 0, 0]^T$ and with the negative of the gravity vector $\mathbf{g}$, respectively; the *local* reference frame $(\mathbf{e}_\theta, \mathbf{e}_\phi, \mathbf{e}_r)$, centered at the aircraft center of gravity and whose axes are defined as $\mathbf{e}_\theta = \frac{d\mathbf{r}}{d\theta}\frac{1}{r}$, $\mathbf{e}_\phi = \frac{d\mathbf{r}}{d\phi}\frac{1}{r\sin\theta}$, and $\mathbf{e}_r = \mathbf{e}_\theta \times \mathbf{e}_\phi$. Note that the unit vectors $\mathbf{e}_\theta, \mathbf{e}_\phi, \mathbf{e}_r$ can be expressed in the inertial frame by the columns of the rotation matrix

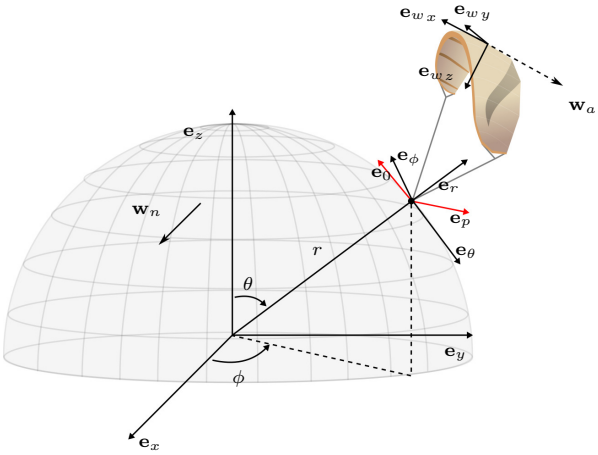

Figure 4.1: Single-point mass model representation with a rigid tether
Source: Original

$$\mathcal{R}_i^l = \begin{bmatrix} \mathbf{e}_\theta & \mathbf{e}_\phi & \mathbf{e}_r \end{bmatrix} = \begin{bmatrix} \cos\theta\cos\phi & \cos\theta\sin\phi & -\sin\theta \\ -\sin\phi & \cos\phi & 0 \\ \sin\theta\cos\phi & \sin\theta\sin\phi & \cos\theta \end{bmatrix}^T \tag{4.1}$$

which can be also used to transform vectors from the local to the inertial frame as in $\mathbf{v}^i = \mathcal{R}_i^l \mathbf{v}^l$, where $\mathbf{v}^i$ and $\mathbf{v}^l$ correspond to a vector described with respect to the inertial and the local frames, respectively.

While in spherical coordinates the position of the airfoil is given by θ, ϕ, and r, in Cartesian coordinates it is described by

$$\mathbf{r}^i = r \begin{bmatrix} \sin\theta\cos\phi \\ \sin\theta\sin\phi \\ \cos\theta \end{bmatrix} \tag{4.2}$$

Assuming that the point of action of all forces coincides with the center of mass of the airfoil, the system dynamics can be analytically obtained by applying Newton's laws of motion to the kite in the local frame

$$m \begin{bmatrix} r\ddot{\theta} \\ r\ddot{\phi}\sin\theta \\ \ddot{r} \end{bmatrix} = \mathbf{F}_g^l + \mathbf{F}_{ap}^l + \mathbf{F}_a^l + \mathbf{F}_{a,t}^l + \mathbf{F}_t^l \tag{4.3}$$

where $\mathbf{F}_g$ is the gravity force due to the airfoil and to the tethers; $\mathbf{F}_{ap}^l$ is the the apparent force; $\mathbf{F}_a$ is the airfoil aerodynamic force; $\mathbf{F}_{d_t}^l$ is the aerodynamic drag force due to the tethers; and $\mathbf{F}_t^l$ is finally the traction force exerted by the lines on the kite.

Gravity force

As a result of the interaction of the masses in the system with Earth's gravitational field, a gravity force $\mathbf{F}_g$ can be observed. This model considers the masses of the airfoil and of the tethers, and models $\mathbf{F}_g$ as

$$\mathbf{F}_g^i = (m + \frac{n_t \rho_t \pi d_t^2 r}{4})\mathbf{g} \tag{4.4}$$

where ρ_t, d_t, and n_t are the tethers' density, diameter, and multiplicity, respectively, and $\mathbf{g}$ is the gravity vector. Note that $\mathbf{F}_g^l$ can be easily obtained by simply applying the transformation defined by $\mathcal{R}_l^i = (\mathcal{R}_i^l)^T$ to $\mathbf{F}_g^i$;

Apparent force

An apparent force $\mathbf{F}_{ap}$ comprising centrifugal and Coriolis effects appears as a result from the acceleration of a non-inertial frame of coordinates with respect to an inertial one. This force can be written in the local frame as

$$\mathbf{F}_{ap}^l = m \begin{bmatrix} \dot{\phi}^2 r \sin\theta\cos\theta - 2\dot{r}\dot{\theta} \\ -2\dot{r}\dot{\phi}\sin\theta - 2\dot{\phi}\dot{\theta} r\cos\theta \\ r\dot{\theta}^2 + r\dot{\phi}^2\sin\theta \end{bmatrix} \tag{4.5}$$

Aerodynamic force

The vector $\mathbf{F}_a$ denotes the aerodynamic force resulting from the interaction of the airfoil with the effective, or apparent wind $\mathbf{w}_a^i = \mathbf{w}_n^i - \dot{\mathbf{r}}^i$, which in the local frame can be written as

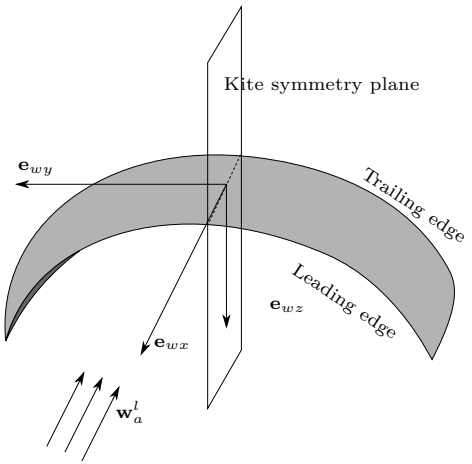

Figure 4.2: Wind reference frame
Source: Adapted from [19]

$$\mathbf{w}_a^l = (\mathcal{R}_i^l)^T \mathbf{w}_n^i - \begin{bmatrix} \dot{\theta} r \\ \dot{\phi} r \sin\theta \\ \dot{r} \end{bmatrix}^l \tag{4.6}$$

Consider now a wind coordinate system $(\mathbf{e}_{wx}, \mathbf{e}_{wy}, \mathbf{e}_{wz})$, whose center is located at the airfoil center of gravity. The $\mathbf{e}_{wx}$ vector is aligned with the effective wind speed vector, pointing from the trailing to the leading edge of the wing; the $\mathbf{e}_{wz}$ vector is contained in the kite symmetry plane, which is assumed to instantly align itself with the apparent wind, and points from the top surface of the kite to the bottom; and $\mathbf{e}_{wy}$ completes the right handed system, as depicted in Figure 4.2.

The unit vector $\mathbf{e}_{wx}$ can be expressed in the local coordinate system as

$$\mathbf{e}_{wx}^l = -\frac{\mathbf{w}_a^l}{\|\mathbf{w}_a^l\|} \tag{4.7}$$

while $\mathbf{e}_{wy}^l$ is given by

$$\mathbf{e}_{wy}^{l} = \mathbf{e}_w(-\cos(\psi)\sin(\eta)) + (\mathbf{e}_r \times \mathbf{e}_w)(\cos(\psi)\cos(\eta)) + \mathbf{e}_r \sin(\psi) \tag{4.8}$$

where

$$\mathbf{e}_w = -\frac{\mathbf{w}_a^l - \mathbf{e}_r(\mathbf{e}_r \cdot \mathbf{w}_a^l)}{\|\mathbf{w}_a^l - \mathbf{e}_r(\mathbf{e}_r \cdot \mathbf{w}_a^l)\|} \tag{4.9}$$

$$\eta = \arcsin\left(\frac{\mathbf{w_a^l} \cdot \mathbf{e}_r}{\|\mathbf{w}_a^l - \mathbf{e}_r(\mathbf{e}_r \cdot \mathbf{w}_a^l)\|}\tan(\psi)\right) \tag{4.10}$$

Finally, the unit vector $\mathbf{e}_{wz}^{l}$ can be computed as

$$\mathbf{e}_{wy}^{l} = \mathbf{e}_{wx}^{l} \times \mathbf{e}_{wy}^{l} \tag{4.11}$$

For all wing types in which steering is based on the difference in length of two command lines, pulling one tether while releasing the other will cause the wing to execute a turn in the same direction. However, the internal mechanisms through which the change in the flight trajectory is achieved can be different. Basically, a steering input causes a rigid wing to roll and a flexible kite to deform [37], yielding a similar change in its trajectory. In [19], the wing is assumed rigid, and its aerodynamic properties constant, which allows for determining the steering forces as functions of the roll angle ψ computed from the difference in length of the two command lines Δl, as can be seen in Figure 4.3, through the equation

$$\psi = \arcsin\frac{\Delta l}{l_w} \tag{4.12}$$

with d being the distance between the two lines fixing points at the kite. The angle ψ influences the airfoil motion by changing the direction of the aerodynamic force vector, which can be computed as a sum of drag and lift effects by

$$\mathbf{F}_a^l = -\frac{1}{2}C_d A\rho \left\|\mathbf{w}_a^l\right\|^2 \mathbf{e}_{wx} - \frac{1}{2}C_l A\rho \left\|\mathbf{w}_a^l\right\|^2 \mathbf{e}_{wz} \tag{4.13}$$

where ρ is the air density, A is the area of the airfoil, C_d and C_l are the airfoil drag and lift coefficients. These coefficients are function of the

angle-of-attack of the airfoil α, which is computed in this model by

$$\alpha = \alpha_0 + \Delta\alpha \tag{4.14}$$

with α_0 being the so called base, or static angle-of-attack, which is another control input to the model, and $\Delta\alpha$ being the dynamic angle-of-attack given by

$$\Delta\alpha = \arcsin\left(\frac{\mathbf{e}_r \cdot \mathbf{w}_a^l}{\|w\|_a^l}\right) \tag{4.15}$$

Tether drag force

The vector $\mathbf{F}_{dt}$ denotes the aerodynamic drag force due to the tethers, which acts against the movement of the airfoil. This force causes a torque given by $\mathbf{T}_d = r\mathbf{e}_r \times \mathbf{F}_{dt}^l$, which can be evaluated for the whole extension of the tether by the integral

$$\begin{aligned}\mathbf{T}_d &= \int_0^r (s\mathbf{e}_r \times -\frac{\rho C_{dt} d_t \cos(\Delta\alpha)}{2}(\frac{s}{r}\left\|\mathbf{w}_a^l\right\|)^2 \mathbf{e}_{wx})ds \\ &= r\mathbf{e}_r \times -\frac{\rho C_{dt} A_t \cos\Delta\alpha}{8}\left\|\mathbf{w}_a^l\right\|^2 \mathbf{e}_{wx}\end{aligned} \tag{4.16}$$

where ds corresponds to an infinitesimal segment of the tethers, C_{dt} is their drag coefficient, d_t the diameter, and $A_d\cos(\Delta\alpha) = rd_t\cos(\Delta\alpha)$ is their frontal area. The force $\mathbf{F}_{dt}^l$ can, therefore, can be expressed in local coordinates as

$$\mathbf{F}_{dt}^l = -\frac{\rho C_{dt} A_t \cos\Delta\alpha}{8}\left\|\mathbf{w}_a^l\right\|^2 \mathbf{e}_{wx} \tag{4.17}$$

Traction force

$\mathbf{F}_t$ is the traction force exerted by the lines on the kite, which due to the tether rigidity assumption is always directed along the local unit vector $\mathbf{e}_r$. Assuming that the tether reeling out speed is being controlled, the magnitude of the traction force can be computed from the equilibrium of forces in the direction of $\mathbf{e}_r$ according to the equation

$$\left\|\mathbf{F}_t^l\right\| = (\mathbf{F}_g^l + \mathbf{F}_{ap}^l + \mathbf{F}_a^l + \mathbf{F}_{dt}^l)\cdot\mathbf{e}_r - m\ddot{r} \tag{4.18}$$

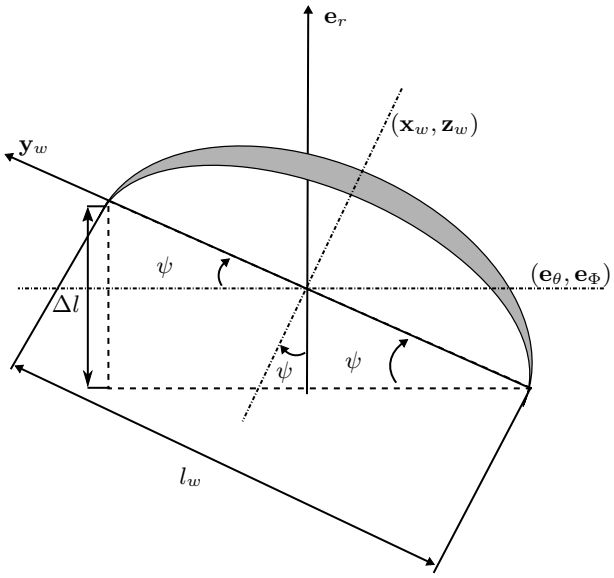

Figure 4.3: View of the airfoil leading edge and rolling mechanism
Source: Original

More recently, the work in [37] has proposed minor enhancements to the model just described, especially regarding the value of the equivalent point mass and, in [42], a similar approach was used to model a tethered airfoil with constant tether length. Besides the azimuth and elevation angles, this model also includes the dynamics of the yaw and pitch angles of the aircraft.

There are simpler modeling approaches that also make use of the single-point mass assumption. Although suitable for analysis, control, and estimation purposes, such models are rarely used for simulation. In [43, 44] a point mass approximation is used to represent the dynamics of a tethered airfoil on the plane tangent to its flight surface. The airfoil is assumed to be anchored to the ground by two cables, which are also used for steering, and flight dynamics is determined as a result of the gravity, apparent (inertial and Coriolis), aerodynamic and cable traction forces, evaluated in a local frame. The kite position $\mathbf{r}$ is described in spherical coordinates by the variables θ, ϕ, and r, where θ is the polar angle, ϕ is the azimuth angle, and r is the radial distance

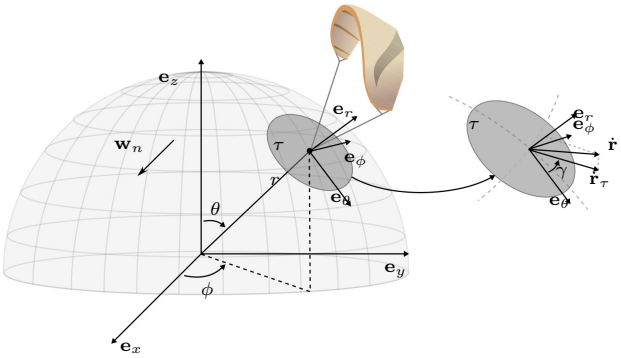

Figure 4.4: Wind window, tangent plane, and course angle
Source: Adapted from [45]

from the kite center of mass to the anchorage point on the ground. The airfoil speed vector is $\dot{\mathbf{r}}$, and its projection $\dot{\mathbf{r}}_\tau$ onto the tangent plane τ of the spherical flight surface at $\mathbf{r}$ described by the normal vector $\mathbf{e}_r$ is given by

$$\dot{\mathbf{r}}_\tau = r \begin{bmatrix} \dot{\theta} \\ \dot{\phi} \sin\theta \end{bmatrix} = r\sqrt{\dot{\theta}^2 + (\dot{\phi}\sin\theta)^2} \begin{bmatrix} \cos\gamma \\ \sin\gamma \end{bmatrix} \tag{4.19}$$

where $V = \sqrt{\dot{\theta}^2 + (\dot{\phi}\sin\theta)^2}$ is the magnitude of the kite angular speed, and γ is a variable referred to as course angle, which represents the direction of the velocity vector projected onto a plane tangent to the flight surface at the wing's current position. The course angle, whose geometrical interpretation is illustrated in Figure 4.4, can be computed as

$$\gamma = \arctan\left(\frac{\dot{\mathbf{r}}_\tau \cdot \mathbf{e}_\phi}{\dot{\mathbf{r}}_\tau \cdot \mathbf{e}_\theta}\right) = \arctan\left(\frac{\dot{\phi}\sin\theta}{\dot{\theta}}\right) \tag{4.20}$$

Considering the state vector $\mathbf{x} = [\theta, \dot{\theta}, \phi, \dot{\phi}]^T$, the model describes the dynamics of the point mass on the spherical surface by the following set of equations

$$\begin{bmatrix} \dot{\theta} \\ \ddot{\theta} \\ \dot{\phi} \\ \ddot{\phi} \end{bmatrix} = \begin{bmatrix} \dot{\theta} \\ \dot{V}\dot{\theta}V^{-1} - \dot{\gamma}\dot{\phi}\sin\theta \\ \dot{\phi} \\ \dot{V}\dot{\phi}V^{-1} + \dot{\gamma}\dot{\theta}(\sin\theta)^{-1} - \dot{\phi}\dot{\theta}\cos\theta(\sin\theta)^{-1} \end{bmatrix} \tag{4.21}$$

where $\dot{V}$ can be computed by simply differentiating V, according to the equation

$$\dot{V} = \frac{\dot{\theta}\ddot{\theta} + \dot{\phi}\ddot{\phi}(\sin\theta)^2 + 0.5\dot{\phi}^2\dot{\theta}\sin 2\theta}{V} \tag{4.22}$$

The accelerations $\ddot{\theta}$ and $\ddot{\phi}$ of the point mass are functions of the aerodynamic, gravity, and apparent forces defined earlier, and can be computed as

$$\begin{aligned} \ddot{\theta} &= \frac{(\mathbf{F}_a + \mathbf{F}_g + \mathbf{F}_{ap}) \cdot \mathbf{e}_\theta}{mr} \\ \ddot{\phi} &= \frac{(\mathbf{F}_a + \mathbf{F}_g + \mathbf{F}_{ap}) \cdot \mathbf{e}_\phi}{mr\sin\theta} \end{aligned} \tag{4.23}$$

4.1.2 Multi-particle models

According to [26], most AWE models are based on a minimal coordinates formulation, where the wing evolves on a sphere centered at the lower attachment point of the tether. This physical constraint is enforced through the usage of spherical coordinates for the equations of motion, and the wing orientation is often represented by means of Euler angles or quaternions. Even though the minimal representation is intuitive and simple to formulate, the resulting models have a series of drawbacks, including intricate symbolics, singularity points, and the need for elaborate nonlinear transformations especially for projecting the wing relative velocity into its reference frame. It has been observed in multi-body modeling that the model efficiency and simplicity can be significantly improved by considering each body separately and by linking them through algebraic constraints. Finally, [26] also presents a modeling approach for AWE systems that allows for developing models of low symbolic complexity and low nonlinearity. The approach is

based on multi-body modeling with the Lagrangian framework, and uses natural coordinates and algebraic constraints for representing the evolution of the system. The technique is demonstrated on a single-wing AWE prototype for power generation and rotating start-up, and also for a dual-wing AWE system. The single-wing model presented by the authors considers the tether as a rigid link of varying length L, whose acceleration $\ddot{L}$ is a control variable. For the sake of simplicity, it is assumed that the relative variation of the tether length is small, such that its mass can be considered constant.

Another subclass of multi-particle models, exemplified in [46], also utilizes a discretization of the tether as a multi body system, as illustrated in Figure 4.5. In this work, the Lagrangian framework is applied to derive in generalized coordinates the equations of motion of the airfoil, represented by a single point-mass, and of the tether, described as a collection of point masses connected by inelastic rods. A simple procedure is developed for efficiently determining the tension constraint forces acting on the tether elements, and the deployment and retrieval of the cable is implemented through the addition and subtraction of tether elements during simulation. Model validity and accuracy is discussed based on a series of numerical experiments. According to [47], the advantage of this approach is the direct incorporation of constraints which results in a compact problem formulation. However, the representation of the tether as a series of rigid segments connected by spherical joints is not sufficient for modeling the traction force and for implementing the control loop. Besides, the addition and removal of point masses during simulation can lead to artificial discontinuities in the model and make it difficult to implement the force controller.

The work in [47] proposes a modeling framework for the dynamic behavior of a ground generation AWE system in which the wing, the bridle, the airborne control unit, or control pod are all represented as sets of particles connected by means of spring-damper elements, as depicted in Figure 4.6. Within this framework, two kite models are proposed: a point mass model and a four point mass model. Reeling of the tether is modeled by varying the lengths of constituent tether elements (i.e. the links between particles), and the dynamical behavior of the ground station is also considered. An automatic control system used for the operation of an actual AWE prototype is used to

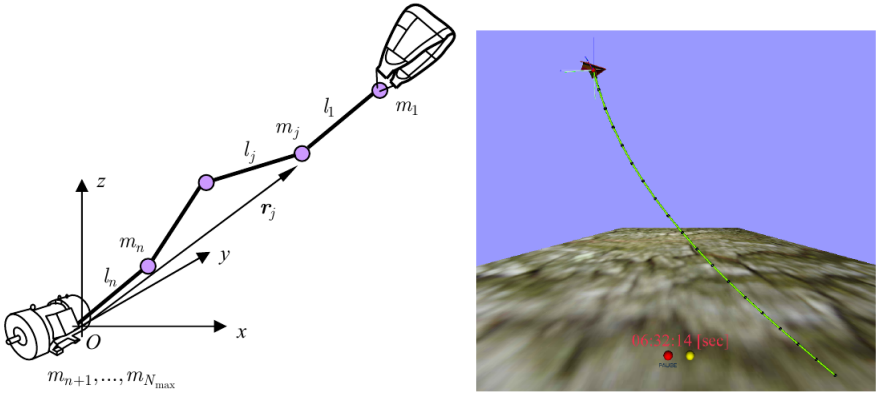

Conceptual model Simulation results with sag

Figure 4.5: Conceptual overview of an AWE system model with flexible tether
Source: [46]

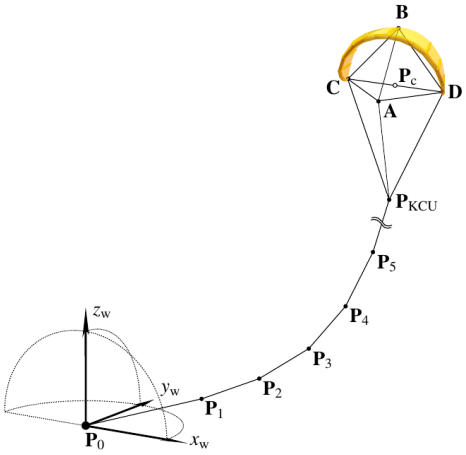

Figure 4.6: Diagram describing a multi-particle model with flexible tether and a four point mass airfoil
Source: [47]

validate the framework, and the simulation results show that the four point mass kite model can better predict the influence of gravity and inertia on the steering response, and remains stable even at low tether forces. Compared to simple one point models, the proposed framework has proven more accurate and robust, while still allowing soft real-time simulations of the complete system. One drawback of this approach is that it is fairly difficult to configure, and the stability of the simulation is directly dependent on the number of particles used and on their masses. According to the authors, the resulting simulator is soft real-time capable, and thus suitable for the training of kite pilots and winch operators, but can also be used for software-in-the-loop testing of AWE control systems, development of estimation algorithms, and the optimization of flight trajectories.

Based on the simulation results obtained with models such as those in [46] and [47], it becomes clear that the tether dynamics plays an important role in the behavior of AWE systems, and that considering it as a rigid segment might be a major source of inaccuracy, as can be inferred from the significant sag visible on Figure 4.5b. Moreover, this sag, which is usually neglected, might severely influence estimates of the airfoil position based on the line angles measured at the ground station, as will be discussed later in this chapter.

4.2 Control

In tower-based turbines, the ultimate goal of the control systems is to either maximize the energy production or limit it at a certain level, known as the rated power, when the wind becomes strong enough. If something goes wrong with the controllers, the rotor can simply be stalled and kept still, usually causing no harm to the plant and to its surrounding areas. In AWE systems, however, the situation is far more critical: even brief failures in the control systems may result in the aircraft colliding with the ground, and can lead to catastrophic results. In other words, the controllers, especially those related to flight, should not only yield trajectories that allow for the maximization of the energy production, but should also be robust enough to ensure a stable, safe flight in spite of challenging operating conditions such as wind gusts, rain, snow etc.

4.2.1 Centralized approaches

Early works in the literature regarding control of tethered wings during the active phase employed a centralized approach for jointly generating the flight trajectory and the control inputs for both the airborne and the ground units. In such cases, these inputs are obtained through an online optimization procedure executed within each sampling interval of the digital control system, usually by means of Nonlinear Model Predictive Control (NMPC) techniques [5, 19, 48, 49]. Although effective, these approaches have high computational requirements, and are centralized by nature, contrasting with most AWE scenarios which usually involve a set of physically separate components. Therefore, besides increasing complexity and costs with hardware, centralized optimization approaches raise the need of sending data back and fourth between the different units, which in turn can introduce delays and losses capable of seriously deteriorating the performance of the controllers, and might eventually lead to instability.

According to [19], NMPC is a powerful tool to deal with nonlinear, open loop unstable systems subject to operational constraints and with relatively fast dynamics. It is capable of stabilizing and controlling these systems while explicitly taking into account state and input constraints. The author points out, however, that an efficient implementation is needed, since the computation of the control input, which requires the real-time solution of a constrained optimization problem, can not be performed at the employed "fast" sampling rate. This issue motivates research efforts devoted to devise more efficient implementations of predictive controllers, as well as to find simpler, more lightweight alternatives.

4.2.2 Decentralized approaches

As the AWE community matured, and issues with optimization based control started to be reported by several different groups [50, 51], the trend has shifted towards a decentralized approach with physically separate structures for controlling the wing flight and the reeling of the tether. The resulting controllers can be installed in the aircraft and at the ground station, respectively, resulting in a topology in which each controller depends solely on variables that are locally available,

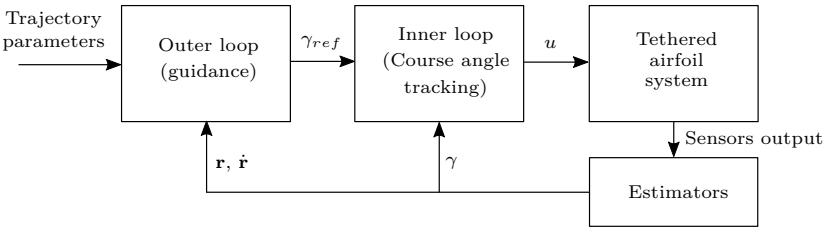

Figure 4.7: Decentralized control topology with two cascaded loops
Source: Original

therefore enhancing overall robustness against communication failures between the airborne and the ground systems and reducing the computational load in each unit [13, 18, 52].

In such decentralized strategies the flight controller usually consists of a two-loop cascaded structure similar to that of Figure 4.7, in which the wing trajectory is generated in the outer loop and tracked by the inner loop, most commonly by controlling the course angle, defined as the angular displacement of a projection of the wing velocity vector onto a plane tangent to the sphere to which the trajectory is constrained, as described in 4.1.1 and indicated in Figure 4.4. The actuation is then performed by manipulation of the steering inputs, whose components and operation can vary according to the constructive concept of the aircraft, as discussed in Section 3.1.1.

4.3 Optimization

More recently, attention has been paid not only to the control problem, but also to strategies for maximizing the power generated by AWE systems. In a ground-generation scenario, for instance, during the active phase the wing should fly on a path that yields the highest traction force for the given wind condition, whereas in the passive phase traction on the tether should be controlled to minimize the amount of energy consumed for reeling the tether back in and not to affect flight stability.

According to [18], most optimization approaches described in the literature involve the offline computation of an optimal path based on a non-linear point mass model considering very specific wind conditions. Automatic controllers are then designed to follow this optimal reference

trajectory. Such approaches, however, present a series of drawbacks. If uncertainties are present in the model, and they usually are, the process might lead to suboptimal or even infeasible trajectories. Finally, wind speed and direction at flight level are assumed to be known, which is hardly the case, given that the wind field changes significantly over time and space, and that its estimation based only on ground anemometer measurements is difficult.

Assuming all system parameters are completely known, and the model is accurate, controllers based on NMPC techniques, such as those presented in Section 4.2, should also yield inputs capable of maximizing the output power of an AWE system. This is achieved through the online optimization of arbitrary figures of merit, which can also weigh the control effort and incorporate operational constraints in their formulation. In practice, however, many parameters remain unknown, the model is inaccurate, and such approaches might too result in suboptimal, or infeasible trajectories. Because of the difficulty, low reliability, and computational cost associated with the real-time solution of the optimization problem, binding the generation of control inputs to it can be dangerous, and lead to poor results.

The recent trend towards more decentralized control structures, which do not worry about optimality, raise the need of implementing additional mechanisms for ensuring that the AWE systems will operate close to their full potential. Current approaches achieve this goal by manipulating the references tracked by the controllers, which are, in turn, generated by a higher level, possibly physically separate subsystem. Since the computation of control inputs no longer relies on any optimization, this architecture allows for this subsystem to execute on a much lower frequency and be incapable of affecting the performance of the controllers. In this direction, [18] proposed an algorithm that uses only the measured traction force on the tether and the wing's position, and is able to center the flight trajectory according to changes in the prevalent wind. The algorithm works in spite of the uncertain and time-varying wind conditions, and does not rely on any specific hardware. It does, however, rely on the knowledge of the aerodynamic efficiency of the airfoil, which depends on the constructive characteristics of the wing, and is substantially time-variant.

Another work concerned with optimization in a decentralized con-

trol paradigm is [19], which employs numerical optimization techniques to optimally choose the design and operational parameters of pumping-kite AWE systems. More specifically, the author presents optimal values for the reeling out/in speeds, elevation, and azimuth angles of the flight path during both the active and the passive phases, which turn out to be functions of the nominal wind at flight level.

In [37], an optimization problem is formulated and the operating parameters for the traction and retraction phases of a pumping-kite AWE system resulting from its solution are shown to yield the maximum cycle power. One of the main findings of the proposed approach is that, by reeling out at a lower speed than the value that maximizes the traction power, the duty cycle increases and, thereby, also the cycle power. The author points out, however, that there is still significant room for improvement regarding the proposed iterative optimization procedure. For instance, although it was conceived for any airfoil with given aerodynamic curves, it is hard to apply the method in the case of flexible wings because their aerodynamic characteristics may change depending on the wing loading, apparent wind speed, angle of attack and deformations induced by steering. Therefore it is suggested that future studies focus on the adaptation of the method for wings with unknown aerodynamic curves.

The work in [53] focuses on the design of the passive phase maneuver of an AWE system in a pumping-kite configuration. A robustness index against wind turbulence is proposed and analyzed, and an offline algorithm for generating a flight trajectory reference, which maximizes the cycle power while considering the desired robustness index, is presented. The proposed optimization depends on knowledge of the lift and drag coefficient curves, which in practice might be unknown, or contain significant errors. These errors might impact the intervals of critical angle-of-attack as well as the obtained trajectory. Also, in the presented method, the amount of admissible perturbation depends on how fast the response of the pitch actuator and of the ground motor are, as well as on the control dynamics, raising the need of determining the control gains and delays of the system. Finally, the study concludes that in order to test the dive maneuver in an actual prototype, an approach for measuring the effective wind and the angle-of-attack is necessary.

The on-line estimation of system parameters describing the aircraft state is of utmost importance for controlling the aircraft flight, as studied e.g. in [14]. As optimization approaches become more popular, addressing the problem of estimating aerodynamic parameters, the airfoil angle of attack and the wind also becomes necessary. Obtaining a relationship between the lift and drag coefficients and the angle-of-attack of the airfoil could too be helpful e.g. for implementing more complex, model based optimization setups to be used with flexible airfoils, whose aerodynamic characteristics are hardly known due to the lack of reliable procedures.

4.4 Measurement and filtering

A common point to all of the aforementioned investigations is that they rely on knowledge of system states and parameters that are a priori unknown or hard to measure, such as the position and velocity of the aircraft, the wind speed and direction at flight level, the aerodynamic characteristics of the system (i.e. its coefficients of lift and drag), or of parameters that depend on these quantities, for instance the steering gain in the turning rate law [13].

Generally speaking, AWE prototypes are equipped with instruments for measuring the position and velocity of the aircraft, the traction force on the tethers, and the wind conditions at a reference height. The most common devices employed for obtaining these variables are rotary encoders, load cells, and anemometers, respectively. A few prototypes, however, also employ Global Positioning System (GPS) receivers and Inertial Measurement Units (IMUs) for positioning – as will be further discussed in Section 6.2, barometers for indirectly measuring altitude, and pitot tubes or sometimes even onboard turbines for obtaining an estimate of the apparent wind the airborne components are subject to. All other information required by the control, monitoring, and optimization subsystems must be extracted from these available data, which is usually accomplished by estimation techniques such as the EKF, the UKF, the MHE, and others, as shown in Table 4.1, which summarizes the measurement and estimation solutions reported in the recent AWE literature. Note that although none of the publications summarized in the table reports the use of turbines on the aircraft

for measuring wind speed at flight level, this approach is employed by most AWE systems in an airborne-generation configuration. It is also function of the estimators to eliminate as much as possible the noise present in the acquired signals by averaging, combining different information, and in some cases considering knowledge of the system dynamics.

In [54] the sensor setup and the basic navigation algorithm used for the flight control of a commercial kite towing system are presented. Among the sensing devices on board the control pod are an IMU for measuring the turn rates and the accelerations of this unit, an impeller anemometer for measuring the velocity of the apparent wind it is subject to, a barometer for obtaining the barometric height, and a strain gauge for measuring the traction on the main tether. At the ground station, three rotary encoders, and an anemometer were employed for measuring the line angles and length, and the wind conditions, respectively. An yaw angle estimator was developed to compute the orientation of the control pod based on the measured turning rates and accelerations, and a wind referencing scheme was employed to adjust the estimated yaw based on the measured wind direction.

With the aim of making research in AWE accessible to a larger number of researchers, the work in [13] provides guidelines for the construction of a small-scale (i.e. 6, 9, and 12 m^2 flexible airfoils) prototype with ground actuation and no energy generation capabilities, but which can be realized at low costs and used with no restrictions for testing different aspects of the technology. In addition to the guidelines, the details of the design and costs of an actual experimental setup which has been successfully used to develop and test sensor fusion and automatic control solutions are provided. Regarding the measurement setup, the system comprises an IMU and a GPS mounted on the control pod, three load-cells (i.e. one for each tether as shown in Figure 3.5d), rotary encoders for measuring the azimuth and elevation angles, a ground compass, GPS, and anemometer. The sensors and control hardware accounted for almost half of the total cost of U$ 30,125.00, with the IMU alone being responsible for around U$ 4,500.00 of this value.

The same prototype presented in [13] was employed in [16] for the development and testing of three model-based sensor fusion approaches

Table 4.1: Summary of the measurement setups and estimation techniques reported in the AWE literature

	Position / Velocity / Orientation						**Traction**	**Wind**			
Ref.	**Encoders**	**GPS**	**IMU**	**Cameras**	**Barometer**	**Radios**	**Load cell**	**Anemometer**	**Pitot tube**	**LIDAR**	**Estimation**
[54]	x	x	x		x		x	x			–
[16],[13]	x	x	x		x		x	x			Cascaded EKF+KF
[55]	x	x	x				x	x		x	–
[15]	x	x	x				x			x	UKF
[56]				x			x				–
[57]			x	x							MHE
[58], [14]	x		x			x					MEKF
[42]							x				EKF/UKF
[17]	x		x					x			EKF/UKF/MHE
[59]	x						x	x			EKF
[45]	x						x				EKF
[60]	x						x				LS
[61]		x	x				x		x		–

targeted at AWE systems. All of these approaches exploit the structure of the considered kinematic model to separate the problem of estimating the wing orientation from that of estimating its position and velocity. The use of EKFs for estimating the absolute orientation of rigid bodies from gyroscope and magnetometer data is well studied in the literature, and most commercial IMUs, including the one employed in the paper, already have their own EKF for this purpose. Therefore, the authors were able to use the orientation estimated by the IMU together with the dynamical model of the system to obtain an estimate of the kite's acceleration in the inertial reference frame. This information then served as input to a linear Kalman filter responsible for tracking position and velocity, resulting in a cascaded estimation structure. In the first approach proposed, the filter was fed with GPS and barometer data only. In the second approach, GPS data was corrected in order to project the measured position onto a sphere of radius given by the tether length. Finally, in the third approach, only the line angle sensors were used to obtain the position measurements. All estimated variables are combined to compute an initial estimate of the course angle, whose filtered version is then obtained by means of a standard Luenberger observer. The study concludes that, under the conditions considered, techniques based on GPS are not suitable in practice for the purpose of feedback control in crosswind motion due to fast dynamics, slow update rates, and time-varying lag, and that fast position measurement devices such as the line angle sensor are essential to obtain high accuracy when the lines are relatively short.

The details about the construction of another AWE prototype are presented in [55]. The initial goal of such work was to build a fully functional and operational autonomous AWE system with minimal efforts in time and costs, comprising driver and inverter technology, battery storage, load resistor and a three-line winch built into a mobile platform and designed to operate with a peak power output of 54 kW and 30 kW nominal continuous power output. Besides the commonly employed sensing devices, tests were performed together with a LIDAR wind measurement system for acquiring measurements of the wind conditions at altitudes up to 200 m.

Prototypes using rigid wings are able to obtain measurements of the wind at flight level by attaching simple pitot tubes to the aircraft. This

is the case of the system described in [61], which also includes a GPS for positioning, an IMU for determining the attitude and the absolute velocity of the airfoil, and a load cell for measuring the tether traction.

Later on, the same prototype presented in [55] was employed in [15] to test a more complete filtering scheme, in which an UKF was used to combine data from sensors chosen to minimize cost and reliability issues, including rotary encoders and a load cell on the ground station, and a GPS receiver and an airspeed sensor attached to the wing. The proposed setup allowed for the joint estimation of the airfoil position, velocity and acceleration, its aerodynamic coefficients and the wind vector. In order to validate the filter, this latter variable was then compared to the measurements obtained with the LIDAR wind measurement system, showing a close correlation. This indicates that the filtering setup might be a viable option for reliable wind site evaluation. Despite delivering a handful of important parameters, the filter structure remained elegant, extensible, and seems to be applicable to most AWE setups. Unfortunately, not all information on the filtering strategy could be found in order to reproduce the results.

In [60], a prototype consisting of a two line kite with ground actuation and rotary encoders for measuring the line angles was used in experiments in which the steering gain and transport delay were identified online during flight through a least squares fit, but the aerodynamic coefficients remained unknown. In the reference, the length of the considered data history and the frequency of the re-identification steps are tuning parameters of the adaptation approach.

The work presented in [56] developed hardware and software to track the flight of tethered vehicles, including kite-like AWE generation systems. The control system consists of a pan-tilt platform and a visible- spectrum digital camera, combined with tracking control software running on a standard PC. The prototype on which the system was tested has available two load-cells – one for each tether – and an anemometer. Regarding actuation, the same two electric motors used for generating electricity are also responsible for steering the aircraft. The system controls the flight of the vehicle to keep its position on a power-producing trajectory, maximizing velocity. The developed system enables effective operation of ground- and airborne-generation AWE systems, and was tested with a small-scale prototype and pre-

beta software. There is no information regarding any data fusion or estimation algorithm related to this specific prototype.

The work in [17] aims at designing and evaluating several estimators suitable for the estimation of the aircraft's position and attitude, as well as of the wind conditions at flight level. The implemented algorithms are the EKF, the UKF and a MHE. While EKF and UKF are recursive algorithms of the same structure, MHE explicitly takes into account the most recent measurements, trying to find the maximum likelihood trajectory for this time horizon by solving an optimization problem at every time step. The utilized sensors are an IMU, an anemometer for measuring the kite air path speed in flight direction, angular sensors for measuring the tether angles at the ground and a rotary encoder returning the winching speed and length of the tether. All approaches also try to estimate the bias of the turn rate sensor as well as wind speed and direction at flight level. After a series of simulations, the estimators were tested with real flight data, and seemed to perform well, although there is no ground truth for comparison.

In [57], a MHE is employed for estimating the position and orientation of tethered wings based on absolute pose measurements captured by a marker based stereo vision system. These measurements are fused with the angular velocities and accelerations obtained by an IMU mounted on the aircraft. The proposed algorithm is a modified version of the conventional MHE which approximates IMU measurements with polynomials to reduce the number of decision variables in the optimization problem, and which uses a Huber penalty function rather than the l_2-norm, and is shown to outperform it as well as the extended Kalman filter.

The work in [58], which also led to the publication in [14], presents estimation approaches for autonomous tethered kite systems for the purpose of airborne wind energy generation based on the fusion of measurements such as line angles and length, ranges obtained with radio-frequency radio devices, and inertial readings from IMU through a multiplicative Kalman filter, a technique used to compute estimates of nonlinear systems with continuous-time process dynamics and discrete-time measurements. The proposed filter is evaluated on simulated models, and shows a promising potential of the ranging devices to improve the quality of the position estimates. Finally, an automatic calibration

of the radio-frequency reference anchors is presented which reduces the setup time of the system, and makes its deployment more convenient.

In [42] spherical coordinates were used to model and to design state estimators for a tethered wing. The system was shown to remain observable even after the inclusion of wind dynamics in the model, and simulation results indicated that the UKF surpassed the EKF in performance. Regarding the sensor setup, the authors employed data from ground based devices such as rotary encoders for measuring line angles and their rates of change, anemometer for measuring the wind conditions, and a third encoder used for measuring the difference in length between the command lines, which modify the configuration of two flaps on the aircraft. The actuation takes place on the ground by means of a control input corresponding to the angular velocity of the flaps controlled by the power cables.

In [45] the line angles and their rates of changes, together with tether traction measurements from a load cell, are used to feed an EKF and estimate the parameters of a simplified model of the dynamical behavior of the course angle. These parameters, namely the delay existing between the control action and the resulting change in direction of the airfoil, as well as of a steering control gain are then used to adaptively adjust a proportional controller. The proposed filtering and control scheme are validated based on a hardware-in-the-loop setup and evaluated on a field test involving a small scale prototype.

Finally, in [59], a filtering and estimation strategy using an EKF and inspired in [15] was presented. As a major difference from the previous works, this new approach proposes the introduction of an orthogonality constraint between the lift force and the apparent wind vectors as an observation with a very high degree of certainty. Among the estimated states were the wind and the lift force vectors, and the magnitude of the equivalent drag force. The filter performance was validated in a simulation environment using the dynamic point-mass kite model [19], and experimental results with the same prototype used in [45] were also discussed.

Regarding the aerodynamic characteristics, for rigid wings these curves are usually computed through wind tunnel tests, but when it comes to flexible wings (i.e. fabric-made kites), these tests can become more cumbersome and resource-demanding. Furthermore, even

if the aerodynamic characteristics are known a priori, they may change significantly during operation depending, for instance, on the current environmental conditions (rain, snow, air humidity) or due to accumulated material wear – such as the increase in kite fabric porosity caused by long-term exposition to solar radiation and the increase in tether roughness due to friction with pulleys and housing components. Hence, if one could monitor how the aerodynamic coefficients degrade with time, they could better decide on when to stop the AWE system operation to carry out maintenance on the wing and/or tether. Perhaps more importantly, because the flight controllers are often designed based on a dynamic model whose parameter values are assumed to be known, depending on how much these assumed values change during operation, the control performance may degrade up to a point where flight stability is threatened. Based on these observations, we can conclude that not only the development of adequate models is important in the field of AWE technology, but also the continuous update of such models in order to maintain their accuracy.

4.4.1 Positioning

Among the challenges related to measurement and filtering in the field of AWE, the determination of the aircraft's position and velocity in 3D space is one that deserves special attention, given the importance of these variables for flight control and operational optimization. Even though accuracy in their estimation is crucial for ensuring operational robustness, as seen in the previous sections, current positioning solutions applied by the AWE community are only partially successful, and fail to address several issues that are known to arise in actual operational conditions.

Because of its simplicity, the usual approach for determining the position and velocity of the aircraft is to combine measurements of the tether angles and length, as well as their rates of change obtained by a line following mechanism attached to rotary encoders at the ground station, as presented in [13, 16, 54, 55] and depicted in Figure 4.8. In pumping-kite configurations, estimators utilizing these measurements have been proven reasonably effective when the tethers are kept taut by high aerodynamic forces on the kite, which typically occurs during the reel-out phase. However, during the reel-in phase, when the

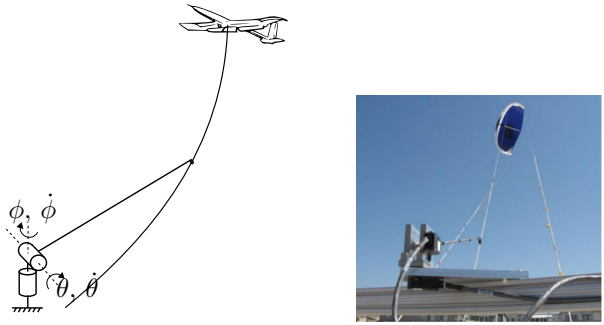

Conceptual overview Physical realization

Figure 4.8: Line angle measurement setup with rotary encoders at the ground station

Source: Adapted from [13]

traction force must be kept low, estimation results based on the assumption of taut tethers degrade. According to [14], besides being susceptible to degradation due to tether dynamics, estimates produced by such schemes also introduce significant delay, which impacts negatively on the performance of the automatic flight controllers. Airborne-generation systems might experience the same problem if the maintenance of a minimum traction on the tether is not always guaranteed.

Other popular strategies, such as that described in [16], make use of a standalone GPS or a GPS associated with an IMU and a barometer. However, GPS signal loss has been reported in situations in which the aircraft is subject to high accelerations or flying at low altitudes [62]. Furthermore, signal quality can vary depending on meteorological conditions and location, which makes it not reliable enough for AWE applications. According to [16], GPS is affected by poor accuracy and by a time-varying delay which, under the considered conditions, causes it not to be suitable for control applications. Finally, industrial grade GPS receivers and IMUs compatible with the AWE requirements can be very expensive, costing up to several thousand dollars, according to the bill of materials presented for the small scale prototype developed in [13].

Another investigated alternative reported in [56, 57, 63], has been the use of cameras and computer vision techniques for determining the position and velocity of the aircraft, in setups similar to those

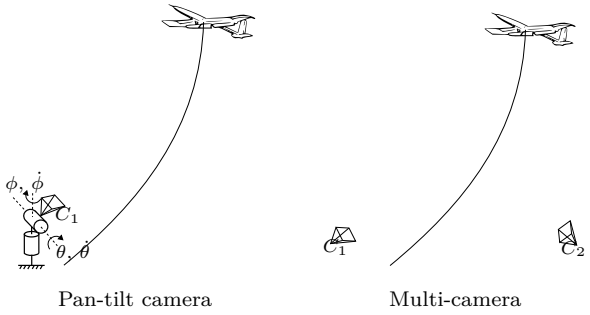

Figure 4.9: Camera setups for estimation of the aircraft's position and velocity

Source: Original

illustrated in Figure 4.9. The approach described in [56] is to employ a pan-tilt camera to track the aircraft from the ground and, based on the resulting angular displacement of the mechanism onto which it is mounted, determine the coordinates of the target. Even if the camera is fixed, as long as the characteristics of its lens are known in advance (e.g. from calibration), the position of the aircraft can be determined as in [63] from the displacement of its projection computed with respect to the center of the image frame. An alternative approach is to deploy a series of cameras around the ground station. Assuming that it simultaneously appears in the images captured by at least two of them, and that the cameras were properly calibrated, the position of the aircraft can be fully reconstructed. While these strategies solve the issues caused by tether sag, they raise several other difficulties, and do not seem to address real-world situations such as changes in lighting and weather, occlusion, and the presence of extraneous objects in the images. Therefore, they are not suitable for a system which is expected to work uninterruptedly and, to some extent, be independent of environmental conditions. Given their superior accuracy, however, computer vision techniques can be employed to generate ground truth data for assessing the quality of other positioning setups, as proposed in [63].

More recently, an approach combining range measurements from Ultra-wideband (UWB) devices and readings from an IMU was proposed in [14]. In this approach, ranges corresponding to the distances

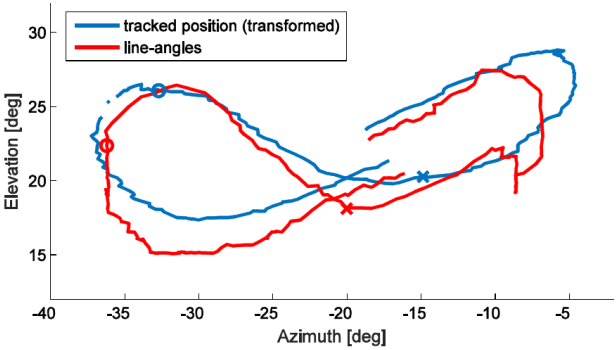

Figure 4.10: Flight trajectories estimated with line angles and with a visual tracking technique

Source: [63]

between a radio transceiver fixed to the aircraft and a number of beacons scattered on the ground are measured, and combined with data from an IMU through a multiplicative EKF. Although simulations show a larger accuracy of this setup when compared to encoder-based schemes, specially when the tethers are not highly taut, no experimental results validating this setup are available in the literature.

Radio-based localization is a well studied topic, and there are several methods for accomplishing its ultimate goal which is to determine the position of a mobile target based on the information carried by radio signals, as discussed in Section 2.5. The concept has successfully been applied to mobile robotics, as exemplified in [64], which describes a simple positioning setup comprising radio tags and an EKF capable of yielding results significantly better than those output by dead reckoning only.

According to [31], the difficulty in achieving highly precise location estimates has led a number of investigators to utilize parameter estimation techniques for positioning and tracking mobile targets. These techniques can be very beneficial, for example, in smoothing position tracks. In this context, Kalman, Bayesian, or particle filters are widely used as state estimators. These methods can be applied with a variety of sensor technologies and positioning algorithms to improve positioning and tracking performance in many real-world environments.

CHAPTER 5

Design of the estimation strategy

From Chapter 4, it is possible to conclude that, to this day, there are still no all encompassing, unquestionable solutions for the estimation problem in AWE. The field suffers with the lack of reliable approaches for determining the position and velocity of the aircraft, which are highly affected by tether sag, for measuring the wind conditions at high altitudes, and also for identifying the aerodynamic characteristics of the system. In order to fill this gap, this thesis presents a solution specifically targeted at AWE applications and capable of estimating these and other variables based on a minimal set of observations, paving the way for the implementation of more sophisticated control, power optimization, and fault detection strategies in the future. The proposed solution is designed as two separate estimation blocks, one for tracking the aircraft kinematic variables and the other for estimating the wind conditions it is subject to, as well as the resulting aerodynamic forces, which in turn can be used to compute its coefficients of lift and drag. Two different versions are presented for the first block: a multi range lateration based on the gradient descent algorithm; and a nonlinear Kalman filter which incorporates knowledge about the system dynamics. The second block, on the other hand, is designed as a nonlinear

Kalman filter whose performance is improved by means of a simple constraint enforcement technique. The resulting system is adaptable to different AWE concepts and can be easily extended to accommodate new sources of data. Moreover, it can be deployed in a decentralized topology, leading to reduced transport delays, and to the optimization of available resources.

This chapter presents in detail the so called kinematics and the aerodynamics estimation modules, focusing on the motivations behind each design decision taken during their development process. Based on the content presented hereafter, the reader is expected to be able to understand the results shown in the next chapter, and judge their suitability for application in AWE systems.

5.1 Filtering topology

For the purpose of favoring the development process and managing system complexity more efficiently, a decomposition of the final solution into two major functional blocks, or modules was proposed. The resulting components, namely the aerodynamics estimation module, and the kinematics estimation module, were organized in such a way that they could be designed, built, and tested independently, and later seamlessly integrated with a minimum amount of effort, yielding the structure shown in Figure 5.1. This approach later proven very effective, and ended up resulting in a more scalable and flexible solution.

Within the proposed topology, the kinematics estimation module is responsible for tracking the position and velocity of the aircraft, whereas the aerodynamics estimation module is assigned with the task of obtaining accurate estimates of the aerodynamic lift and drag forces the system is subject to, as well as of the wind speed and velocity at flight level. The aerodynamic lift and drag coefficients, as well as the dynamic angle-of-attack of the aircraft can be both computed directly from the estimated states through a closed form expression.

If necessary, outputs of one module can be fed as inputs to the other, e.g. to abstract away the origin of position and velocity data, a possibility that will be explored later in this chapter. This is an interesting feature, since even though most AWE systems have means of measuring position and velocity, how they obtain these information can vary

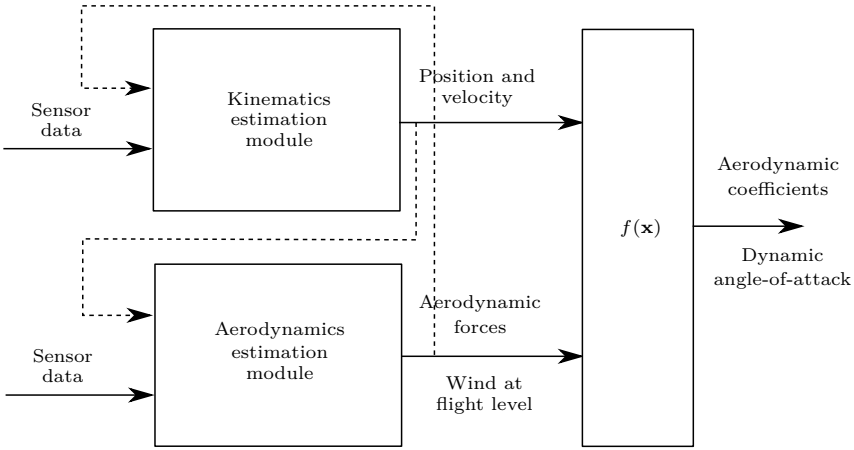

Figure 5.1: High-level topology of the proposed estimation structure
Source: Original

significantly. Rotary encoders, GPS receivers, IMUs, cameras, and radio devices can all be used as measurement sources, as seen in Section 4.4. In order for the outcome of this thesis to have a broader range of applicability, and be compatible with the largest possible number of prototypes, it must leave enough room for customization. By designing the system as two loosely coupled modules, the process of adapting it to a more specific scenario is smoothened. For instance, depending on the quality of the already existing measurement setup, and on the availability of computational resources, developers of AWE prototypes may choose whether or not both components should be deployed. Moreover, as will become clear later in the text, including additional measurements and replacing the dynamical model is much easier and safer with a modular structure.

Another interesting advantage of splitting the system is that it allows for supporting physically distributed deployment, which can be very appealing within the AWE context. Since the variables output by the kinematics estimation module are especially important for flight control purposes, this component can be lodged on the embedded platform of the aircraft, where, assuming a decentralized control topology, is where the flight controllers are usually installed. This eliminates most of the transport delay between the estimator and the controller,

increasing the overall robustness of the automatic flight control system. The aerodynamics estimation module, on the other hand, can be deployed on the ground station, next to the monitoring and power optimization structures, which will likely rely on its outputs. Besides saving computational resources on the aircraft, which are scarcer than those available in the embedded systems on the ground, this allows for each module to operate with an independent sample frequency compatible with its purpose, and also mitigates the possibility of propagating failures.

5.2 Dynamics modeling

The Kalman Filter framework provides a mechanism for using available knowledge about the behavior of a dynamical system for improving accuracy when estimating its states, as discussed in Section 2.4.2. In order to harness this power, however, one must be able to reasonably model the evolution of such system in time. This section presents a simple dynamic model of a generic AWE system which will be later employed in the modules of the estimation solution proposed in this chapter.

As discussed in Section 4.1, although common, models which constraint the flight surface to a sphere centered at the lower attachment point of the tether by using spherical coordinates have a series of drawbacks, including intricate symbolics, singularity points, and the need for elaborate nonlinear transformations. In order to avoid these issues, and to keep complexity and nonlinearity to a minimum, a procedure similar to that suggested in [26] is adopted, and the system is modeled as a series of bodies linked through algebraic constraints incorporated into the equations of motion through the Lagrangian framework. This results in a simple, easily extensible model, which is extremely convenient in a Kalman filtering scenario.

An AWE system, in either ground or airborne generation mode, can be generically described as a suspended aerodynamic structure anchored to the ground by one or more tethers, and exposed to a wind vector $\mathbf{w}_n$ with components in $\mathbf{x}_0$ and $\mathbf{y}_0$ only. Aiming at a good compromise between simplicity and accuracy, this suspended structure can then be modeled as two-point masses, or particles, m and m_t. The first

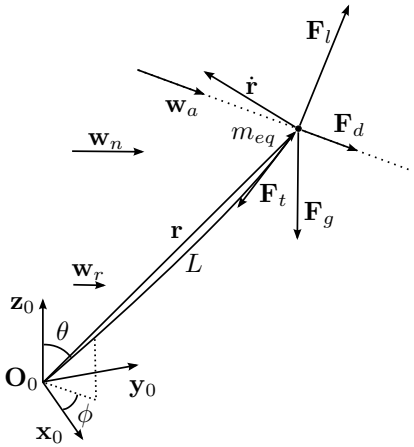

Figure 5.2: AWE system represented by an equivalent point-mass subject to different forces

Source: Original

particle represents the aircraft and the control pod, and is located at the aerodynamic center of the aircraft. The other particle lies midway between the origin and m, and represents the n_t perfectly taut tethers connecting the airfoil to the ground station. Its value is approximated by

$$m_t = (1/4)\, n_t\, \pi\, d_t^2\, L\, \mu_t \tag{5.1}$$

where μ_t, L, and d_t correspond to the volumetric density of the tethers, their length, and diameter, respectively. Besides the weight $\mathbf{F}_{g_t}$, the tether is also subject to an aerodynamic drag force $\mathbf{F}_{d_t}$. In order to assemble the equations of motion, these two forces will be translated to the aircraft point-mass position, yielding an equivalent particle of mass m_{eq}.

The system potential energy can be defined as $V(\mathbf{q}, \dot{\mathbf{q}})$, and its kinetic energy as $T(\mathbf{q}, \dot{\mathbf{q}})$, where $\mathbf{q} = (q_1, q_2, ..., q_m)$ are the *generalized coordinates*. Considering $\mathbf{q} = \mathbf{r} = [r_x, r_y, r_z]^T$, which is the position of the kite point-mass m, and knowing that the tether point-mass m_t is located at $(1/2)\,\mathbf{r}$, the expressions of the system's potential and kinetic

energy are, respectively,

$$\begin{aligned} V(\mathbf{r}) &= \left(m + \frac{1}{2}m_t\right) g\, r_z \\ T(\mathbf{r}, \dot{\mathbf{r}}) &= \frac{1}{2}\left(m + \frac{1}{4}m_t\right) \dot{\mathbf{r}}^T \dot{\mathbf{r}} \end{aligned} \tag{5.2}$$

where g is the acceleration of gravity, and $\dot{\mathbf{r}}$ is the wing velocity with respect to the reference frame. Based on the equations for the kinetic and potential energy, the system Lagrangian can be written as

$$\mathcal{L}(\mathbf{r}, \dot{\mathbf{r}}, \nu) = T(\mathbf{r}, \dot{\mathbf{r}}) - V(\mathbf{r}) - \nu^T \mathbf{c}(\mathbf{r})\,, \tag{5.3}$$

where ν is a vector of *Lagrange multipliers*, in which each entry corresponds to a constraint in the vector of constraints $\mathbf{c}(\mathbf{r})$. In this specific case, the only constraint is that the distance from the kite to the ground station is limited by the tether length L, assuming perfectly taut tethers. As discussed in [26], in a general scenario with variable tether length, the constraint and its time-derivatives can be expressed as

$$\begin{aligned} c(\mathbf{r}) &= \frac{1}{2}\left(\mathbf{r}^T\mathbf{r} - L^2\right) = 0 \\ \dot{c}(\mathbf{r}, \dot{\mathbf{r}}) &= \mathbf{r}^T\dot{\mathbf{r}} - L\,\dot{L} = 0 \\ \ddot{c}(\mathbf{r}, \dot{\mathbf{r}}, \ddot{\mathbf{r}}) &= \mathbf{r}^T\ddot{\mathbf{r}} + \dot{\mathbf{r}}^T\dot{\mathbf{r}} - L\,\ddot{L} - \dot{L}^2 = 0\,. \end{aligned} \tag{5.4}$$

Denoting the sum of all external forces acting upon the system by $\sum \mathbf{F}_{ext}$, and assuming that the aircraft's center of mass coincides with its aerodynamic center, and therefore that all forces it is subject to act upon m, the equations of motion can be obtained by substitution of (5.3) into the Euler-Lagrange equations

$$\frac{\partial \mathcal{L}(\mathbf{r}, \dot{\mathbf{r}})}{\partial r_i} - \frac{d}{dt}\frac{\partial \mathcal{L}(\mathbf{r}, \dot{\mathbf{r}})}{\partial \dot{r}_i} + \sum \mathbf{F}_{ext} = 0\,, \tag{5.5}$$

evaluated for each i-th coordinate of $\mathbf{r}$. Considering also the constraint equations in (5.4), the following set of dynamic equations is obtained:

$$\underbrace{\begin{bmatrix} (m+\frac{1}{4}m_t)\mathbf{I}_3 & \mathbf{r} \\ \mathbf{r}^T & 0 \end{bmatrix}}_{\mathbf{M}} \begin{bmatrix} \ddot{\mathbf{r}} \\ \nu \end{bmatrix} = \begin{bmatrix} \sum \mathbf{F}_{ext} + \left(m+\frac{1}{2}m_t\right)\mathbf{g} \\ -\dot{\mathbf{r}}^T\dot{\mathbf{r}} + \dot{L}^2 + L\ddot{L} \end{bmatrix}, \tag{5.6}$$

where $\mathbf{I}_3$ is the identity matrix of size 3, $\mathbf{g} = [0, 0, -g]^T$ is the vector of gravitational acceleration, and $m + \frac{1}{4}m_t$ can be interpreted as an equivalent point-mass m_{eq} comprising the aircraft, the control pod, and the tethers, and located at the system's aerodynamic center, as depicted in Figure 5.2. Given the system parameters m, m_t, and g, the sum of external forces $\sum \mathbf{F}_{ext}$, and the possibly controlled inputs of tether length L, reel-out speed $\dot{L}$, and acceleration $\ddot{L}$, the solution vector $[\ddot{\mathbf{r}}, \nu]^T$ can be computed as long as $\mathbf{M}$ is invertible.

Observe that the quantities in both sides of (5.6) are forces. As pointed out in [26], since ν is the constraint on the wing flight due to the tether, the product $\mathbf{r}\,\nu$ should correspond to the force that arises from this constraint, i.e. the *tether traction force* $\mathbf{F}_t$. The effect of the apparent forces are implicitly considered in the model through the second line of (5.6). On the other hand, by inspection, the weight vector is analytically obtained as

$$\mathbf{F}_g = \left(m + \frac{1}{2}m_t\right)\mathbf{g} \tag{5.7}$$

This force need not be explicitly considered in the model, since it has already been accounted for in the potential energy expression in Equation 5.2

The aerodynamic characteristics of the airfoil, together with its velocity relative to the wind, cause an aerodynamic lift force $\mathbf{F}_l$ to arise. This force is always perpendicular to the apparent wind, defined as $\mathbf{w}_a = \mathbf{w}_n - \dot{\mathbf{r}}$. Its instantaneous direction, however, is a priori unknown, being described by the unit vector $\mathbf{z}_l$. The aircraft itself, as well as other non-ideal elements in the system may also contribute to the appearance of aerodynamic drag forces. As opposed to what happens to the lift force, the direction and orientation of the drag forces depend only on the apparent wind $\mathbf{w}_a$. The effects of all individual elements subject to drag are combined into a single equivalent drag force $\mathbf{F}_d$, whose direction and orientation coincide with those of the apparent

wind.

Flight actuation takes place by means of the control vector $\mathbf{u} = [u_s, u_p]^T$, which comprises a steering and a pitch/de-power command, u_s and u_p, respectively. Regardless of the specific type of wing, as a general rule, the steering input causes the lift force to rotate around the apparent wind with an angular velocity ω_l, given by

$$\omega_l = c_{us} u_s \tag{5.8}$$

where c_{us} is an unknown gain associated with the steering command. As for the second input, it either directly changes the angle of attack by *pitching* the aircraft or it alters the airfoil shape and the corresponding curves of the lift and drag coefficients, C_l and C_d, respectively. In both cases, the input u_p causes the magnitude of the aerodynamic forces, defined as

$$\begin{aligned} \mathbf{F}_l &= (1/2)\,\rho\, A\, C_l\, w_a^2\, \mathbf{z}_l \\ \mathbf{F}_d &= (1/2)\,\rho\, A\, C_d\, w_a^2\, (\mathbf{w}_a / w_a)\,, \end{aligned} \tag{5.9}$$

to change.

When compared to the dynamic equations employed in [59], the model presented in this section is significantly more accurate, since it also accounts for the tether constraint and for the apparent forces, and therefore more accurate filtering results are expected.

5.3 Aerodynamics estimation module

Because of the nonlinear characteristics of the system, and in order to facilitate implementation in software, a discrete-time nonlinear EKF was chosen as the core structure for the aerodynamics estimation module. This is a common approach in the AWE literature, being used e.g. in [14, 16, 22, 42, 59]. As already discussed in Section 2.4.2, the Kalman filter combines knowledge about the dynamics of the system with control inputs and information gathered from measurement devices to improve estimation accuracy when compared to that obtained using measurements alone.

The design of a Kalman filter involves the definition of a set of state variables, which are believed to reasonably represent the system, and a dynamic model used to propagate these variables in time during

the prediction phase. Moreover, it must also include the definition of an observation vector, in which each entry corresponds to a quantity whose value is available with some degree of accuracy either from a measurement or from previous knowledge about the system, and is somehow related to the state variables through a so called observation model.

In the case of the proposed aerodynamics estimator, the system state vector $\mathbf{x}$ contains the position $\mathbf{r}$, the velocity $\dot{\mathbf{r}}$, and the acceleration $\ddot{\mathbf{r}}$ of the equivalent point-mass. These states are followed by the Lagrange multiplier ν associated to the tether constraint, the nominal wind $\mathbf{w}_n$, the lift force $\mathbf{F}_l$, the magnitude of the equivalent drag force F_d, and by the scalar gain c_u describing a linear relation between the steering command and the angular rate at which $\mathbf{F}_l$ rotates around the apparent wind as a result of this input, resulting in:

$$\mathbf{x} = [\mathbf{r}^T, \dot{\mathbf{r}}^T, \ddot{\mathbf{r}}^T, \nu, \mathbf{w}_n^T, \mathbf{F}_l^T, F_d, c_u]^T \,. \tag{5.10}$$

This specific choice of state variables is enough for capturing aspects of interest about the system while keeping the state vector's dimensionality to a minimum, and will later allow for the direct computation of other important quantities such as the aerodynamic efficiency and the complementary angle-of-attack of the aircraft.

When compared to other models employed for filtering purposes in the literature, the model presented in this thesis is somewhat more high-level. It directly considers in its formulation the aerodynamic forces, as opposed to the usual lift and drag coefficients. One advantage that follows from this approach is that the forces assumed to act upon the system are completely known, both in magnitude and direction. Another aspect worth mentioning is that by including the aerodynamic forces in the state vector one is able to model the effects of the control inputs in their magnitudes and direction, which would be harder if we had considered the aerodynamic coefficients instead.

The evolution of the states of the filter is ruled by the flight dynamics discussed in Section 5.2, which in turn can be described in discrete time by the set of difference equations

$$
\begin{aligned}
\mathbf{r}_{k+1} &= \mathbf{r}_k + \dot{\mathbf{r}}_k T_s \\
\dot{\mathbf{r}}_{k+1} &= \dot{\mathbf{r}}_k + \ddot{\mathbf{r}}_k T_s \\
\begin{bmatrix} \ddot{\mathbf{r}}_{k+1} \\ \nu_{k+1} \end{bmatrix} &= \begin{bmatrix} m_{eq}\mathbf{I}_3 & \mathbf{r}_k \\ \mathbf{r}_k^T & 0 \end{bmatrix}^{-1} \begin{bmatrix} \mathbf{F}_{lk} + \mathbf{F}_{dk} + \left(m + \frac{1}{2}m_t\right)\mathbf{g} \\ -\dot{\mathbf{r}}_k^T \dot{\mathbf{r}}_k + \dot{L}^2 + L\ddot{L} \end{bmatrix} \\
\mathbf{w}_{n\,k+1} &= \mathbf{w}_{n\,k} \\
\mathbf{F}_{l\,k+1} &= \mathcal{R}\left(\mathbf{F}_{l\,k}, \mathbf{w}_{a\,k}, c_{u\,k}\, u_k\, T_s\right) \\
F_{d\,k+1} &= F_{d\,k} \\
c_{u\,k+1} &= c_{u\,k}\,,
\end{aligned}
\tag{5.11}
$$

where $\mathcal{R}(\mathbf{u}, \mathbf{v}, \psi)$ is a function representing the counterclockwise rotation of $\mathbf{u}$ around $\mathbf{v}$ by an angle ψ, and is computed by the Euler-Rodrigues formula

$$
\mathcal{R}(\mathbf{u}, \mathbf{v}, \psi) = \begin{bmatrix} a^2 + b^2 - c^2 - d^2 & 2(bc + ad) & 2(bd - ac) \\ 2(bc - ad) & a^2 + c^2 - b^2 - d^2 & 2(cd + ab) \\ 2(bd + ac) & 2(cd - ab) & a^2 + d^2 - b^2 - c^2 \end{bmatrix}
\tag{5.12}
$$

where $\mathbf{v}$ is an arbitrary unit vector, and

$$
\begin{bmatrix} a & b & c & d \end{bmatrix} = \begin{bmatrix} \cos(\frac{\psi}{2}) & -\mathbf{v}\sin(\frac{\psi}{2}) \end{bmatrix}\,.
\tag{5.13}
$$

Note that although the dynamic model embedded in the filter relies on $\mathbf{F}_d$ for computing the predicted state, this variable is not present within the state vector itself. However, knowing that the drag force points to the same direction of the apparent wind $\mathbf{w}_a$, it can be easily obtained from F_d, which represents the magnitude of the equivalent drag force due to the airfoil, the control pod, and the tethers through the equation

$$
\mathbf{F}_d = F_d \frac{\mathbf{w}_a}{\|\mathbf{w}_a\|}\,.
\tag{5.14}
$$

Independently of their design, in most AWE systems a minimal set of variables is measured. The list includes the aircraft position $\mathbf{r}$ and

velocity $\dot{\mathbf{r}}$ with respect to the ground station, which can be obtained from rotary encoders measuring the tether angles and their rates of change, GPS receivers attached to the wing or to the control pod, radio frequency ranging devices, or even from vision-based tracking systems. Other easily obtainable data include the magnitude F_t of the traction force on the main tether, usually measured with a load cell [1], and the wind speed w_r and direction ϕ_r at a reference altitude z_r, measured with an off-the-shelf cup anemometer in the majority of cases. These quantities were translated into the observation vector

$$\mathbf{y} = [\mathbf{r}^T, \dot{\mathbf{r}}^T, w_r, \phi_r, F_t, \delta]^T \,, \tag{5.15}$$

where $\mathbf{r}$ and $\dot{\mathbf{r}}$ correspond to noisy observations of the position and velocity of the equivalent point-mass, $\hat{F}_t$ is a corrupted version of the cable traction force, and $\hat{w_r}$ and $\hat{\phi_r}$ represent the nominal wind speed and direction, respectively, at a reference height z_r. Except for a measurement noise, the measured wind speed w_r and direction ϕ_r are related to the nominal wind at the kite point-mass position by an assumed logarithmic wind shear profile:

$$\begin{aligned} w_r &= \frac{\log(z_r/z_0)}{\log(z/z_0)} \left\|\mathbf{w}_n\right\| \\ \phi_r &= \arctan\left(w_{ny}/w_{nx}\right) \,, \end{aligned} \tag{5.16}$$

where $\mathbf{w}_n = [w_{nx}, w_{ny}, 0]^T$ is the nominal wind at $\mathbf{r}$, $log(\cdot)$ is the natural logarithm, and z_0 is the surface roughness coefficient. Similarly, the measured traction force is related to the Lagrange multiplier ν and the aircraft point-mass position through the expression

$$\mathbf{F}_t = \mathbf{r}\,\nu \,. \tag{5.17}$$

Finally, regarding the observation δ, it does not model any physical quantity. It is, in fact, a made-up variable representing the inner product between the lift vector and the apparent wind:

$$\delta = \mathbf{F}_l^T \mathbf{w}_a \tag{5.18}$$

and is included in the filtering as a way to enforce the orthogonality

[1] Because of the modeling assumption of perfectly taut tethers, the direction of $\mathbf{F}_t$ is obtained from the position vector $\mathbf{r}$ of the equivalent point mass.

constraint between these two variables ($\delta = 0$), according to the perfect measurement technique already presented in Section 2.4.4.1. In practice, this means that the value of δ is always zero, and it is considered an extremely reliable observation, which in a Kalman filtering scenario implies that its associated covariance is negligible. Based on a thorough literature review, the inclusion of such an orthogonality constraint in the form of a measurement is a novel practice in AWE, being first reported in [59] as an early result of this thesis. Note that the approach is particularly favored in this formulation given that both the lift force and the apparent wind can be easily obtained from the filter state vector.

Even though initially only the knowledge of the aforementioned variables is assumed, it should be clear to the reader that the proposed filter can be easily extended to account for additional states and data, and hence to adapt to different AWE configurations.

As previously mentioned, the proposed filter allows for the computation of other important variables which are functions of its states. The equivalent aerodynamic efficiency E_{eq}, sometimes also called lift-to-drag ratio, of the whole airborne system can be computed as

$$E_{eq} = \frac{\|\mathbf{F}_l\|}{F_d} \,. \tag{5.19}$$

Provided the drag coefficient of the tethers is available (e.g. from the manufacturer's documentation), the drag component caused by these elements can be discounted from F_d, and Equation 2.2 can be used to calculate the aerodynamic coefficients of lift and drag of the aircraft only, assuming that its projected area A is a known parameter.

Finally, knowing from Section 2.1 that α_0 represents the angle between the wing chord line and the tangent plane at $\mathbf{r}$ of a sphere of radius $\|\mathbf{r}\|$, and assuming that α_0 is a known variable, then from the filter output we can also compute the angle of attack $\alpha = \alpha_0 + \Delta\alpha$, where $\Delta\alpha$ is given by

$$\Delta\alpha = \arcsin\left(\frac{\mathbf{w}_a^T \mathbf{r}}{\|\mathbf{w}_a\| \, \|\mathbf{r}\|}\right) . \tag{5.20}$$

5.4 Kinematics estimation module

In Section 5.3 it is assumed that the aircraft's position and velocity are always available to the aerodynamics estimator. This module, however, remains completely unaware of the actual source the data is obtained from, which is convenient due to a series of reasons discussed earlier. Although many different setups can theoretically be employed for measuring position and velocity in AWE applications, as seen in Section 4.4, all of them present severe drawbacks when operating under real world conditions.

Therefore, a measurement system inspired in [14] and based on lateration of range information is proposed as an attempt to provide AWE prototypes with reliable position and velocity estimates. Lateration, a positioning technique which relies on distance measurements between a mobile target and a series of reference points – also referred to as anchors – was chosen because of its advantages over other approaches: range information can be reliably obtained with simple, inexpensive hardware; it can be easily implemented e.g. using a closed form expression, an iterative algorithm, or by means of a Kalman filter; and finally, it scales well, and can be extended to support an arbitrary number of measurements, which means new reference points can be added as necessary for increasing robustness against noise.

In order to formulate the lateration problem, a scenario is considered in which a particle, representing the aircraft, is located at the position $\mathbf{r} = [x, y, z]^T$, and N reference anchors are scattered on the ground at known locations $\mathbf{r}_1, ..., \mathbf{r}_N$, with $\mathbf{r}_i = [x_i, y_i, z_i]^T$ surrounding the ground station. Moreover, it is assumed that the Euclidean distances between each anchor and the particle are measurable somehow and given by $d_1, d_2, ..., d_N$, as depicted in Figure 5.3. These distance measurements can then be ideally modeled as

$$d_i = \|\mathbf{r} - \mathbf{r}_i\| \tag{5.21}$$

If the true distances to the reference anchors could be measured exactly, i.e. if the sensing devices were ideal, the position of the target particle would be at the point of intersection of the spheres centered at these anchors and with radii given by $d_1, d_2, ..., d_N$. Although in theory a geometric technique could be used for finding this intersection, in

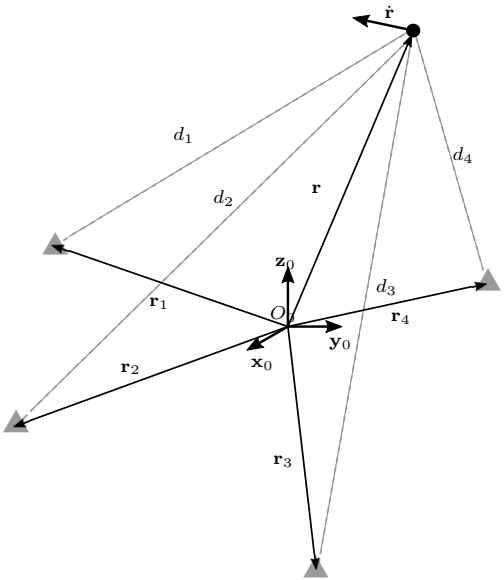

Figure 5.3: Lateration setup in an AWE application
Source: Original

real world conditions in which the measurements are contaminated by noise, such an approach would present severe limitations and, therefore, statistical methods are commonly employed [34]. A popular statistical positioning algorithm is the least squares estimation technique, which consists of finding the unknown position of the mobile target that minimizes the sum of squared discrepancies between the measured and the estimated distances.

5.4.1 Nonlinear least squares (N-LS) positioning

Given a set of distance measurements d_i modeled according to Equation 5.21, this approach estimates the position of the target particle by minimizing a least squares criterion J given by

$$J(x, y, z) = \sum_{i=1}^{N} \beta(\sqrt{(x - x_i)^2 + (y - y_i)^2 + (z - z_i)^2} - d_i)^2 \quad (5.22)$$

where β is a weighting coefficient which reflects the reliability of the i-th measurement. The solution to this optimization problem can be determined numerically e.g. by an iterative algorithm such as the gradient descent, yielding an estimator of the form

$$\hat{\mathbf{r}} = [\hat{x}, \hat{y}, \hat{z}]^T = \underset{x,y,z}{\operatorname{argmin}} \; J(x, y, z) \tag{5.23}$$

The estimator just described corresponds to the maximum likelihood (ML) estimator of the target position for independent noise components distributed according to $v_i \sim \mathcal{N}(0, \sigma_i^2)$ and for the weighting coefficient β given by $1/\sigma_i^2$. Since an ML estimator asymptotically achieves the Cramer-Rao Lower Bound (CRLB), the Nonlinear Least Squares (NLS) estimator provides an asymptotically optimal estimator under the stated conditions [34].

5.4.1.1 Gradient descent

The gradient descent, or steepest descent is a simple first-order iterative optimization algorithm for finding the minimum of a function f. The two main computational advantages of this algorithm are the ease of implementation and the low storage requirements necessary. As described in pseudocode in Algorithm 1, the main idea behind the gradient descent method is to continuously take steps proportional to the negative of the gradient of the function to be minimized at the current point, until a convergence criterion is satisfied or a maximum number of iterations is reached.

Algorithm 1 Gradient descent algorithm

```
1:  procedure GradientDescentOpt(f, x_0, α, ε, k_max)
2:      x_k ← x_0
3:      for k = 0; k < k_max do
4:          x_{k+1} ← x_k − α∇f(x_k)
5:          if |x_{k+1} − x_k| < ε then
6:              return x_{k+1}
7:          end if
8:          k ← k + 1
9:      end for
10:     return x_{k+1}
11: end procedure
```

In the case of positioning, the function f is given by Equation 5.22, and the learning rate α, the convergence criterion ϵ, the maximum number of iterations k_{max}, as well as the initial guess x_0 are all provided by the user. Note that, although it is common to use a variable learning rate, in this work α is assumed constant.

According to [65], one of the main advantages of the steepest descent method is that it has a nice convergence theory. It is also fairly easy to show that it has a linear rate of convergence, which is not too surprising given the simplicity of the method. Regarding its disadvantages, the same author points out that the method may present slow convergence depending on the nonlinear characteristics of the problem at hand.

Applying an iterative approach can, however, be time consuming and inconvenient to implement in many applications [33]. In such cases, it is also possible to solve the least squares through a closed form computation after linearizing the problem.

5.4.2 Linear least squares (L-LS) positioning

Starting from Equation 5.21, and assuming that there are four distance measurements available[2], one can write

$$\begin{aligned}
&\text{(Anchor 1)} \quad (x-x_1)^2+(y-y_1)^2+(z-z_1)^2 = d_1^2 \\
&\text{(Anchor 2)} \quad (x-x_2)^2+(y-y_2)^2+(z-z_2)^2 = d_2^2 \\
&\text{(Anchor 3)} \quad (x-x_3)^2+(y-y_3)^2+(z-z_3)^2 = d_3^2 \\
&\text{(Anchor 4)} \quad (x-x_4)^2+(y-y_4)^2+(z-z_4)^2 = d_4^2
\end{aligned} \tag{5.24}$$

By expanding the factors on the left of all equations in 5.25, and subtracting the equations corresponding to anchors 2,3, and 4 from that of anchor 1, one ends up with

[2]For the sake of simplicity, only four distance measurements were considered. Note however, that this same technique can be applied for an arbitrarily large number of anchors.

$$
\begin{aligned}
(x_1 - x_2)x + (y_1 - y_2)y + (z_1 - z_2)z = \\
\frac{1}{2}(d_2^2 - d_1^2 + x_1^2 - x_2^2 + y_1^2 - y_2^2 + z_1^2 - z_2^2) \\
(x_1 - x_3)x + (y_1 - y_3)y + (z_1 - z_3)z = \\
\frac{1}{2}(d_3^2 - d_1^2 + x_1^2 - x_3^2 + y_1^2 - y_4^2 + z_1^2 - z_3^2) \\
(x_1 - x_4)x + (y_1 - y_4)y + (z_1 - z_4)z = \\
\frac{1}{2}(d_4^2 - d_1^2 + x_1^2 - x_4^2 + y_1^2 - y_4^2 + z_1^2 - z_4^2)
\end{aligned} \tag{5.25}
$$

Note that Equation 5.25 can be expressed in matrix form as

$$\mathbf{Ar} = \mathbf{b} \tag{5.26}$$

where

$$\mathbf{A} = \begin{bmatrix} x_1 - x_2 & y_1 - y_2 & z_1 - z_2 \\ x_1 - x_3 & y_1 - y_3 & z_1 - z_3 \\ x_1 - x_4 & y_1 - y_4 & z_1 - z_4 \end{bmatrix} \tag{5.27}$$

$$\mathbf{b} = \frac{1}{2}\begin{bmatrix} d_2^2 - d_1^2 + x_1^2 - x_2^2 + y_1^2 - y_2^2 + z_1^2 - z_2^2 \\ d_3^2 - d_1^2 + x_1^2 - x_3^2 + y_1^2 - y_3^2 + z_1^2 - z_3^2 \\ d_4^2 - d_1^2 + x_1^2 - x_4^2 + y_1^2 - y_4^2 + z_1^2 - z_4^2 \end{bmatrix} \tag{5.28}$$

$$\mathbf{r} = [x, y, z]^T \tag{5.29}$$

The position of the mobile target is, therefore, given by

$$\mathbf{r} = (\mathbf{A}^T\mathbf{A})^{-1}\mathbf{A}^T\mathbf{b} \tag{5.30}$$

It is important to notice that, in order for the system to have an unique solution in 3D space, at least four reference anchors are necessary.

Finally, note that, in both the Linear Least Squares (LLS) and the NLS approaches, the velocity of the mobile target is determined by differentiating the position estimates, which is usually followed by a filtering step in order to mitigate the undesired effects of noise. While

intuitive, this solution does not allow velocity estimates to be employed in the future for constraining the trajectory of the target.

5.4.3 Extended Kalman Filter

Although easy to implement, and convenient to apply in most situations, the techniques described so far completely neglect the dynamics of the system. Moreover, they make it hard to introduce new information and to weigh different data sources. In order to overcome these limitations, and to make the kinematics estimation module more flexible and scalable, the application of an EKF is proposed again, this time for positioning.

The state vector of the EKF designed for the kinematics estimation module comprises the position and velocity of the mobile target, which in an AWE application are assumed to coincide with those of the aircraft. It is therefore given by

$$\mathbf{x} = [\mathbf{r}^T, \dot{\mathbf{r}}^T]^T . \tag{5.31}$$

These states are propagated at every time interval T_s according to a simple linear motion model, described by

$$\begin{aligned} \mathbf{r}_{k+1} &= \mathbf{r}_k + \dot{\mathbf{r}}_k T_s \\ \dot{\mathbf{r}}_{k+1} &= \dot{\mathbf{r}}_k \end{aligned} \tag{5.32}$$

While line angles, angular rates of change, and length measurements obtained in AWE applications are usually of high quality, which means they have a good signal-to-noise ratio, and could be employed alone for the determination of the aircraft position and velocity, this yields poor results when the assumption of rigid tether degrades, which happens at high altitudes or during the passive phase, as already discussed in Chapter 4. Meanwhile, as will be discussed later in the text, range information obtained with Radio Frequency (RF) based techniques remains reliable in these situations, but its quality decreases when the aircraft is flying at low altitudes, or the line-of-sight condition between it and the anchors is violated due to some obstacle, e.g. a tree or building. Acknowledging the complementary characteristics of line and range measurements, and in order to take the most out of the information available, the observation vector proposed for the EKF of the

kinematics estimation module is given by

$$\mathbf{y} = [d_1, d_2, ..., d_N, \theta, \phi, L, \dot{\theta}, \dot{\phi}, \dot{L}]^T , \tag{5.33}$$

with $d_1, d_2, ..., d_N$ being the ranges measured between the reference anchors and the mobile target (i.e. the aircraft), given in 5.21; θ, ϕ, and L being the polar angle, azimuth angle, and tether length, respectively, as measured at the ground station, and obtained as

$$\theta = \arctan(\frac{\sqrt{x^2 + y^2}}{z}) \tag{5.34}$$

$$\phi = \arctan(\frac{y}{x}) \tag{5.35}$$

$$L = \|\mathbf{r}\| \tag{5.36}$$

and $\dot{\theta}$, $\dot{\phi}$, and $\dot{L}$ being the rates of change associated with the angles and length of the tether. Knowing that

$$\mathbf{r} = \begin{bmatrix} L\sin(\theta)\cos(\phi) \\ L\sin(\theta)\sin(\phi) \\ L\cos(\phi) \end{bmatrix}, \tag{5.37}$$

the dynamic models these measurements can be obtained directly from the equation

$$\dot{\mathbf{r}} = \begin{bmatrix} \dot{L}\sin(\theta)\cos(\phi) + L(\dot{\theta}\cos(\theta)\cos(\phi) - \dot{(}\phi)\sin(\theta)\sin(\phi) \\ \dot{L}\sin(\theta)\sin(\phi) + L(\dot{\theta}\cos(\theta)\sin(\phi) + \dot{(}\phi)\sin(\theta)\cos(\phi) \\ \dot{L}\cos(\theta) - L\dot{\theta}\sin(\theta) \end{bmatrix}, \tag{5.38}$$

which is in turn obtained by differentiating Equation 5.37 with respect to time. They are given by

$$\dot{\theta} = \frac{\dot{L}\cos(\theta) - \dot{z}}{L\sin(\theta)} \tag{5.39}$$

$$\dot{\phi} = \frac{y - \dot{L}\sin(\theta)\sin(\phi) - L\dot{\theta}\cos(\theta)\sin(\phi)}{L\sin(\theta)\cos(\phi)} \tag{5.40}$$

$$\dot{L} = \dot{\mathbf{r}}^T \cdot \frac{\mathbf{r}}{\|\mathbf{r}\|} \tag{5.41}$$

The fusion of these information into the observation vector also provides the system with an increased robustness against failures in the underlying ranging mechanism, which could happen, for instance, due to environmental phenomena if the distance measurements were obtained through a RF based method. Finally, it allows for the estimator to continue working in the case of a tether break – situation in which line angle measurements become useless, and could be important for landing the aircraft safely.

Although it was initially assumed that the coordinates of each reference used for lateration were completely known in advance, this is not usually the case in most of the experimental setups. In such situations, the lateration system is commonly deployed only shortly before the realization of the experiment, and calibrated with general purpose instruments, potentially leading to inaccuracies. Moreover, for mobile systems it is simply impractical to survey the position of all reference anchors in every deployment site [14]. In order to mitigate undesired effects caused by inaccuracies in anchor locations, a self-calibration procedure could be convenient.

Aided by the EKF framework, this could be accomplished as in [14] by an augmentation of the state vector with the coordinates of the references r_i, and of the observation vector with the distances measured between each pair of anchors, yielding

$$\mathbf{x_{aug}} = [\mathbf{x}^T, \mathbf{r_1}^T, ..., \mathbf{r_N}^T]^T \tag{5.42}$$

$$\mathbf{y_{aug}} = [\mathbf{y}^T, d_{ij}]^T, \ i \neq j \tag{5.43}$$

According to [14], the estimation scheme based on range information with self-calibration is locally stable, which means it requires sufficiently accurate initial estimates of the aircraft and anchor positions to ensure convergence. The authors of [14] also point out that this is likely due to the use of the EKF, which can introduce significant linearization errors.

CHAPTER 6

Experimental setup and implementation

The previous chapter described a modular estimation structure targeted at AWE applications and designed to deliver estimates of several variables which, according to the literature review presented in Chapter 4, are useful for control, monitoring and optimization of wind power harvesting systems with tethered aircraft. In order to validate the proposed estimators, they were first implemented in a simulation environment and, after being proven functional, ported to the embedded platform of a small-scale AWE prototype available in the lab. In parallel, the hardware components responsible for measuring the required signals were built or adapted to fit the needs of the estimators. This chapter describes in detail all software and hardware elements involved in this work, and which allowed for the achievements of the results to be presented in Chapter 7.

6.1 Small scale prototype

Since its foundation, the UFSCkite research group – in the context of which this work was developed – has been concentrating its studies on AWE systems in the pumping-kite configuration with airborne actu-

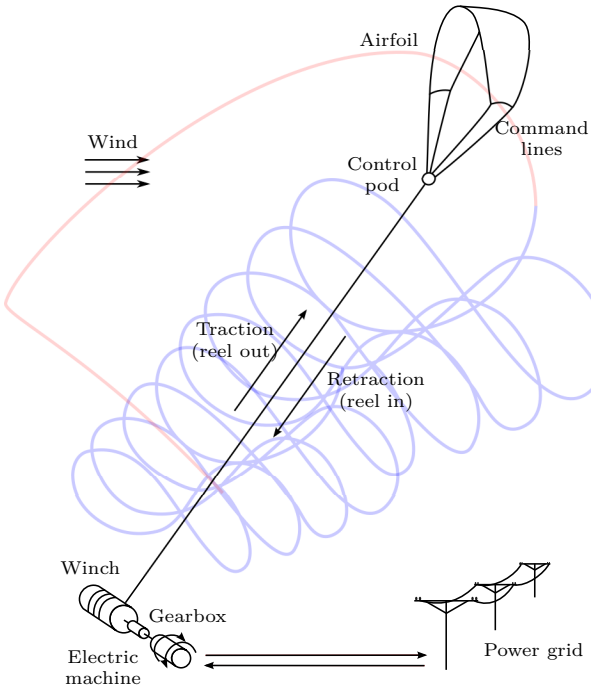

Figure 6.1: Conceptual overview of an AWE system in a pumping-kite configuration with an airborne flight control unit
Source: Original

ation, whose operating principle was previously described in Chapter 3. A conceptual overview of this kind of system is presented in Figure 6.1. Due to the complexity and inherent distributed characteristics of pumping-kite AWE devices, in order to facilitate their study, the group has decided to organize all analysis, development, and testing activities into two distinct parts: electricity generation, and flight control.

Given that in a pumping-kite scenario the electricity generation is highly dependent on the maintenance of a proper flight trajectory, which in turn is a responsibility of the elements in the flight control part of the system, this latter problem was chosen to be tackled first. In order to allow for the experimental validation of the control and estimation techniques studied by the group, a small scale AWE prototype was built[1] comprising a 3 m^2 foil (ram-air) kite tethered by means of

[1]Note that, although the author contributed to the improvement of the proto-

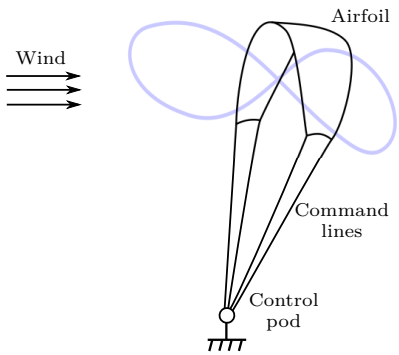

Figure 6.2: Conceptual overview of a prototype for independently testing the flight control strategies

Source: Original

45 m lines to a control pod designed in such a way that it could be fixed to the ground, as illustrated in Figure 6.2.

The resulting structure was equipped with measurement, processing, and actuation elements, which are illustrated in Figure 6.3. Among the instruments available are rotary encoders for measuring the tether angles and their rates of change, from which the airfoil position and velocity could be computed[2]; a cup anemometer meant to be installed at approximate height of 2.5 m, for measuring the wind speed and direction; and a load cell attached to an eye bolt, to which the traction line was tied, for measuring the traction force. For actuation, the prototype included two DC servo-motors which, together with a simple transmission mechanism, allow for a steering and a depower inputs to be applied to the airfoil, causing the exact same effects as the inputs described in the model of Section 4.1.1. Finally, a processing unit consisting of the single-board computer Beaglebone Black[3] was used for

type, especially in what comes to its embedded electronics, most of the development was conducted prior to the start of the activities reported in this document

[2]Velocity is computed by simply numerically differentiating the angular position measured by the encoders

[3]The Beaglebone Black is a low-cost, Linux-capable, community-supported single-board computer developed by Texas Instruments and which features the AM335x 1GHz ARM Cortex-A8 SoC, 512MB of RAM, and 4GB 8-bit eMMC onboard flash storage. For more details, refer to [66].

running the software to process the data from the sensors, compute the control laws, and adjust the actuators accordingly.

The control strategy executing on the prototype comprised an outer loop similar to that used in [37, 52], responsible for generating course angle references for a simple proportional controller in the inner loop. This cascaded structure leads to a behavior commonly known as *bang-bang*, in which the airfoil is always moving towards one of two attraction points. As soon as the kite overtakes the target in the azimuth direction the target is switched, resulting in a trajectory similar to a flattened lying-eight. The resulting prototype can be seen operational during a field test in Figure 6.4.

6.2 Positioning and communication infrastructure

The previous chapter presented an algorithm based on the Kalman filtering framework and on the lateration technique for the position estimation of a generic aircraft considering the constraints imposed by AWE applications. This approach, which was encapsulated into the so-called kinematics estimation module, relies on distance measurements, or ranges between the moving target (i.e. the aircraft) and a set of known locations scattered on the ground. By then, however, it was not specified where these measurements came from, except that a radio-frequency technique would be employed to obtain them. Unfortunately, the small scale prototype available for testing did not include any hardware suitable for ranging, and thus it was settled that the specification and development of such an infrastructure would be responsibility of the present author.

From an engineering point of view, the first decision faced during the development of the positioning solution presented in this thesis was whether the radio-frequency and signal processing electronics should be designed in-house, or if third-party solutions should be employed. In other words, the extent to which this work was going to rely on off-the-shelf solutions had to be defined. It was settled that due to aspects such as complexity and costs, the development of any low-level components should be left out of the scope of the thesis. An important argument was that, given the available resources, such an effort would hardly yield any result applicable for deployment into an

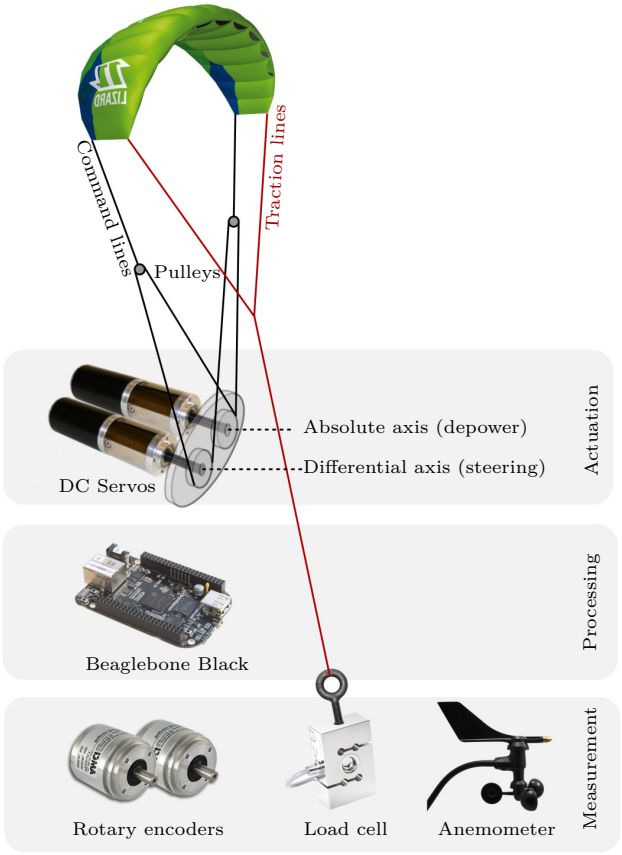

Figure 6.3: Hardware components of the UFSCkite prototype
Source: Original

Figure 6.4: Small scale AWE prototype in operation during one of the field experiments

Source: Original

Figure 6.5: The NSBEE radio module
Source: [67]

actual AWE prototype. Therefore, it was decided that this work should focus on delivering a fully functional positioning solution rather than on developing individual components, and that products available on the market should be employed whenever possible.

This section provides details about the solution found for measuring the distances required by the positioning algorithms, and gives the reader a general idea regarding deployment aspects of the proposed infrastructure.

6.2.1 The NSBEE module

After a thorough analysis of the different ranging devices available on the market, the NSBEE radio module developed by the german company Nanotron Technologies GmbH was selected as the ideal candidate

for providing the data needed for implementing the proposed positioning algorithm. The NSBEE module, whose specifications are presented in Table 6.1, is a 2.4 GHz autonomous radio node equipped with very precise low-cost ranging technology, and controlled by its comprehensive *swarm* Application Programming Interface (API) through a host microcontroller. It is based on Nanotron's second generation ranging and communication transceiver chip *nanoLOC*. Using a host microcontroller, an antenna and a battery as the only external components, NSBEE devices can be transformed into fully functional, low power radio nodes in a very short period of time. A comprehensive API command language eliminates the need for lower level firmware, and higher-level functions for measuring distance to another node, or sending a message, can be executed with a single command.

Parameter	**Value**
Frequency range	ISM band 2.4 GHz (2.4 - 2.4835 GHz)
Modulation	Chirp Spread Spectrum (CSS)
Transmission modes	80 MHz, 1 Mbps or 250 Kbps (80/1 or 80/4 mode)
TOA capture accuracy	<1 ns (better than 30 cm)
Typical air time per ranging cycle	1.8 ms
RF output power	Configurable - 22 t0 16 dBm
RF sensitivity	-89 dBm typ. @80/1 mode -95 dBm typ. @80/4 mode
RF interface	50 Ohm RF port (for external antenna)
Host interface (UART)	500 bps $\sim$ 2 Mbps
Power supply	3 - 5.5 V
Max. supply voltage ripple	20 mVpp
Active power consumption*	120 mA during transmission, 60 mA during receive in 80/1 mode
Power consumption in sleep mode*	5.5 mA
Power consumption in snooze mode*	4.5 uA
Power consumption in nap mode**	4.5 $\sim$ 600 uA
Power consumption in deep-sleep mode*	<1 uA
Operating temperature range	-30 $\sim$ 85 ^{o}C
Dimensions	40 mm x 24 mm x 3.5 mm
Weight	7 g
*Power consumption in all modes is measured at 20^{o}C, 3.3 V.	
**Power consumption in nap mode depends on interrupt sources (GPIO pins or MEMS or both).	

Table 6.1: Specifications of the NSBEE radio module
Source: [67]

Regarding its internal components, the NSBEE module consists of a

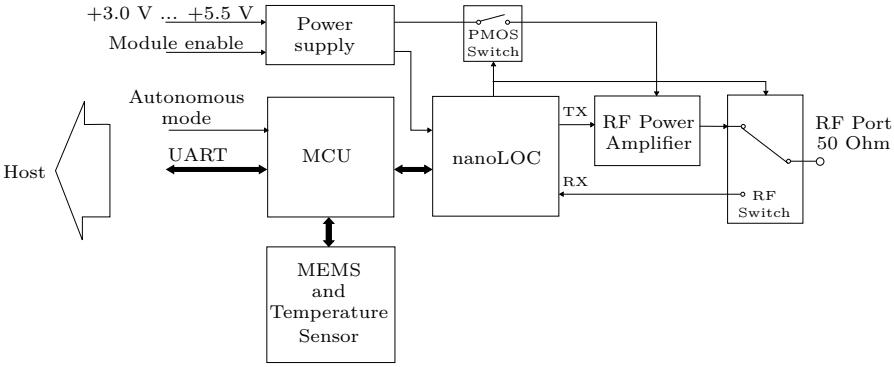

Figure 6.6: Internal representation of the NSBEE module
Source: Adapted from [67]

fully integrated ranging and communication transceiver, a power amplifier, a microcontroller, a MEMS accelerometer, and temperature sensor, as depicted in Figure 6.6. The whole module is powered from a single 3.3 V supply, and contains two physical interfaces, namely an UART and a 50 Ohm RF port. The transceiver is responsible for providing the module with robust wireless communication and ranging capabilities, and utilizes a technology patented by Nanotron known as Chirp Spread Spectrum (CSS). Besides increasing the robustness to disturbances and to the multipath fading effect, this technology allows for a lower power consumption, which makes it ideal for the application at hand. The microcontroller is assigned with the task of running the *swarm* API, and was selected by Nanotron due to its power consumption and performance characteristics. The NSBEE module also offers access to an on-board MEMS sensor, which measures accelaration in all three axes, and can detect changes such as shock or movement. Besides, the MEMS can measure temperature, and is accessible through the same API used for ranging and sending data.

6.2.1.1 Distance measurements

In order to measure distances, the NSBEE utilizes a technique known as Symmetrical Double-Sided Two-Way Ranging (SDS-TWR), whose principle is illustrated in Figure 6.7.

This method receives its name because it is symmetrical in that the

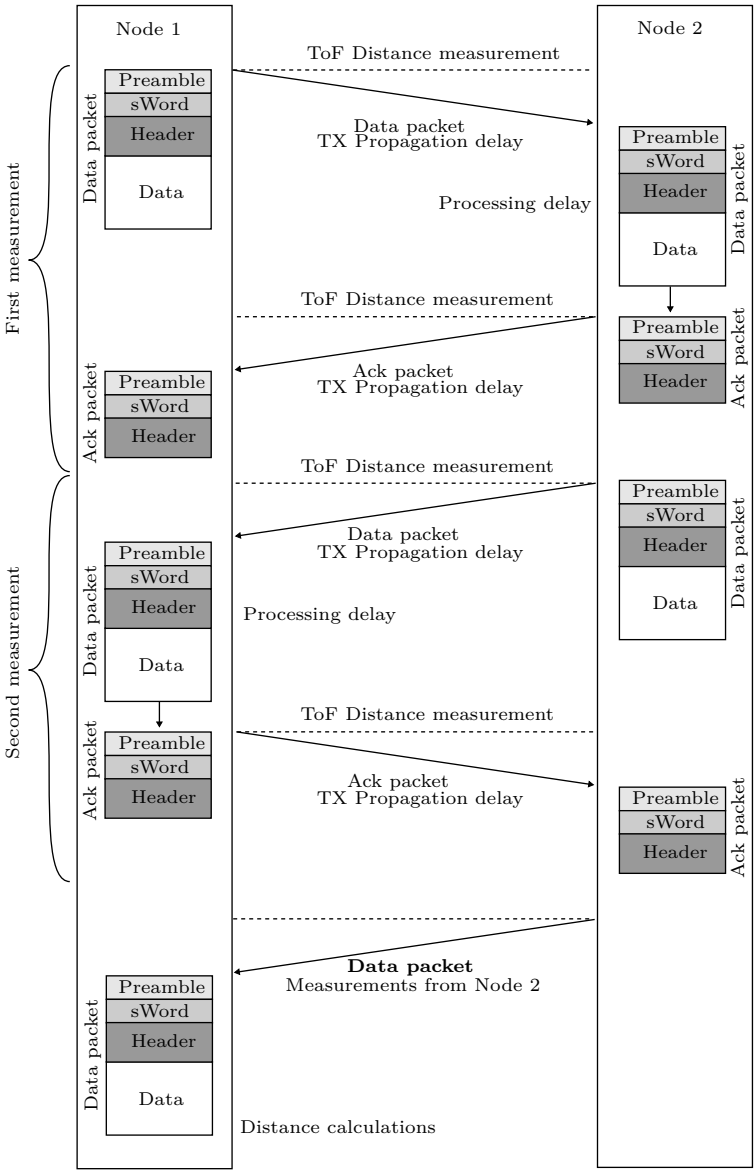

Figure 6.7: Working principle of the SDS-TWR technique implemented in the NSBEE modules

Source: Adapted from [67]

measurements from station A to station B are a mirror-image of the measurements from station B to station A; it is double-sided in that only two stations are used for ranging measurement; and it is two-way in that a data packet (also called a test packet) and an acknowledgement packet are used. As described in [67], the method makes use of two delays that occur naturally in signal transmission, namely the signal propagation delay between two wireless devices and the processing delay of acknowledgements within a device for determining the range between two stations.

The range measurement cycle starts with the transmission of a test packet from station A to station B. After transmission, station A waits for an acknowledgement packet from station B, which is not sent immediately, since it takes station B some time to process the incoming packet, generate the acknowledgement, and prepare it for transmission. The time interval between the reception of a test packet and the sending of an acknowledgement is known as processing delay, and its value is included in the acknowledgment sent by station B. When station A receives the acknowledgement packet, it is able to compute the round trip time based on the timestamp generated when the first packet was transmitted and on the processing delay measured by station B, according to the equation

$$rtt^A = 2\ t_{prop} + t^B_{proc} \tag{6.1}$$

where rtt_A, t_{prop}, and t_{proc} are the round trip time measured by station A, the propagation delay, and the processing delay in station B, respectively. Station B repeats the procedure by transmitting a test packet, which is acknowledged by station A after a processing delay, resulting in the equation

$$rtt^B = 2\ t_{prop} + t^A_{proc} \tag{6.2}$$

By combining these two equations, one is then able to determine the propagation time t_{prop}, which can be used together with the knowledge of the signal propagation speed to determine the distance between stations A an B. One possible solution is to add Equations 6.1 and 6.2 and isolate t_{prop}, yielding

$$t_{prop} = \frac{1}{4}(rtt^A - t^A_{proc} + rtt^B - t^B_{proc}) \tag{6.3}$$

Note that although the procedure just described required four exchanges of data (i.e. two test packets and two acknowledgements) for obtaining Equations 6.1 and 6.2, in Figure 6.7 there is a fifth packet being transmitted from station B to station A. This is because the final distance computation is assumed to take place in station A, and station B has to provide it with the times measured in the second part of the cycle.

It can be shown that errors introduced by clock drift, which are the major cause of inaccuracies in conventional two-way ranging, are minimal in SDS-TWR if the processing delays of the two stations, t^A_{proc} and t^B_{proc} are equal, and therefore this is the main assumption behind the technique. More details can be found in [68].

The main features that motivated the decision of using Nanotron's solution were:

- Dimensions and weight: Each radio module (breakout board included) measures about 50 x 30 mm and weighs no more than 15 g. These characteristics are of utmost importance considering that one of the devices is intended to be attached to the flight control unit of the AWE system, or to the wing itself in case the former is not present, and that the space available for extra payloads in such structures is usually very limited. Moreover, depending on where they are attached, excessive, or oddly-shaped loads could influence the dynamical characteristics of the system, potentially making it more difficult to control;

- Power consumption: The mobile node has to work on batteries, and its consumption has to be as low as possible given that AWE systems are constrained with regards to the power available for the onboard components. The NSBEE modules have an efficient energy management system, and there are several low power modes available which are capable of reducing the active stand-by consumption below 5 μA.

- Cost: Positioning solutions employed in current AWE prototypes tend to be very costly. Together, the line angle sensors and the inertial measurement unit used to obtain the position of the airfoil

in [13] cost about U$ 4800.00, which corresponds to roughly 16% of the total budget spent on the system. Another example is the pair of rotary encoders used for measuring the line angles in the first prototype developed by the UFSCkite team, which cost almost U$ 1000.00. Industrial grade GPS modules, as well as vision based tracking systems are too very expensive, and depending on their accuracy can cost several thousand dollars. The NSBEE radio modules, on the other hand, are sold by their manufacturer by € 99.00 a unit, which sums up to about € 500 considering that five of these devices are needed, one attached to the aircraft and four fixed at known locations. Moreover, the solution scales well, and for applications consisting of several AWE systems deployed close to each other (e.g. in a wind farm), the anchors can be shared and used as positioning references for multiple generating units, which dilutes the total cost even more;

- Independence on time synchronization infrastructure: Despite using TOF measurements to estimate distance to each other, NSBEE devices do not require any sort of time synchronization mechanism, which reduces the overall complexity of the system;

- Accuracy: According to their manufacturer, NSBEE devices can measure distances with an accuracy of 30 cm in open line-of-sight conditions. Although no exact accuracy requirements have been yet specified for positioning in AWE applications, it is believed that the accuracy provided by the NSBEE devices is enough for control purposes;

- Output rate: Given the fast dynamics of AWE systems, and knowing that the control loops used in the prototype in which the system will be installed has a sample period of around 50 ms, it is important that the position information is available at a compatible rate. Each ranging cycle between NSBEE devices takes around 1.8 ms, and considering that four ranges are necessary for determining the target's position, all measurements can be obtained in less than 8 ms;

- Operation range: The swarm bee is able to measure distances of up to 500 m, which is enough considering that the prototype in

which the system will be installed operates with a constant tether length of about 50 m. Even for larger prototypes, the operation range of the NSBEE is of the same order of magnitude of the maximum tether length;

- Ease of use (high-level API): All interactions with a swarm bee device happen by means of a hardware-independent API, accessible through a serial port, and which provides a series of high-level commands for controlling the hardware. The swarm API supports three protocols: ASCII, BINARY and AIR. The ASCII and BINARY options provide direct communication between an optional host controller and swarm radios using their serial interface. The AIR option provides wireless reconfiguration for swarm radio nodes, which can be very handy, especially when the anchors are deployed in rough terrain.

- Time-based measurements: The NSBEE radio relies on TOF for distance estimation, as opposed to RSSI, resulting in more reliable measurements, and immunity to many environmental effects that could jeopardize the operation of the system, as discussed in Section 2.5.

- Communication capabilities: Besides being able to measure ranges between each other, NSBEE devices are also capable of exchanging data by piggybacking a useful payload in the ranging packets. This is extremely convenient in AWE applications, because it allows for the same devices used for ranging to be used as a communication infrastructure between the ground and the airborne components of the system, cutting costs and complexity.

Since the NSBEE modules are supposed to be employed as a black box solution for measuring distances, and given that all interactions amongt the devices happen through an API implemented by the manufacturer, it was only necessary to develop a thin software layer for organizing the access to this API by the rest of the system. This layer, which was written in C as a header only library, comprises several data structures and functions e.g. for sending and receiving data, measuring ranges to a specific node, and configuring the device.

Regarding the hardware, the radio modules meant to be used as reference anchors were lodged together with a single-cell Lithium Polymer

Figure 6.8: Prototype developed for one of the lateration reference anchors
Source: Original

(LiPo) battery, an off the shelf battery management solution, and an on/off switch inside a plastic case specifically designed by the author and printed in 3D. The case was then attached to a wooden rod, which made the deployment easier, resulting in the structure seen in Figure 6.8.

For the mobile radio module, a more compact plastic case was designed. This enclosure, which allowed for the attachment to the aircraft through a piece of Velcro on its back is depicted in Figure 6.9. The whole experimental setup comprising the reference anchors and the mobile target is presented in Figure 6.10

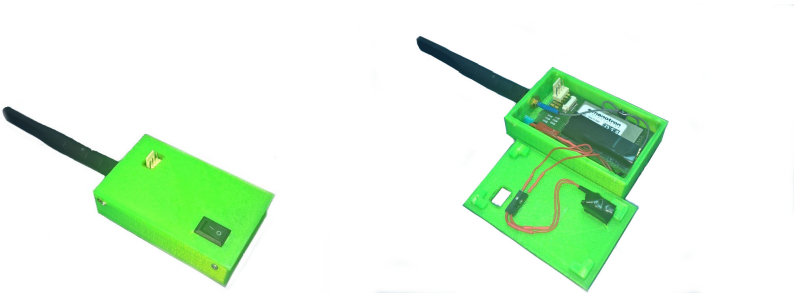

Figure 6.9: Prototype developed for the mobile radio target
Source: Original

Since the prototype available in the lab has no control pod, and all the hardware is located on the ground, the radio module attached to the airfoil had to be capable of operating in standalone mode. In order

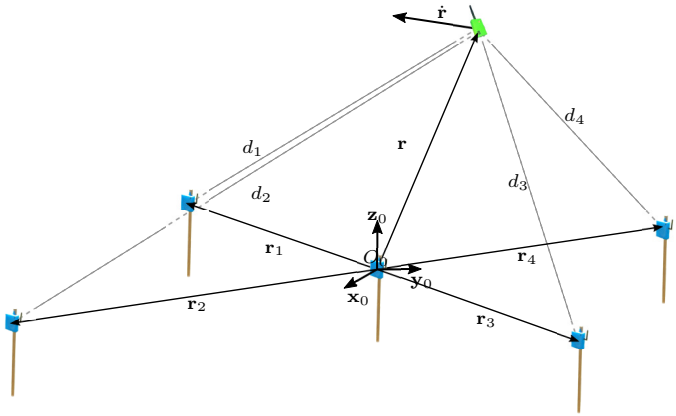

Figure 6.10: Overview of the experimental setup implemented for lateration
Source: Original

to achieve this, it was configured to broadcast a specific packet every 10 ms, forcing all other nodes in the region, i.e. the reference anchors, to initiate a ranging cycle with it. In addition, the anchors were configured to always broadcast the distance measurement at the end of each ranging cycle. Finally, the anchor meant to be installed closest to the tether anchorage point on the ground, and therefore to the processing unit of the prototype, was configured to capture (i.e. sniff) all packets containing distance measurements. Because this anchor was connected to the prototype, the setup allowed for all range measurements to be available to the software modules responsible for the kinematics estimation, which will be discussed in detail in the next section. Given that in the setup just described all anchors initiate a ranging cycle with the mobile target at about the same time, the Carrier sense multiple access with collision avoidance (CSMA) method, already implemented in the NSBEE radios, was used to detect and handle collisions in the medium.

Lastly, once the whole setup was functional, a simple experiment was carried out for the purpose of characterizing statistically the distance measurements obtained with the radio devices. The procedure involved positioning the mobile target at a distance of 5, 15, and 30 m from one of the anchors, and recording the measured ranges for a short period of time of around two minutes. The collected data was then used to obtain approximations of the PDFs of a random vari-

able corresponding to the measured distance. These PDFs, which are presented in Figure 6.11, can be approximated by the Gaussian distribution $p_d(\hat{d}|d = D) = \mathcal{N}(\mu = D, \sigma^2 = 0.09)$, whose parameters were later used for simulating the radio devices and also as a starting point for tuning the covariances of the Kalman filter in the kinematics estimation module.

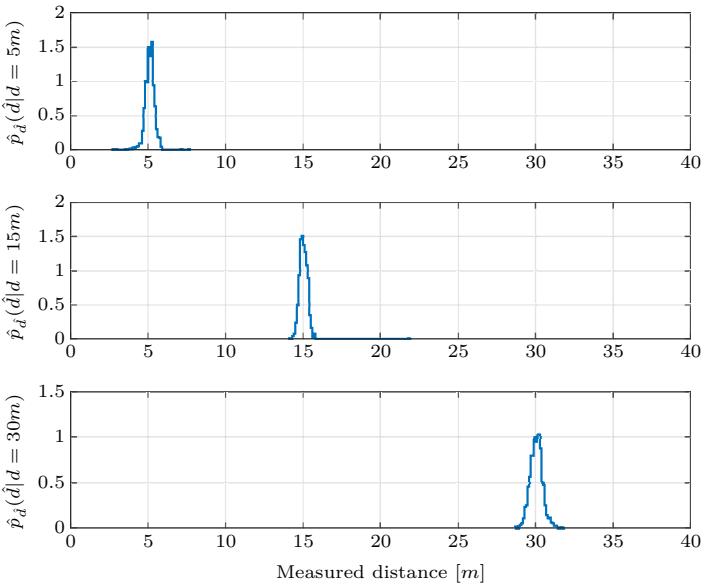

Figure 6.11: Probability density functions based on distance measurements between a fixed NSBEE module and a moving target standing at 5 m, 15 m, and 30 m

Source: Original

6.3 Embedded software

As discussed in the previous chapters, AWE systems comprise both ground and airborne structures, each of which with its own subcomponents. This results in an inherently distributed system with multiple physically separate, heterogeneous elements coupled together by means of mechanical or electrical connections. Teams involved in the development of AWE systems are usually composed of people from

different backgrounds and levels of expertise. Especially in academic environments, changes in the requirements, physical characteristics of the prototypes, and operating conditions are common, which requires great flexibility, especially from the software tools and components employed.

Considering this highly uncertain scenario, the UFSCkite research group decided to build the embedded software of its prototype on top of a lightweight platform developed specifically for this purpose. Regarding its architecture, this software platform is designed in such a way that it allows for AWE systems to be split into highly decoupled functional modules running in a distributed fashion as independent processes of the Operating System (OS), possibly across several computational units, and capable of exchanging information through a standard, high-performance communication infrastructure based on the publisher-subscriber pattern, as illustrated in Figure 6.12. Implementation intricacies are kept transparent to the end developer by means of a standardized API written in C, which provides extensible and versatile data structures upon which specific modules can be built and configured. Besides a carefully chosen set of dependencies, the platform also provides a series of facilities to the developer, including remote deployment, real-time monitoring, logging, code instrumentation and debug tools. Other advantages of the platform include high flexibility, low development and maintenance efforts, and ease of integration with external systems such as user interfaces and simulation environments.

6.3.1 Estimation modules

Given the characteristics of the embedded software platform used in the processing unit of the prototype available in the lab (i.e. the aforementioned Beaglebone Black), both the kinematics and the aerodynamics estimators described in Chapter 5 were implemented on top of it as independent modules and integrated with the rest of the system according to the diagram depicted in Figure 6.13. Additionally, a module for communicating with one of the RF devices and collecting all measured ranges was implemented. This latter module, which is also responsible for propagating the measured distance signals to the system, is basically a driver for the NSBEE radio, and was designed as a wrapper around the header only library mentioned in Section 6.2.

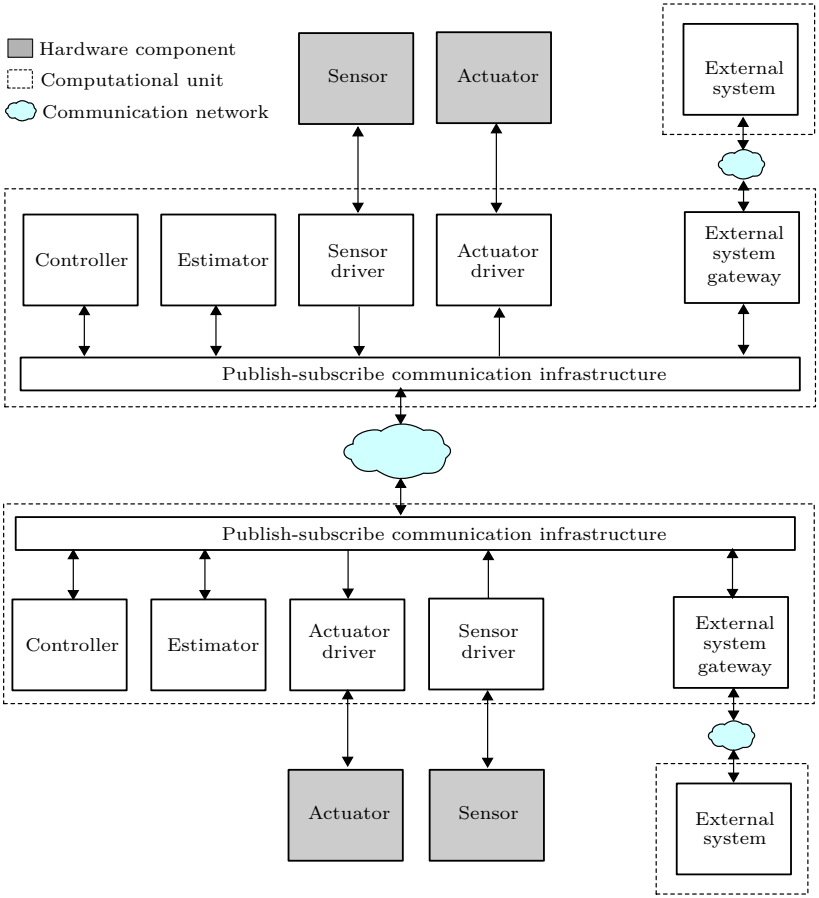

Figure 6.12: Example of a typical distributed application built on top of the software platform developed by the UFSCkite group
Source: Original

The EKF was implemented from scratch using only functions from the well established and computationally efficient numerical library GNU Scientific Library (GSL)[4]. The implementation was performed in such a way that enabled the same data structures and routines to be utilized by both the kinematics and the aerodynamics estimation modules, which need only to set the process and observation models to be employed by the filter in the configuration stage. All derivatives required by the EKF algorithm are computed numerically using first-order forward finite differences.

Regarding the code structure of the estimators, they were written following the standards enforced by the utilized embedded software platform, and as such, comprise two main routines: one for loading parameters, connecting to the communication infrastructure, and subscribing to specific information; and other for actually performing the computations necessary for the estimation. In this execution flow, which is similar to that commonly used in Arduino[5], the configuration procedure runs only once, as soon as the module is spawned, while the computation block is periodically executed. In the case of the implemented modules, 10 ms was chosen as an adequate execution period, whose maintenance was left entirely as a responsibility of the underlying software platform.

6.4 Simulation environment

In order to validate and assess the performance of the implemented estimation structure in laboratory conditions, a numerical simulation environment specifically targeted at dynamical systems and written in the Python programming language was employed. Within this environment, which was developed in conjunction with other students during the course of this work, a single point-mass model of a pumping-kite AWE system similar to that presented in [19] and described in Chapter 4 was built. The main parameters of the model were adjusted to approximately match those of the already described small-scale AWE

[4]The GSL is a free (GNU GPL licensed) numerical library for C and C++ programmers. The library provides a wide range of mathematical routines such as random number generators, special functions and least-squares fitting, adding up to over 1000 functions with an extensive test suite.

[5]Arduino is a famous open-source electronics platform based on easy-to-use hardware and software. For more details, see [69].

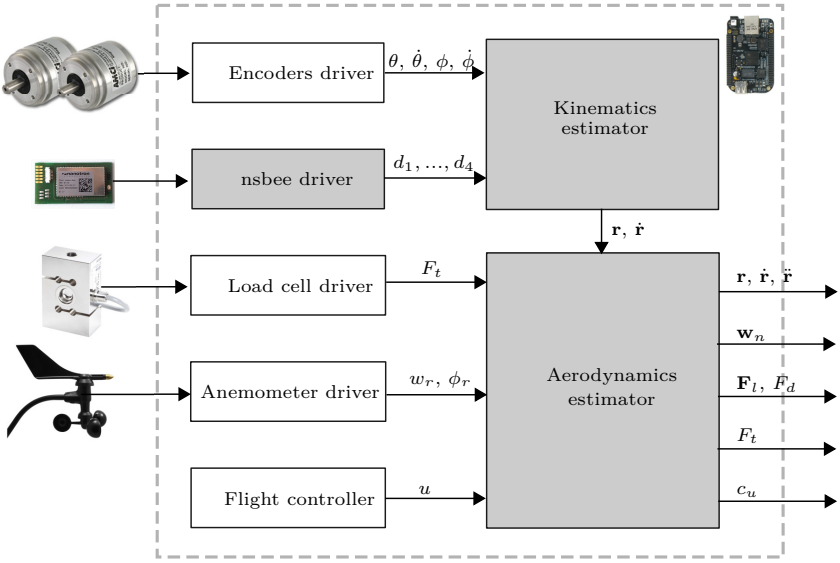

Figure 6.13: Data flow and implemented modules (highlighted) of the proposed estimation structure in a configuration intended for operation with the actual prototype

Source: Original

prototype available for testing, and are presented in Table 6.2. Regarding the aerodynamic characteristics of the airfoil, the lift and drag curves in [47] were employed. These curves were obtained for a rigid wing in a wind tunnel, and although they might differ from those of the flexible kite in the prototype, their utilization significantly simplified the simulation.

Among other advantages, the developed simulator made it possible to execute the model of the AWE system in real time, and to seamlessly integrate it with the embedded software in which the estimation modules were implemented, and also with a graphical user interface capable of monitoring the whole system. Moreover, it allowed for corrupting the measured signals with additive noise randomly sampled according to arbitrary distributions, which was convenient for verifying the robustness of the estimators in the face of uncertainty. By adjusting the

characteristics of the noise, one can more reliably replicate the actual operating conditions to which the estimation modules would be subject in the field.

Table 6.2: Model parameters of the AWE system

Parameter	**Value**	
	Simulation	**Prototype**
Airfoil area	3 m^2	3 m^2
Airfoil aspect ratio	3	3
Airfoil mass	0.5 kg	0.5 kg
Base angle of attack (α_0)	0 rad	(unknown)
Tether diameter	2 mm	2 mm
Tether density	970 kg/m^3	970 kg/m^3
Tether drag coefficient	1.2	(unknown)
Tether length (constant)	45 m	45 m

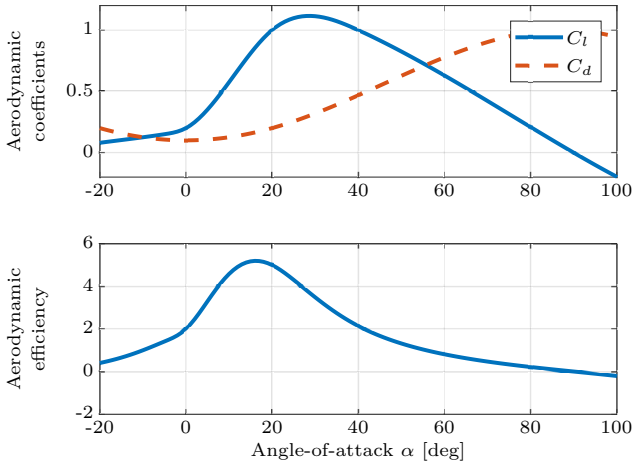

Figure 6.14: Aerodynamic coefficients used in the simulation environment
Source: Adapted from [47]

As opposed to the configuration illustrated in Figure 6.13, which is meant to work in the field with the actual AWE prototype, the integration of the embedded software platform together with the simulation environment made it possible to test the estimation modules in a Hardware-in-the-loop (HIL) scenario. In this setup, all peripheral drivers and peripherals are replaced by a *gateway* module and by the

previously described simulation environment, respectively. This setup, which is shown in Figure 6.15 allows for testing the estimators under controlled laboratory conditions, and was used extensively in this work, also for generating many of the results that will be presented in the next chapter. It is also worth mentioning that during the HIL experiments, the simulated airfoil was kept in flight by a two-stage controller similar to that described in [43], with gains conservatively adjusted to provide an overdamped closed-loop response.

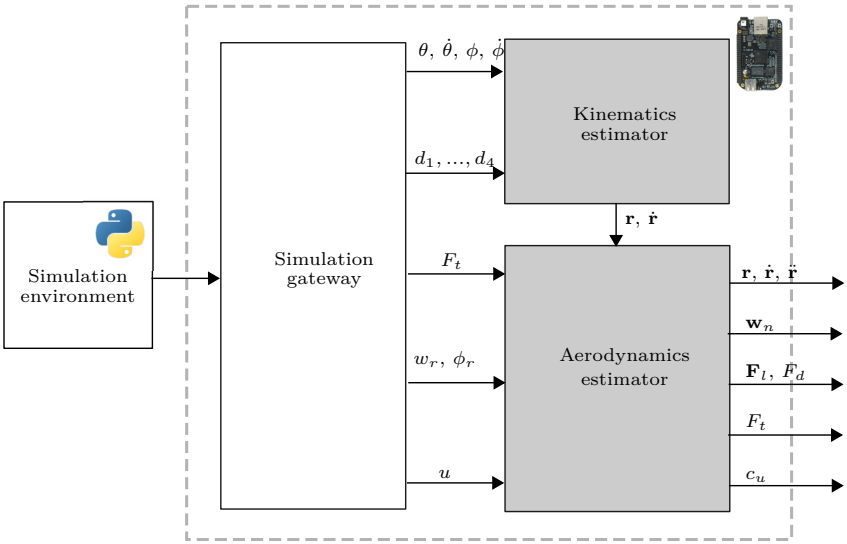

Figure 6.15: Data flow and implemented modules (highlighted) of the proposed estimation structure in a configuration intended for operation in a HIL environment

Source: Original

CHAPTER 7

Results

This chapter presents the results obtained with the proposed estimation structures whose design and implementation were described in Chapter 5 and 6, respectively. Both estimators were first tested in the HIL configuration described in 6.4 and illustrated in Figure 6.15. After this first stage, which allowed for the comparison of the estimated values with ground truth obtained from the simulation model, a new batch of tests was performed under actual operating conditions with a small scale AWE prototype. Although, due to the absence of ground truth data, this second scenario did not allow for a more formal evaluation of the estimators' performance, the results are qualitatively discussed based on a comparison with the values obtained in the laboratory.

7.1 Simulation results

In order to test the developed estimators, the simulation environment presented in the previous chapter was employed according to the diagram in Figure 6.15. The model parameters were adjusted according to Table 6.2 to match the characteristics of the small scale AWE prototype available in the lab. The test was then split into two different

Table 7.1: Simulated measuring instruments, observed variables, and their noise characteristics

Simulated instrument	**Variable**	σ	**Unit**
Rotary encoders	Angular position	0.052	rad
	Angular velocity	0.14	rad/s
Anemometer	Wind speed	0.14	m/s
	Wind direction	0.11	rad
Load cell	Tether traction	4.0	N
nsbee Radio	Ranges to anchors	0.3	m

phases in which the estimated variables were compared against their actual values, which in turn were available from the simulation model. In the first phase all sensors were assumed ideal, meaning that no noise was considered in the simulation. This was intended to confirm that the design and implementation of the estimators were correct. In the second phase, the observed signals were corrupted with additive zero-mean Gaussian random noise with standard deviations shown in Table 7.1, as an attempt to approximately represent actual measuring instruments. Besides allowing for an initial assessment of the quality of the estimation and its sensitivity to uncertainty in the measured signals, this setup served as a sandbox for tuning the filter parameters and preparing everything for the actual field test.

The characteristics of the noise applied to simulate the RF ranging devices were obtained from a Gaussian fit to the same experimental data used to generate Figure 6.11. Even though no significant levels of noise were observed in the measurements acquired from the rotary encoders available in the lab, the outputs of their simulated versions were still corrupted with the same noise proposed in [14] for simulating analogous instruments. The noise signals applied to the wind speed and direction, and to the tether traction, to simulate the anemometer and the load cell, respectively, were too specified based on data collected during experiments with these instruments. More specifically, the procedure involved taking the signals measured from these devices over the course of a whole experiment, removing their mean values – determined through low pass filtering of the original signals, and fitting Gaussian PDFs to the approximate distributions obtained from the resulting noise.

In this section, the results of both phases are presented side-by-

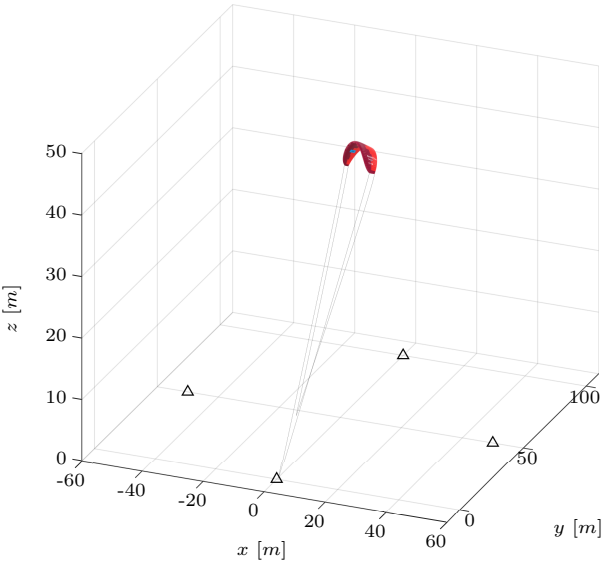

Figure 7.1: Coordinates of the positioning anchors used in the simulation
Source: Original

side for one realization, with the left and right columns corresponding to the case with clean and contaminated data, respectively. In order to facilitate the visualization and the interpretation of the results, all figures correspond to the same 25 s interval and also include, as dashed curves, the actual values of the system variables. One exception is the steering gain c_u, for which there is no equivalence in the simulation model.

For producing the results presented in this section, the EKF of the aerodynamics estimation module was adjusted with covariance matrices given by

$$\begin{aligned} \mathbf{Q} &= \text{diag}(0.2, 0.2, 0.2, 2, 2, 2, 5, 5, 5, \\ &\qquad 2, 2, 30, 30, 30, 30, 4, 0.1) \\ \mathbf{R} &= \text{diag}(0.25, 0.25, 0.25, 1, 1, 1, 0.02, 0.01, 10, 1e-10) \end{aligned} \quad , \tag{7.1}$$

and its initial state was set to

$$\mathbf{x}_0 = [40, 0, 40, 0, 0, 0, 0, 0, 0, 4, 0.2, 0, 0, 500, 300, 500, 0.001]^T \quad (7.2)$$

The kinematics estimation module, on the other hand, had its internal EKF adjusted according to the matrices

$$\begin{aligned} \mathbf{Q} &= \text{diag}(0.05, 0.05, 0.05, 10, 10, 10,) \\ \mathbf{R} &= \text{diag}(0.09, 0.09, 0.09, 0.09, ... \\ &\qquad 0.01, 0.01, ... \\ &\qquad 0.3, 0.3, ... \\ &\qquad 0.0001, 0.000001) \end{aligned} \quad , \quad (7.3)$$

and started from the state

$$\mathbf{x}_0 = [40, 0, 40, 0, 0, 0]^T \quad (7.4)$$

The anchors used as references for measuring the ranges to the aircraft were positioned according to Figure 7.1. Their locations were chosen in such a way that the baseline (i.e. the distance between any two anchors) was always greater than the length of the tether. Diagonal matrices were used to describe the uncertainty in the state propagation and in the observation models of the Kalman filters, and the matrices related to the observations had their elements adjusted according to the noise characteristics of the sensors already presented in Table 7.1.

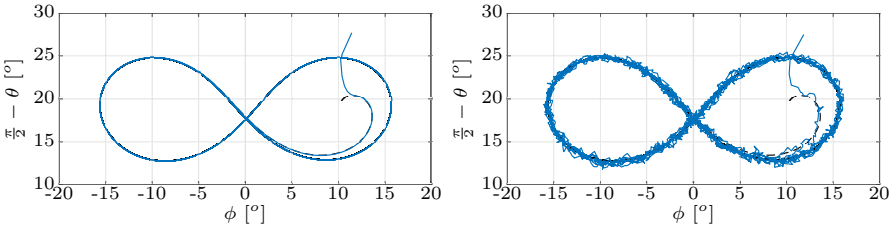

Figure 7.2: Estimated (solid) and actual (dashed) trajectory during simulations with clean and corrupted data

Source: Original

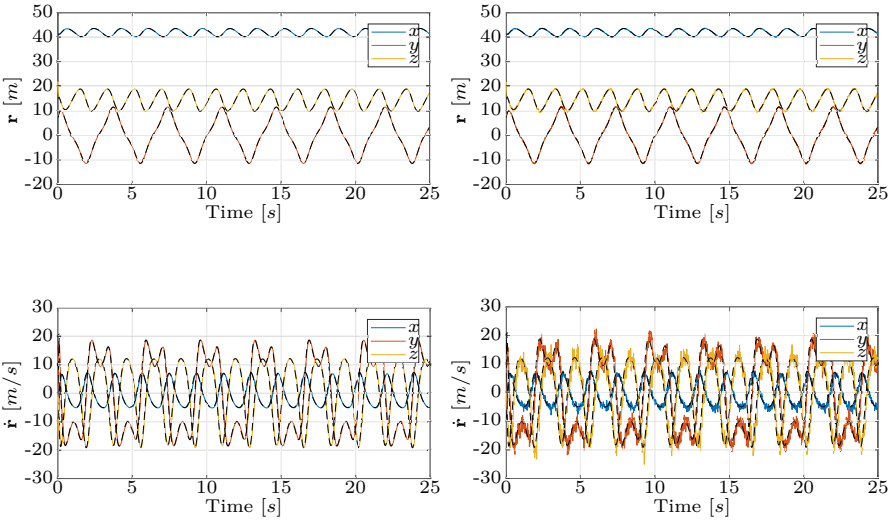

Figure 7.3: Estimated (solid) and actual (dashed) position and velocity during simulations with clean and corrupted data

Source: Original

During the simulations, the airfoil was driven by a two-stage controller with a lemniscate-shaped reference trajectory. The resulting flight pattern – as estimated by the solution described in Chapter 5, is plotted in the (ϕ, θ) plane in Figure 7.2.

Estimates of the airfoil position $\mathbf{r}$ and velocity $\dot{\mathbf{r}}$ are also presented in Cartesian coordinates in Figure 7.3. The aerodynamic lift force vector $\mathbf{F}_l$, as well as the magnitude of the equivalent drag force F_d, are both shown in Figure 7.4. Finally, the estimated nominal wind speed $\|\mathbf{w}_n\|$ is shown in Figure 7.5, and is followed by the estimated steering gain c_u in Figure 7.6. The equivalent aerodynamic efficiency E_{eq} and the dynamic angle-of-attack $\Delta\alpha$ computed directly from the estimated states according to the Equations 5.19 and 5.20 are presented in Figures 7.7 and 7.8, respectively. Theoretical values for the efficiency were obtained from the simulation model as

$$E_{eq} = \frac{C_l A}{C_d + 0.25\ n_t\, C_{dt}\, L\ d_t\ \cos(\Delta\alpha) A^{-1}}\,, \tag{7.5}$$

where A is the airfoil projected area in Table 6.2 and C_l and C_d are interpolated from the aerodynamic curves in Figure 6.14.

The estimators were able to successfully track all variables both in the case with clean and contaminated measurements. In the scenario in which there is no measurement noise, the estimates converged to the actual values with negligible error. Convergence was still achieved when the measurements were corrupted, but in this case part of the noise was propagated to the estimated states. Nonetheless, if one looked at the expected value of the estimates, they still match the ground truth.

7.2 Experimental results

The proposed estimation solution has been also validated under actual operating conditions with the small scale AWE prototype described in Chapter 6. This prototype was deployed at the center of an open field next to a positioning anchor like that of Figure 7.9, and with three other anchors around it.

In the field experiments, whose outcomes are presented in this section, the EKF of the aerodynamics estimation module was adjusted with covariance matrices given by

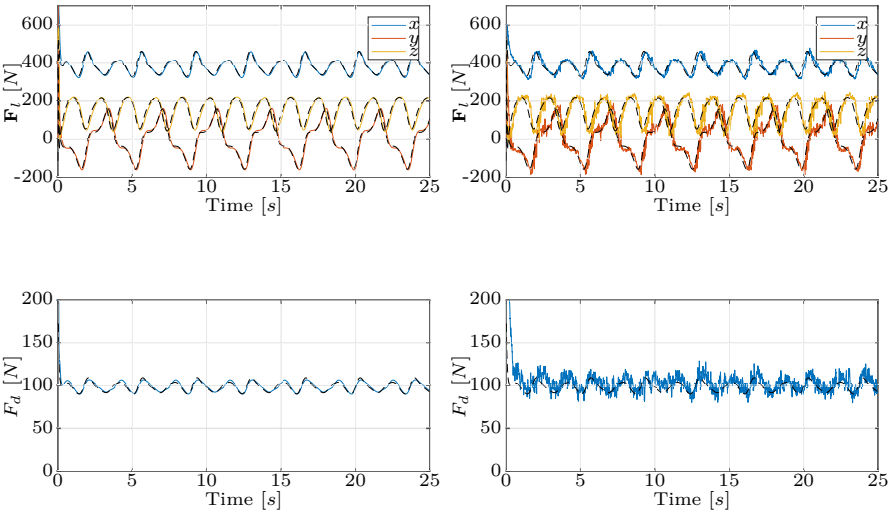

Figure 7.4: Estimated (solid) and actual (dashed) lift and equivalent drag forces during simulations with clean and corrupted data

Source: Original

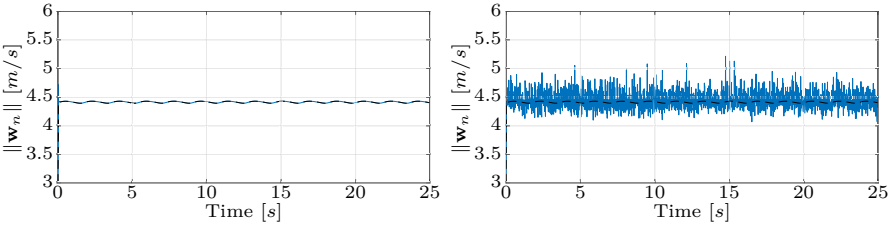

Figure 7.5: Estimated (solid) and actual (dashed) nominal wind speed during simulations with clean and corrupted data

Source: Original

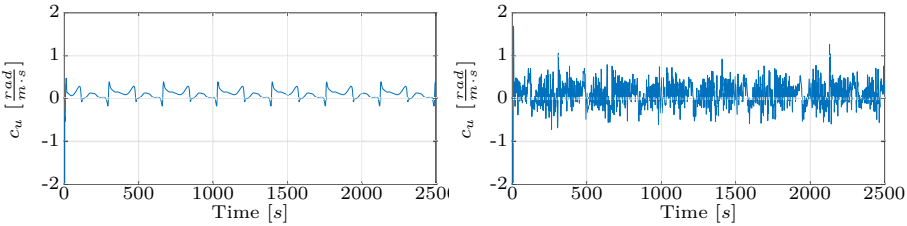

Figure 7.6: Estimated steering gain during simulations with clean and corrupted data

Source: Original

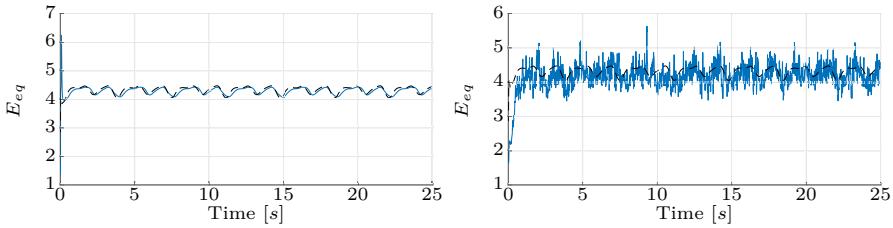

Figure 7.7: Estimated (solid) and actual (dashed) equivalent aerodynamic efficiency during simulations with clean and corrupted data

Source: Original

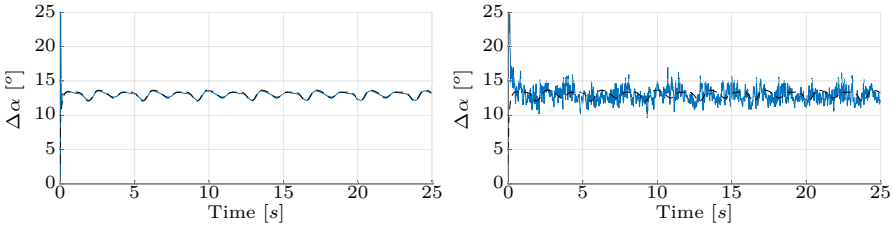

Figure 7.8: Estimated (solid) and actual (dashed) dynamic angle-of-attack during simulations with clean and corrupted data

Source: Original

Figure 7.9: Positioning anchor deployed on the test field
Source: Original

$$\begin{aligned}\mathbf{Q} &= \text{diag}(0.2, 0.2, 0.2, 0.2, 0.2, 0.2, 0.5, 0.5, 0.5, \\ &\qquad 2, 2, 300, 300, 300, 300, 100, 0.1) \quad , \\ \mathbf{R} &= \text{diag}(0.25, 0.25, 0.25, 1, 1, 1, 0.02, 0.01, 10, 1e-10)\end{aligned} \tag{7.6}$$

The kinematics estimation module had the state covariance matrix of its EKF adjusted according as

$$\mathbf{Q} = \text{diag}(0.01, 0.01, 0.01, 1, 1, 1) \quad , \tag{7.7}$$

All other parameters were adjusted identically to those used in the simulations and already presented in Section 7.1.

The coordinates of the anchors were initially determined with a tape meter, in a highly unreliable procedure, and the distances between them were measured through an approach which involved manually positioning the mobile radio device next to each anchor, and averaging the measurements collected during an interval of around two minutes. These measurements were then fed to an optimizer based on the same gradient descent algorithm of Section 5.4.1.1. Starting from the coordinates determined with the tape meter, and based on the distances measured between the anchors, this optimizer was responsible for refining the coordinates of all anchors except for the first one, which was assumed to be at the origin. This semi-automatic, off line calibration process can be more formally written as

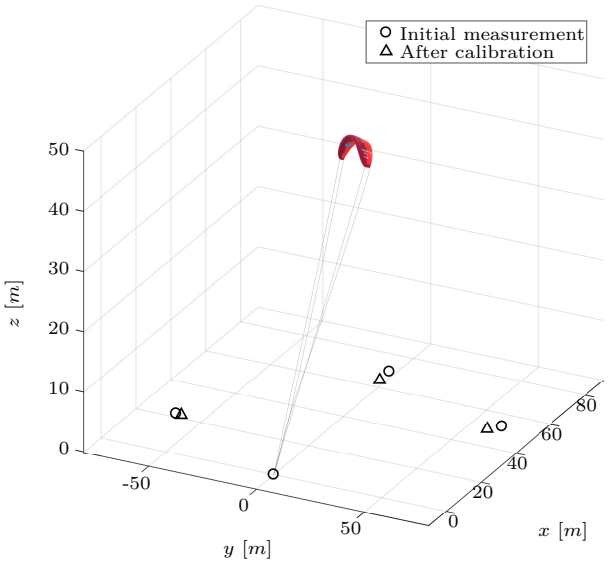

Figure 7.10: Coordinates of the RF anchors before and after calibration
Source: Original

$$\hat{\mathbf{r}}_2, \hat{\mathbf{r}}_3, \hat{\mathbf{r}}_4 = \underset{\mathbf{r}_2,\mathbf{r}_3,\mathbf{r}_4}{\operatorname{argmin}} \sum_{i=1}^{4} \sum_{j=1}^{4} (\|\mathbf{r}_i - \mathbf{r}_j\| - d_{ij})^2 \,, \tag{7.8}$$

where $\mathbf{r}_2$, $\mathbf{r}_3$, and $\mathbf{r}_4$ correspond to the coordinates of three of the anchors, and d_{ij} is the distance measured between anchors i and j. The relative layout of the anchors with respect to the prototype during the field test, as well as the result of the calibration process just described are illustrated in Figure 7.10. It is noticeable how the coordinates of the anchors after calibration differ from the initial measurements obtained with the tape meter, which corroborates the importance of a calibration step.

With the positioning anchors properly calibrated, the airfoil was manually launched, and as soon as it reached a reasonable altitude, the automatic controller discussed in Section 6.1 was activated. As a result, the airfoil started following a lying-eight trajectory similar to that presented in the time lapse of Figure 7.11, which also shows

Figure 7.11: Small scale prototype and time lapse of the kite trajectory
Source: Original

the prototype in operation on the field, and gives a better idea of the conditions in which the experiment was carried out. As expected, the estimators remained stable during the whole course of the experiment, and their states converged to values approximately similar to those obtained in the simulation. The results obtained during a 25 s interval extracted from data collected in the experiment are presented next, together with a discussion regarding the behavior and quality of the estimates.

The wing angular position and velocity as output by the filtering solution are presented in Figure 7.12 and compared against measurements of the same variables obtained with rotary encoders. Note that the polar angle θ measured with the encoder is almost always larger than that output by the estimator. This behavior might be caused by tether sag, whose theoretical effect on the measured polar angle is illustrated in Figure 7.14. Moreover, it can be too observed that the measured azimuth angle ϕ seems to be an slightly attenuated version of its estimated counterpart, which is probably caused by the dynamics introduced by the flexible tether. Both the measured angles and rates of change are also clearly delayed with respect to their estimates. Together, these discrepancies, which are in agreement with the behavior observed in [14] during flight simulations performed with a flexible tether model, indicate that effects caused by the non-rigidity of the tether are indeed present in actual AWE systems, and might be significant even for short tether lengths, confirming that the work developed

in this thesis was well motivated. Finally, the results show that setups based on RF ranging devices, for which there were still no reported experimental results in the literature, can be effectively used for the purpose of determining the position and velocity of tethered aircraft, and represent a promising solution for AWE applications.

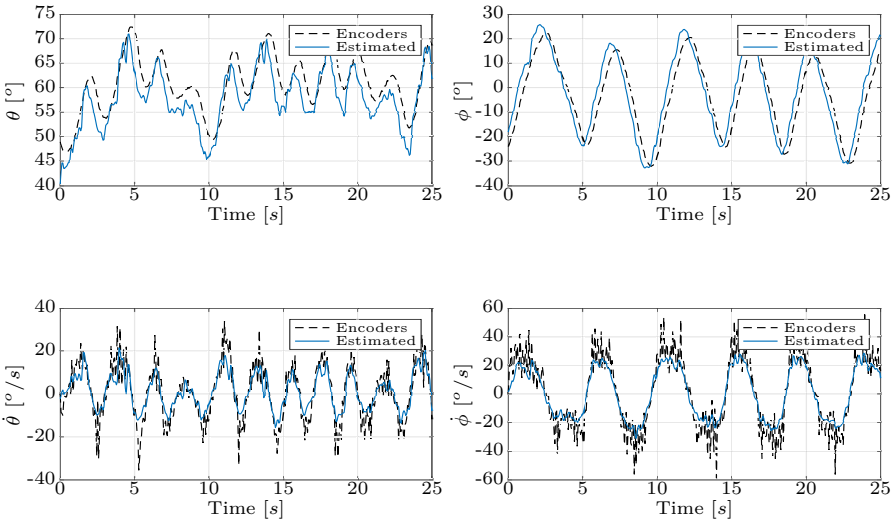

Figure 7.12: Polar and azimuth angles, their rates of change, and corresponding measurements obtained from the rotary encoders during a field test
Source: Original

In order to allow for a comparison of the experimental with the simulated results, the aircraft's position and velocity estimates are also presented in Cartesian coordinates in Figure 7.13. It can be seen that the waveforms in this figure are very similar to those of Figure 7.3 in the previous section, which show that the estimators are working properly. One difference is in the average flight altitude, (visible in the curve representing the z coordinate of the $\mathbf{r}$ vector), which in the experiment is higher than that observed in the simulations, because of differences in the parameterization of the reference trajectory.

The estimated aerodynamic lift force acting on the system is displayed side-by-side with the also estimated equivalent drag force in Figure 7.15. Note that, although both forces resemble in shape, and

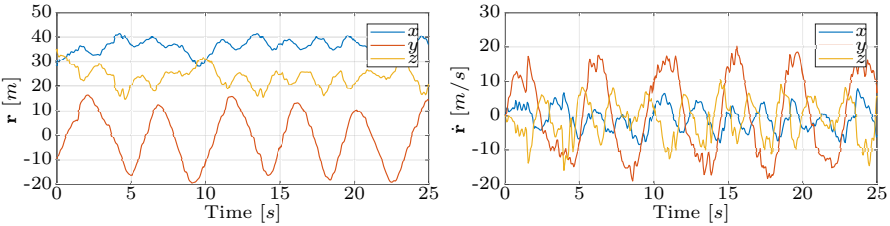

Figure 7.13: Position and velocity estimates in Cartesian coordinates during a field test

Source: Original

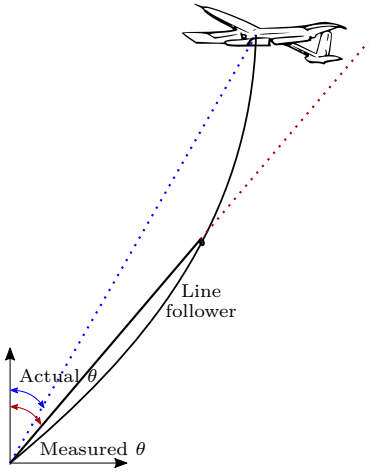

Figure 7.14: Influence of tether sag in the polar angle measured with a rotary encoder

Source: Original

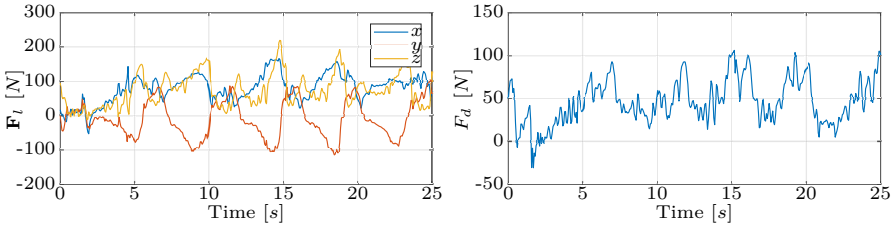

Lift force

Equivalent drag force

Figure 7.15: Lift force and equivalent drag estimates during a field test
Source: Original

seem to be coherent with the curves obtained in the simulation, in the field experiment they present significantly smaller magnitudes. From the analysis of the aircraft position estimates shown in Figure 7.13, it was concluded that there is also a difference between the polar angle chosen as the center of the reference trajectory in these two scenarios, which affects the angle-of-attack, and ends up impacting the aerodynamic forces, thus explaining this behavior. In the field test, in which the wing was flying at a smaller polar angle, it makes sense that the aerodynamic forces are not as large as one would expected if the airfoil was flying closer to the ground, and therefore more perpendicular to the wind. It is also worth pointing out that even though no constraints were imposed in this direction, the estimated equivalent drag is always positive, which was expected since this state in fact represents the norm of this force.

In Figure 7.16 the estimated speed of the nominal wind at flight level is presented and compared to the wind speed measured with the anemometer. The same figure also displays the values estimated for the steering gain c_u, which although very noisy, resembles the curves obtained in the simulation.

The estimated states are once again combined through Equations 5.19 and 5.20 to compute estimates of the equivalent aerodynamic efficiency of the system, and of the dynamic angle-of-attack of the airfoil, which are both presented in Figure 7.17. It can be observed in the figure that the small drag magnitudes, associated with the noise present in the estimates led to expressive levels of noise in the estimated efficiency, which floats around the value of 3.5. Another interesting be-

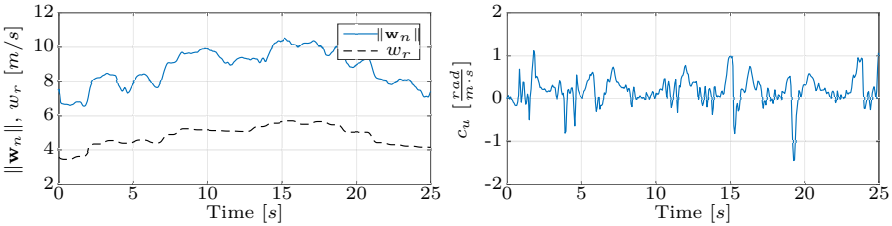

Figure 7.16: Nominal wind and steering gain estimates during a field test
Source: Original

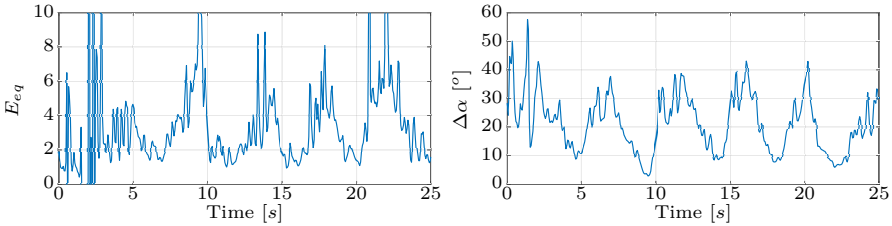

Figure 7.17: Equivalent aerodynamic efficiency and dynamic angle-of-attack estimates during a field test
Source: Original

havior noticeable in Figure 7.17 is the apparent negative correlation between the angle of attack and the equivalent efficiency. The joint observation of these two variables allows one to infer about the shape of the aerodynamic curves in a vicinity of the operating point. Based on the experimental results, it can be concluded that the prototype was operating beyond its point of maximum efficiency, which is probably located next to $\alpha = \Delta\alpha \approx 0^\circ$, in a region where increases in the angle of attack cause the aerodynamic efficiency to decrease.

In order to give an idea of the relationship between angle-of-attack and aerodynamic efficiency, scatter plots of this latter variable as well as of the equivalent drag coefficient C_{deq} of the system – calculated according to Equation 2.2, are presented as functions of $\Delta\alpha$ in Figure 7.18. If the behavior of the resulting data points could be explained by some mathematical law, the format of the underlying functions would

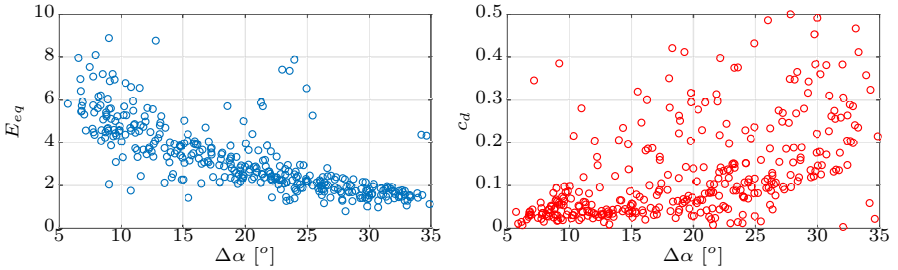

Figure 7.18: Scatter plot of the equivalent aerodynamic efficiency and of the drag coefficient as functions of the dynamic angle-of-attack based on estimates obtained during a field test

Source: Original

be quite similar to those previously shown in Figure 6.14, assuming that only a small segment of the horizontal axis was covered during the experiment. This is an indication that the designed estimator is producing coherent results.

Finally, if one could continuously adjust the base angle of attack during flight to cover more of the α axis, aided by the proposed solution it would then be possible to fit on-line a curve to these data points, and therefore "learn" the aerodynamic characteristics of the system, which in the literature so far has only been possible through expensive and cumbersome wind tunnel experiments.

CHAPTER 8

Final remarks

This thesis presented an estimation strategy comprising an experimental setup and a two-stage cascaded filtering structure specifically designed for AWE applications and capable of obtaining in real time estimates of the aircraft position and velocity, as well as of the wind conditions at flight level and of the resulting aerodynamic forces acting upon the system. The setup is based on a minimal set of information obtained by sensors commonly found in AWE prototypes, or that can be easily acquired, and therefore remains suitable for deployment by other groups working in the field. Based solely on the estimated quantities, it was shown that the computation of variables such as the aircraft's dynamic angle-of-attack, as well as its aerodynamic characteristics is straightforward, which can benefit control and optimization techniques depending on these quantities.

The developed estimation structure can be seen as a flexible platform on top of which AWE researchers and developers could build their own solutions, similarly to what is illustrated in Figure 8.1. Besides using the estimated aircraft's position and velocity for control purposes, one could, for instance, correlate the estimated lift and drag coefficients with knowledge of the angle-of-attack to obtain accurate models

of a given airfoil – something that so far has only been possible with complex wind tunnel experiments. This information could in turn help designers come up with more efficient aircraft, or be employed in real time anomaly detection modules for identifying sudden changes in the lift and drag curves and determining whether they were caused e.g. by stall conditions or by a damaged wing. Another possibility is to use the efficiency information yield by the estimator for adjusting parameters of the control systems in order to drive the aerodynamic efficiency to a desired value, and hence maximize the generated power. Finally, the estimated wind conditions could help in the process of assessing the wind potential at high altitudes of a candidate deployment site, which is currently only possible with expensive equipment.

Two main contributions can be identified in this work. The first one is the utilization of distance measurements obtained by radio-frequency ranging devices as inputs for helping determine the aircraft's position and velocity during an actual field test. This solution has many advantages over more conventional techniques and to this date real world results involving its usage had not been reported in the literature. The other is the estimation of the aerodynamic forces with the enforcement of an orthogonality constraint between the lift and the apparent wind through the so-called perfect measurement method, whose utilization is a novelty in AWE literature. Although simple, this solution demonstrates that Kalman filter-based estimators can be used in AWE applications and have their performance improved without significant increases in the computational requirements and complexity of the system, allowing for the estimation of important variables with a reasonable level of accuracy. The importance of these contributions were confirmed by the AWE community during an invited section within the 20th World Congress of the International Federation of Automatic Control, in which early results derived from this work were presented.

Although they are not at the center of the thesis, and have been only briefly mentioned in the text, the simulation environment, the embedded software platform, the graphical user interface, and the hardware described in Chapter 6 have all demanded a significant amount of time and effort from the author, and can too be seen as secondary contributions of this work. The importance of these contributions in the context of AWE prototyping have already been noticed in the laboratory, and

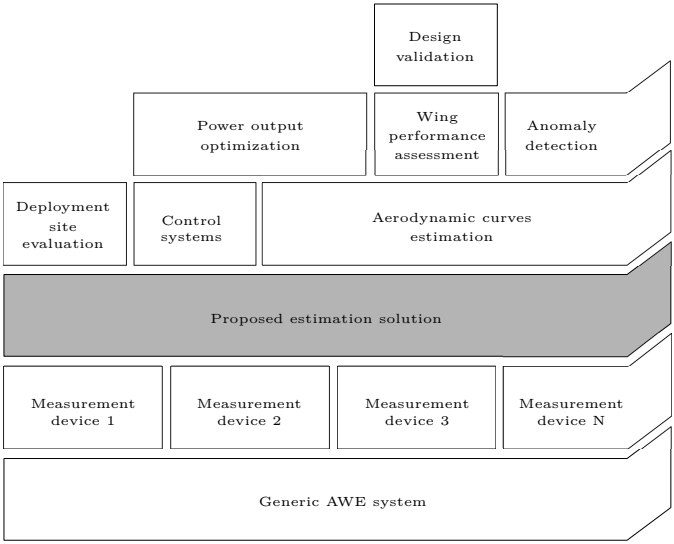

Figure 8.1: Estimation solution as a platform for higher level modules
Source: Original

they will surely lead to publications in the future.

8.1 Future work

The work described in this document represented a first step towards the goal of developing a complete, robust estimation solution for AWE systems capable of tracking important variables without wasting any of the available data. As such, this first iteration was not expected to tackle all the problems at once and, therefore, there are still a lot of studies to be performed and improvements to be done. More specifically, the models used to describe the dynamics of the system at this first stage were extremely simple, and did not take into account the attitude of the wing, nor the flexibility of the tether. Another limitation of the proposed solution is its rather strong dependency on the model describing the wind conditions as a function of the altitude. Moreover, it has been observed that the kinematics estimation module can be very sensitive to measurement noise, especially when information about the aircraft's velocity is absent from the observation vector or highly unreliable. Finally, as a direct result of employing extended

Kalman filters in both stages of the estimation structure, there is no way of guaranteeing the convergence of the observer, and the user is required to adjust a large number of parameters (i.e. the covariances of the filter) prior to operation, in a trial and error approach until convergence is achieved. In order to overcome these, and other identified shortcomings, the following future works are suggested:

- Improvement of the quality of the speed measurements, for instance, by filtering the derivative of the value measured by the rotary encoders;
- Inclusion of accelerometer data to improve velocity estimates and reduce dependency on the encoders;
- Inclusion of airspeed sensors on the aircraft in order to reduced dependency on the assumption of a logarithmic wind profile;
- Employment of a more complex dynamical model for the kite motion;
- Modification of the kinematics estimation module to allow for automatic calibration of the reference anchors, as described in Section 5.4.3;
- Employment of a more complex filtering algorithm for which convergence guarantees can be obtained, e.g. the Moving Horizon Estimator;
- Execution of an observability analysis of the proposed estimation strategy;
- Study of the sensitivity of the proposed estimation strategy to modeling inaccuracies and measurement noise;
- Testing of the estimation solution with different aircraft and under adverse operational conditions.

It is worth stressing that most, if not all, of these improvements are fairly easy to be implemented thanks to the design decisions taken during the development of the estimators.

A future work related to this thesis but not specifically targeted at improving the proposed solution is the publication of three other papers, addressing:

- A comparison of the EKFs by other estimation methods such as the MHE and the Fast Orthogonal Search (FOS) which offer theoretical guarantees regarding convergence and might provide a better accuracy;
- The online identification of the aerodynamic curves of different types of airfoil;
- The potential of using radio frequency ranging devices for positioning in AWE applications;

References

[1] The Swiss Wind Power Data Website, "Wind profile." http://wind-data.ch/tools/profile.php?lng=en, 2013. Acessed October 7, 2016.

[2] UCS, "A short history of energy." http://www.ucsusa.org/clean_energy/our-energy-choices/a-short-history-of-energy.html, 2015. Acessed March 30, 2017.

[3] IEA, *World Energy Outlook*. IEA, 2016.

[4] EIA, *International Energy Outlook*. EIA, 2016.

[5] M. Canale, L. Fagiano, and M. Milanese, "High altitude wind energy generation using controlled power kites," *IEEE Transactions on Control Systems Technology*, vol. 18, no. 2, pp. 279–293, 2010.

[6] IEA, *World Energy Outlook*. IEA, 2013.

[7] M. Diehl, "Airborne wind energy: Basic concepts and physical foundations," in *Airborne wind energy*, pp. 3–22, Springer, 2013.

[8] A. Cherubini, A. Papini, R. Vertechy, and M. Fontana, "Airborne wind energy systems: A review of the technologies," *Renewable and Sustainable Energy Reviews*, vol. 51, pp. 1461–1476, 2015.

[9] Twingtec, "Advantages of airborne wind energy." `http://twingtec.ch/advantages/`, 2017. Acessed August 5, 2017.

[10] Enerkite, "Enerkite EK200 technical brochure." `http://www.enerkite.de/downloads/EnerKite_200_Technical_Data_EN_SM.pdf`, 2015. Accessed August 15, 2017.

[11] M. De Lellis, A. Mendonça, R. Saraiva, A. Trofino, and Á. Lezana, "Electric power generation in wind farms with pumping kites: An economical analysis," *Renewable Energy*, vol. 86, no. C, pp. 163–172, 2016.

[12] J. Heilmann and C. Houle, *Economics of Pumping Kite Generators*, pp. 271–284. Berlin, Heidelberg: Springer Berlin Heidelberg, 2013.

[13] L. Fagiano and T. Marks, "Design of a small-scale prototype for research in airborne wind energy," *IEEE/ASME Transactions on Mechatronics*, vol. 20, no. 1, pp. 166–177, 2015.

[14] A. Millane, H. Hesse, T. A. Wood, and R. Smith, "Range-Inertial Estimation for Airborne Wind Energy," pp. 455–460, 2015.

[15] M. Ranneberg, "Sensor setups for state and wind estimation for airborne wind energy converters," *arXiv preprint arXiv:1309.1029*, 2013.

[16] L. Fagiano, K. Huynh, B. Bamieh, and M. Khammash, "On sensor fusion for airborne wind energy systems," *IEEE Transactions on Control Systems Technology*, vol. 22, no. 3, pp. 930–943, 2014.

[17] F. Messerer, *Comparative Evaluation of State Estimation Approaches for an Airborne Wind Energy System Based on Simulated and Real Flight Data*. PhD thesis, University of Freiburg, 2016.

[18] A. U. Zgraggen, L. Fagiano, and M. Morari, "Real-time optimization and adaptation of the crosswind flight of tethered wings for airborne wind energy," *IEEE Transactions on Control Systems Technology*, vol. 23, no. 2, pp. 434–448, 2015.

[19] L. Fagiano, *Control of tethered airfoils for high–altitude wind energy generation*. PhD thesis, Politecnico di Torino, 2009.

[20] T. A. Talay, *Introduction to the Aerodynamics of Flight*, vol. 367. Scientific and Technical Information Office, National Aeronautics and Space Administration, 1975.

[21] Wikipedia, "Airfoil." `https://en.wikipedia.org/wiki/Airfoil`, 2017. Acessed August 16, 2017.

[22] R. S. d. Silva *et al.*, "Aerofólios cabeados para geração de energia elétrica," 2014.

[23] C. L. Archer and M. Z. Jacobson, "Evaluation of global wind power," *Journal of Geophysical Research: Atmospheres*, vol. 110, no. D12, 2005.

[24] W. M. Organization, *Guide to meteorological instruments and methods of observation*. Secretariat of the World Meteorological Organization, 1983.

[25] J. B. Marion, *Classical dynamics of particles and systems*. Academic Press, 2013.

[26] S. Gros and M. Diehl, "Modeling of airborne wind energy systems in natural coordinates," in *Airborne wind energy*, pp. 181–203, Springer, 2013.

[27] S. J. Malham, "An introduction to lagrangian and hamiltonian mechanics," *Maxwell Institute for Mathematical Sciences & School of Mathematical and Computer Sciences Heriot-Watt University, Edinburgh EH14 4AS, UK*, 2014.

[28] S. M. Kay, *Fundamentals of statistical signal processing*. Prentice Hall PTR, 1993.

[29] S. S. Haykin *et al.*, *Kalman filtering and neural networks*. Wiley Online Library, 2001.

[30] D. Simon, "Kalman filtering with state constraints: a survey of linear and nonlinear algorithms," *IET Control Theory & Applications*, vol. 4, no. 8, pp. 1303–1318, 2010.

[31] R. Zekavat and R. M. Buehrer, *Handbook of position location: Theory, practice and advances*, vol. 27. John Wiley & Sons, 2011.

[32] I. Cisco Systems, *Wi-Fi Location-Based Services 4.1 Design Guide*. 2008.

[33] A. Bensky, *Wireless positioning technologies and applications*. Artech House, 2016.

[34] S. Gezici, I. Guvenc, and Z. Sahinoglu, "On the performance of linear least-squares estimation in wireless positioning systems," in *Communications, 2008. ICC'08. IEEE International Conference on*, pp. 4203–4208, IEEE, 2008.

[35] L. Zhang, C. Tao, and G. Yang, *Wireless positioning: fundamentals, systems and state of the art signal processing techniques*. INTECH Open Access Publisher, 2011.

[36] N. Patwari, J. N. Ash, S. Kyperountas, A. O. Hero, R. L. Moses, and N. S. Correal, "Locating the nodes: cooperative localization in wireless sensor networks," *IEEE Signal processing magazine*, vol. 22, no. 4, pp. 54–69, 2005.

[37] M. De Lellis, *Airborne wind energy with tethered wings: modeling, analysis and control*. PhD thesis, Federal University of Santa Catarina, 2016.

[38] L. Fagiano and M. Milanese, "Airborne wind energy: an overview," in *American Control Conference (ACC), 2012*, pp. 3132–3143, IEEE, 2012.

[39] M. L. Loyd, "Crosswind kite power (for large-scale wind power production)," *Journal of energy*, vol. 4, no. 3, pp. 106–111, 1980.

[40] R. Schmehl, "The international airborne wind energy conference 2015: Book of abstracts," 2015.

[41] M. Diehl, *Real-time optimization for large scale nonlinear processes*. PhD thesis, 2001.

[42] O. H. Hjukse, "State estimation and kalman filtering of tethered airfoils: by use of ground based measurements," 2011.

[43] M. De Lellis, R. Saraiva, and A. Trofino, "Turning angle control of power kites for wind energy.," in *CDC*, pp. 3493–3498, 2013.

[44] L. Fagiano, A. U. Zgraggen, M. Morari, and M. Khammash, "Automatic crosswind flight of tethered wings for airborne wind energy: Modeling, control design, and experimental results," *IEEE Transactions on Control Systems Technology*, vol. 22, no. 4, pp. 1433–1447, 2014.

[45] R. Saraiva, M. D. Lellis, E. Schmidt, and A. Trofino, "Dynamics identification, filtering and control design for power kites," 2017.

[46] P. Williams, B. Lansdorp, and W. Ockels, "Modeling and control of a kite on a variable length flexible inelastic tether," in *AIAA Modeling and Simulation Technologies Conference and Exhibit*, p. 6705, 2007.

[47] U. Fechner, R. van der Vlugt, E. Schreuder, and R. Schmehl, "Dynamic model of a pumping kite power system," *Renewable Energy*, vol. 83, pp. 705–716, 2015.

[48] B. Houska and M. Diehl, "Optimal control for power generating kites," in *Control Conference (ECC), 2007 European*, pp. 3560–3567, IEEE, 2007.

[49] P. Williams, B. Lansdorp, and W. Ockels, "Nonlinear control and estimation of a tethered kite in changing wind conditions," *Journal of guidance, control, and dynamics*, vol. 31, no. 3, pp. 793–799, 2008.

[50] J. H. Baayen and W. J. Ockels, "Tracking control with adaption of kites," *IET control theory & applications*, vol. 6, no. 2, pp. 182–191, 2012.

[51] C. Jehle and R. Schmehl, "Applied tracking control for kite power systems," *Journal of Guidance, Control, and Dynamics*, vol. 37, no. 4, pp. 1211–1222, 2014.

[52] M. Erhard and H. Strauch, "Control of towing kites for seagoing vessels," *IEEE Transactions on Control Systems Technology*, vol. 21, no. 5, pp. 1629–1640, 2013.

[53] R. Saraiva, M. De Lellis, and A. Trofino, "Passive phase design of a pumping kite wind generator," *IFAC Proceedings Volumes*, vol. 47, no. 3, pp. 6764–6769, 2014.

[54] M. Erhard and H. Strauch, "Sensors and navigation algorithms for flight control of tethered kites," *arXiv preprint arXiv:1304.2233*, 2013.

[55] A. Bormann, M. Ranneberg, P. Kövesdi, C. Gebhardt, and S. Skutnik, "Development of a three-line ground-actuated airborne wind energy converter," in *Airborne wind energy*, pp. 427–436, Springer, 2013.

[56] NASA, "Control and tracking for tethered airborne wind energy vehicles.." `https://technologygateway.nasa.gov/docs/TOA_LARC120_aWE_7web.pdf`, 2013. Acessed October 7, 2016.

[57] K. Geebelen, A. Wagner, S. Gros, J. Swevers, and M. Diehl, "Moving horizon estimation with a huber penalty function for robust pose estimation of tethered airplanes," in *American Control Conference (ACC), 2013*, pp. 6169–6174, IEEE, 2013.

[58] A. Millane, *Sensor Fusion for Airborne Wind Energy Estimation*. PhD thesis, ETH Zurich, 2015.

[59] E. Schmidt, M. D. Lellis, R. Saraiva, and A. Trofino, "State estimation of a tethered airfoil for monitoring, control, and optimization," 2017.

[60] T. A. Wood, H. Hesse, A. U. Zgraggen, and R. S. Smith, "Model-based identification and control of the velocity vector orientation for autonomous kites," in *American Control Conference (ACC), 2015*, pp. 2377–2382, IEEE, 2015.

[61] L. Fagiano, E. Nguyen-Van, F. Rager, S. Schnez, and C. Ohler, "Autonomous takeoff and flight of a tethered aircraft for airborne wind energy," *IEEE Transactions on Control Systems Technology*, 2017.

[62] R. van der Vlugt, J. Peschel, and R. Schmehl, "Design and experimental characterization of a pumping kite power system," in *Airborne wind energy*, pp. 403–425, Springer, 2013.

[63] W. T. A. Polzin M, Hesse H and S. R. S., "Visual motion tracking for estimation of kite dynamics," Presented at the Airborne Wind Energy Conference (AWEC), 2015.

[64] D. Kurth, G. Kantor, and S. Singh, "Experimental results in range-only localization with radio," in *Intelligent Robots and Systems, 2003.(IROS 2003). Proceedings. 2003 IEEE/RSJ International Conference on*, vol. 1, pp. 974–979, IEEE, 2003.

[65] J. C. Meza, "Steepest descent," *Wiley Interdisciplinary Reviews: Computational Statistics*, vol. 2, no. 6, pp. 719–722, 2010.

[66] Beagleboard, "Beaglebone black.." `https://beagleboard.org/black`, 2013. Acessed August 8, 2017.

[67] N. GmbH, "Swarm product family.." `http://nanotron.com/EN/PR_protect.php`, 2013. Acessed August 7, 2017.

[68] D. Neirynck, E. Luk, and M. McLaughlin, "An alternative double-sided two-way ranging method," in *Positioning, Navigation and Communications (WPNC), 2016 13th Workshop on*, pp. 1–4, IEEE, 2016.

[69] Arduino, "Arduino cc.." `http://www.arduino.cc`, 2017. Acessed August 8, 2017.